



Universität
Bremen

Theoretical investigation on
light-driven ultrafast dynamics in
nanoscale.

VON
ADRIAN DOMÍNGUEZ CASTRO

GUTACHTER 1: PROF. DR. THOMAS FRAUENHEIM
GUTACHTER 2: PROF. DR. ANGEL RUBIO

VOM ZUR ERLANGUNG DES AKADEMISCHEN GRADES EINES
DOKTORS DER NATURWISSENSCHAFTEN
(DR. RER. NAT.)

FACHBEREICH FÜR PHYSIK UND ELEKTROTECHNIK
UNIVERSITÄT BREMEN
BREMEN, DEUTSCHLAND
SEPTEMBER 23, 2022

©2022 – ADRIAN DOMÍNGUEZ CASTRO
ALL RIGHTS RESERVED.

Theoretical investigation on light-driven ultrafast dynamics in nanoscale.

ABSTRACT

The present doctoral thesis is a contribution to the computational modeling of light-driven ultrafast charge transfer on TiO_2 and Gold Nanoclusters. Specifically, we describe by using theoretical modeling how the computational simulations complement the experimental findings from different perspectives. With this aim in mind, we have applied simulations techniques to elucidate the mechanism involved and the prediction of photoinduced charge transfer on the systems of interest.

One of the challenges of photocatalysis is to understand the ultrafast dynamics during early stages. Inspired by the experimental work developed by our collaborators, the research focus is unraveling the ultrafast nature of charge trapping and interfacial charge transfer processes involved. In the study performed on the photooxidation of CO on TiO_2 , it is predicted and confirmed the presence of intragap unoccupied O_2 levels allowing the formation of a charge transfer complex. The reaction is initiated following laser illumination at a photon energy of 1.6 eV, by direct transfer of electrons from TiO_2 to physisorbed O_2 . These findings highlight the possibility to trigger the photoreaction on TiO_2 with visible light instead conventional electron/hole formation. In the study conducted about on $\text{H}_2\text{O}-\text{TiO}_2$ system, Ehrenfest dynamics simulations underline the interfacial hole transfer from TiO_2 to molecular adsorbed water takes place within 285 fs. With the efficient trapping of the hole at the surface by hydroxyl groups, facilitate a new Hydrogen bond formation and efficient interfacial charge transfer. In the study on the photodynamics of $(\text{TiO}_2)_{153}$ anatase nanoparticle, no electron/hole recombination is observed in the time scale studied. The photoinduced electron/hole formation and polaron effects are responsible for the narrowing of the peaks corresponding with L-edge bands in the TiO_2 nanoparticle. The impact of the lattice vibrations underline the mechanism involved.

Regarding the Gold Nanoclusters, an atomistic description of light-driven quantum dynamics in a set of different thiolated Gold Nanoclusters formed by a labeled Gold Nanocluster acting as a donor and pyrene as an acceptor is performed by using Ehrenfest dynamics. The systems under study show an ultrafast charge transfer, separation, and

stabilization. The findings highlight that the presence of chains in the functionalization of the Gold Nanocluster matters, the coherent oscillations matters as well for a more efficient irreversible charge transfer and charge separation to take place. The simulations are in accordance with experimental investigation and predict new insights in the charge transfer processes involved from the Gold Nanocluster to the labeled pyrene. For the first time the photoinduced charge separation of pyrene-functionalized middle-sized $\text{Au}_{70}\text{S}_{20}(\text{PH}_3)_{16}$ and large-sized $\text{Au}_{108}\text{S}_{24}(\text{PR}_3)_{16}$ ($\text{R} = \text{H}, \text{CH}_3, \text{C}_2\text{H}_5, \text{C}_6\text{H}_5$) clusters is reported. The proposed mechanism uncovers an ultrafast and irreversible photoinduced charge transfer from the Gold Nanocluster unit to the pyrene derivative in all cases. By a Fourier transform analysis of the dynamics, the effect of vibronic couplings is highlighted. With the increase of the Tolman cone angle is observed an increase on the photoinduced charge transfer ability, for the cases investigated. Concluding, that the steric effects are more significative than the pi-acceptor capacity of the phosphine ligands considered.

In this doctoral thesis, the three pillars of theoretical modeling such as interpretation, confirmation and prediction, have underlined the importance of simulations techniques in femtochemistry on the analysis and understanding of experimental data and the vaticination of photoinduced charge transfer. The significance and novelty of the studies presented is that due to the several challenges on the accurate description of the charge transfer processes involving the systems of interest, the benefits of the DFT and DFTB based calculations are highlighted. From the ground state description, the computation of X-ray absorption spectroscopy (XAS) and X-ray photoelectron spectroscopy (XPS) and the excited states studies applying the real-time Ehrenfest approach in the TDDFTB framework. This last method is a valuable tool for the study of large systems for new materials design with applications in photochemistry and nanophotonics. This work could be useful for the investigation on this topic in the near future.

Contents

1	INTRODUCTION	I
2	DENSITY FUNCTIONAL THEORY: AN OVERVIEW	7
2.1	DFT foundations	8
2.2	Exchange correlation functionals.	10
2.3	TD-DFT	16
3	DENSITY FUNCTIONAL TIGHT-BINDING APPROACH	21
3.1	Basics on Tight-Binding methodology	22
3.2	Brief description of the DFTB Approach	26
3.3	SCC-DFTB	29
4	EXCITED-STATE PROCESSES AND MIXED QUANTUM/CLASSICAL DYNAMICS	34
4.1	Photoinduced processes and Born-Oppenheimer breakdown	35
4.2	Ehrenfest dynamics	41
4.3	Surface Hopping	47
5	PHOTOINDUCED CHARGE TRANSFER IN FUNCTIONALIZED GOLD NANOCCLUSERS	49
5.1	Photoinduced charge transfer in pyrene-functionalized Thiolated GNC	50
5.2	Impact of vibronic coupling effects on light-driven charge transfer in pyrene-functionalized middle and large-sized Metalloid GNC	63
6	THEORY MEETS EXPERIMENTS FOR LASER-INDUCED PROCESSES ON TiO ₂	79
6.1	CO photooxidation on TiO ₂ anatase 101 surface	80
6.2	Water-TiO ₂ anatase 101 surface	88
6.3	X-Ray absorption spectroscopy of TiO ₂ anatase nanoparticle	100
7	CONCLUSIONS	107

APPENDIX A	LIST OF PUBLICATIONS	112
APPENDIX B	APPENDIX SECTION 5.1	116
B.1	Study of the effect of the Temperature in the charge-transfer processes: A configuration sampling	116
APPENDIX C	APPENDIX SECTION 5.2	122
C.1	Electronic structure - Density of states	122
APPENDIX D	APPENDIX SECTION 6.1	126
REFERENCES		142

Listing of figures

2.1	Jacob's ladder of density functional approximations. Adapted from ref. 39	15
4.1	Diagram for the electronic states of a molecule and the possible transitions between those states. In Figure Abs represent Absorption process, the non-radiative processes k_{IC} internal conversion, k_{ISC} intersystem crossing, S_0 ground state, and S_1, S_2, S_n, T_1, T_2 excited states with spin multiplicity singlet and triplet respectively.	40
4.2	Ehrenfest approach	42
4.3	Surface Hopping method	47
5.1	Schematic representation of the systems studied in the present work. On the left side, $[\text{Au}_{25}(\text{SR})_{17}\text{SPyr}]^-$, i.e., one pyrene molecule attached to the gold nanocluster $[\text{Au}_{25}(\text{SR})_{18}]^-$ (GNC) with different protecting groups R: H, hexyl and phenylethyl for IA, IB and IC, respectively. On the right side, two newly designed systems with pyrene molecules attached in two different positions.	51
5.2	Absorption spectra for: (a) IA system. (b) IB system.	52
5.3	Absorption spectra for: (a) IC system. (b) IIB system. (c) IIB-prime system.	53
5.4	Δq as a function of time for IA and IB systems under study.	55
5.5	Changes in the Mulliken charges with respect to their ground-state values as a function of time for the donor cases, IA system (a) and IB system (b). Green curve corresponds with the electron dynamics at 0K. Blue curve represents the Ehrenfest dynamics at 0K. And red curve is the average obtained from the Ehrenfest dynamics at 300K for the decorrelated sampling configurations, with the red transparency as the standard deviation obtained, respectively, for each case under study.	55
5.6	(Up) Δq as a function of time for one single frame from the NVT assemble presented in Fig. 5.5 for IA (a) and IB (b). (Bottom) Fourier intensity spectrum of the charge-transfer dynamics obtained above for the system IA (c) and IB (d).	58

5.7	(a) Δq as a function of time for the IC system.(b) Contribution analysis for the Δq as a function of time for the IC system. (c) Δq as a function of time for the IIB and IIB' systems and compared with the IB study case.	61
5.8	(a) Contribution analysis for the Δq as a function of time for the IIB system. (b) Contribution analysis for the Δq as a function of time for the IIB' system.	62
5.9	Molecular structure for: (a) $\text{Au}_{70}\text{S}_{20}(\text{PH}_3)_{15}\text{PH}_2\text{Pyr}$ and (b) $\text{Au}_{108}\text{S}_{24}(\text{PH}_3)_{15}\text{PH}_2\text{Pyr}$ systems. The orange, yellow, purple, red, blue and white represent the Au, S, P, O, N and H atoms, respectively. For simplicity and clarity the graphical representation of the rest of the systems under study are omitted.	65
5.10	Absorption spectra obtained respectively, using RT-TDDFTB approach for the systems: (a) $\text{Au}_{70}\text{S}_{20}(\text{PH}_3)_{15}\text{PH}_2\text{Pyr}$, (b) $\text{Au}_{108}\text{S}_{24}(\text{PH}_3)_{15}\text{PH}_2\text{Pyr}$. . .	66
5.11	Changes in the Mulliken charges with respect to their ground-state values as a function of time: (a) $\text{Au}_{70}\text{S}_{20}(\text{PH}_3)_{15}\text{PH}_2\text{Pyr}$ and (c) $\text{Au}_{108}\text{S}_{24}(\text{PH}_3)_{15}\text{PH}_2\text{Pyr}$, with (b) and (d) displaying the individual contributions, respectively.	68
5.12	Fourier intensity spectra of the charge transfer dynamics obtained respectively for: (a) $\text{Au}_{70}\text{S}_{20}(\text{PH}_3)_{15}\text{PH}_2\text{Pyr}$ and (b) $\text{Au}_{108}\text{S}_{24}(\text{PH}_3)_{15}\text{PH}_2\text{Pyr}$	70
5.13	Absorption spectra obtained respectively, using RT-TDDFTB approach for the systems: (a) $\text{Au}_{108}\text{S}_{24}(\text{PPh}_3)_{15}\text{PPh}_2\text{Pyr}$, (b) $\text{Au}_{108}\text{S}_{24}(\text{PCH}_3)_{15}\text{P}(\text{CH}_3)_2\text{Pyr}$, and (c) $\text{Au}_{108}\text{S}_{24}(\text{P}(\text{C}_2\text{H}_5)_3)_{15}\text{P}(\text{C}_2\text{H}_5)_2\text{Pyr}$	71
5.14	Changes in the Mulliken charges with respect to their ground-state values as a function of time: (a) $\text{Au}_{108}\text{S}_{24}(\text{PPh}_3)_{15}\text{PPh}_2\text{Pyr}$, (d) $\text{Au}_{108}\text{S}_{24}(\text{PCH}_3)_{15}\text{PCH}_2\text{Pyr}$, and (g) $\text{Au}_{108}\text{S}_{24}(\text{PC}_2\text{H}_5)_{15}\text{P}(\text{C}_2\text{H}_5)_2\text{Pyr}$	72
5.15	Individual contributions corresponding to the cases: (a) $\text{Au}_{108}\text{S}_{24}(\text{PPh}_3)_{15}\text{PPh}_2\text{Pyr}$, (b) $\text{Au}_{108}\text{S}_{24}(\text{PCH}_3)_{15}\text{PCH}_2\text{Pyr}$, and (c) $\text{Au}_{108}\text{S}_{24}(\text{PC}_2\text{H}_5)_{15}\text{P}(\text{C}_2\text{H}_5)_2\text{Pyr}$.	74
5.16	Fourier intensity spectra of the charge transfer dynamics obtained respectively for: (a) $\text{Au}_{108}\text{S}_{24}(\text{PPh}_3)_{15}\text{PPh}_2\text{Pyr}$, (b) $\text{Au}_{108}\text{S}_{24}(\text{PCH}_3)_{15}\text{PCH}_2\text{Pyr}$, and (c) $\text{Au}_{108}\text{S}_{24}(\text{PC}_2\text{H}_5)_{15}\text{P}(\text{C}_2\text{H}_5)_2\text{Pyr}$	75
5.17	Main value of the changes in the Mulliken charges with respect to their ground-state values as a function of time for the stable charge-transfer state versus Tolman cone angle.	77
6.1	Optimized geometry obtained corresponding with: A)CO adsorption over TiO_2 anatase 101 surface; B) O_2 adsorption over TiO_2 anatase 101 surface ; C)coadsorption over a Ti_{5c} binding site on TiO_2 anatase 101 surface; D) coadsorption over two adjacent Ti_{5c} binding site on TiO_2 anatase 101 surface, respectively. Bond lengths are given in angstrom (\AA).	84
6.2	DOS for the O_2 adsorbed system using (PBE) functional at the DFT level of theory. The Fermi level was shifted to zero.	85

6.3	Absorption spectrum of the O ₂ -TiO ₂ charge-transfer complex and pristine TiO ₂ . ϵ corresponds to the molar extinction coefficient as discussed in reference.	86
6.4	Absorption spectra of the O ₂ -TiO ₂ CT complex. The total absorption spectrum (a) has been projected onto three separate components shown in (b) metal-to-ligand CT transitions (red), ligand-to-metal CT transitions (black), and band-to-band excitations (blue).	87
6.5	Molecular representation of a unit cell for the optimized geometry obtained for (A) molecular adsorption (undissociated) of H ₂ O molecules on TiO ₂ anatase 101 surface (B) dissociative adsorption of H ₂ O molecules on TiO ₂ anatase 101 surface (C) a mixture of molecular and dissociative adsorption of H ₂ O molecules on TiO ₂ anatase 101 surface (D) molecular adsorption of H ₂ O molecules on the hydroxylated TiO ₂ anatase 101 surface. Bond lengths are given in angstrom (Å).	91
6.6	Density of States (DOS) and Partial Density of States (PDOS) for the systems under study. Top left represents the clean TiO ₂ anatase 101 surface. Top right represents the undissociated water adsorption system. Middle left corresponds with dissociated water adsorption system. Middle right corresponds with undissociated water adsorbed over Ti _{5c} site and partial hydroxylated surface. Bottom left corresponds with undissociated water adsorbed over full hydroxylated surface.	93
6.7	Changes in the Mulliken charges with respect to their ground-state values as a function of time for the systems under study. (a) undissociated water adsorption system. (b) dissociated water adsorption system. (c) undissociated water adsorbed over Ti _{5c} site and partial hydroxylated surface. (d) undissociated water adsorbed over full hydroxylated surface.	95
6.8	Dynamics evolution for the undissociated water adsorbed over Ti _{5c} site and a partially hydroxylated surface system. The Hydrogen bond formation: (A) time = 0 fs; (B) time = 101.6 fs; (C) time = 152.4 fs; (D) time = 177.8 fs; (E) time = 199.4 fs. The silver, red and white colors are used to represent Ti atoms, O atoms, and H atoms, respectively.	96
6.9	Configurations under study: (left) Mixed molecular and dissociative adsorption of H ₂ O molecules on TiO ₂ anatase(101) surface (right) molecular adsorption (undissociated) of H ₂ molecules on TiO ₂ anatase 101 surface. Oa, Ob, Oc atom types are referred in Table 1 as the TiO ₂ , Ti-OH, and molecular H ₂ O, respectively.	99
6.10	(a) (TiO ₂) ₁₅₃ nanoparticle system. (b) Density of States (DOS) and Partial Density of States (PDOS) analysis for the system under study.	102

6.1.1	Frontier orbitals of the $(\text{TiO}_2)_{153}$ nanoparticle: (a) HOMO (b) LUMO. Blue and orange colors correspond to the positive and negative isosurfaces. Isovalue $0.01 \text{ e}\cdot\text{au}^{-3}$	103
6.1.2	(a) Absorption spectra obtained using RT-TDDFTB approach (b) Changes in the Mulliken charges with respect to their ground-state values as a function of time.	104
6.1.3	X-Ray Absorption Spectra for the $(\text{TiO}_2)_{153}$ nanoparticle system.	105
6.1.4	Fourier intensity spectra obtained from the Ehrenfest dynamics.	106
A.1	The paper number 1 was selected as Cover of the ACS Catalysis journal. . .	114
A.2	The paper number 2 was selected as Inside Cover of the Nanoscale journal.	115
B.1	Classical MD analysis: (up) Total Energy (bottom) Temperature during the simulation time for the IA system.	118
B.2	Velocities autocorrelation function corresponding to the second half of the NVT dynamic.	118
B.3	Changes in the Mulliken charges with respect to their ground-state values as a function of time for the donor in the IA system. (a) Donor contribution (b) Acceptor contribution. The average curve calculated from all the configuration sampled is represented in red.	119
B.4	Classical MD analysis: (up) Total Energy (bottom) Temperature during the simulation time for the IB system.	120
B.5	Velocities autocorrelation function corresponding to the second half of the NVT dynamic.	120
B.6	Changes in the Mulliken charges with respect to their ground-state values as a function of time for the donor in the IB system. (a) Donor contribution (b) Acceptor contribution. The average curve calculated from all the configuration sampled is represented in red.	121
C.1	DOS and PDOS analysis respectively for: (a) (top) $\text{Au}_{70}\text{S}_{20}(\text{PH}_3)_{12}$ system; (bottom) $\text{Au}_{70}\text{S}_{20}(\text{PH}_3)_{11}\text{PH}_2\text{Pyr}$ system (b) (top) $\text{Au}_{108}\text{S}_{24}(\text{PH}_3)_{16}$ system; (bottom) $\text{Au}_{108}\text{S}_{24}(\text{PH}_3)_{15}\text{PH}_2\text{Pyr}$ system	123
C.2	DOS and PDOS analysis respectively for: (top) neutral $\text{Au}_{108}\text{S}_{24}(\text{PPh}_3)_{16}$ system; (bottom) neutral $\text{Au}_{108}\text{S}_{24}(\text{PPh}_3)_{15}\text{PPh}_2\text{Pyr}$ system.	124
C.3	DOS and PDOS analysis respectively for: (a) (top) $\text{Au}_{108}\text{S}_{24}(\text{PCH}_3)_{16}$ system; (bottom) $\text{Au}_{108}\text{S}_{24}(\text{PCH}_3)_{15}\text{P}(\text{CH}_3)_2\text{Pyr}$ system (b) (top) $\text{Au}_{108}\text{S}_{24}(\text{P}(\text{C}_2\text{H}_5)_3)_{16}$ system; (bottom) $\text{Au}_{108}\text{S}_{24}(\text{P}(\text{C}_2\text{H}_5)_3)_{15}\text{P}(\text{C}_2\text{H}_5)_2\text{Pyr}$ system.	125
D.1	DOS of the O_2 adsorption over TiO_2 anatase 101 surface using DFTB approach	127
D.2	DOS of the O_2/CO coadsorption over TiO_2 anatase 101 surface using DFTB approach	127

**DEDICATED TO MY BELOVED MIMI, *IN MEMORIAM*, AND TO YOU MAMUSHKA.
FOR YOUR ENDLESS LOVE, SUPPORT AND ENCOURAGEMENT.
I HOPE YOU ARE PROUD OF YOUR GENERAL.**

Acknowledgments

I WANT TO EXPRESS MY GRATITUDE to my supervisor Prof. Dr. Thomas Frauenheim for the opportunity offered to conduct my PhD research at the Bremen Center for Computational Materials Science (BCCMS) and for his help, guidance, knowledge, insightful discussions, and encouragement during my stay.

I would also like to thank to my scientific collaborators Dr. Adriel Domínguez García, Prof. Dr. Angel Rubio, Dr. Michael Wagstaffe, Dr. Heshmat Noei, Prof. Dr. Andreas Stierle, Dr. Carlos Raúl Medrano, Dr. Arnaud Fihey. It has been an exceptional experience working with you on the several projects. Thank you for all your enthusiasm and efforts.

I am very grateful to the entire Group and staff, Dr. Balint Aradi, Dr. Christof Köhler, Dr. Mohamed El-Amine Madjet, Dr. Lynn Gross, Dr. Verena Kristin Gupta, Dr. Fulu Zheng, Dr. Arkamita Bandyopadhyay, Yuxiang Liu, Wenbo Sun, Guozheng Fan, Pu Guo, Tammo van der Heide, Lyubov Varlamova, Dr. Elham Khorasani, Mohammad Bahmani, Meisam Farzalipour. I've been lucky to work with many wonderful people here. Thank you for always being such a tremendous help around the office and a great company at lunch.

A very special thank to Sandra Smit, Ann-Kristin Risken, Svenja Wehr, Angela Farny and Christine Frauenheim for the support and consideration. Your help has been invaluable. Thank you for everything!

A huge thank to my friend and office-mate Dr. Mauricio Chagas da Silva for the fruitful discussions about science during lunch and dinners in many restaurants around Bremen. Thank you for always sharing your professional knowledge and expertise. To the others coworkers who shared the office with me along the years, Dr. Cihan Bacaksiz, Dr. Ritabrata Sarkar, it's been a pleasure working together - thank you!

I would like to say a few words in German:
Meine Erinnerungen an Bremen werden mich immer begleiten. Alles hat ein Ende, nur die Wurst hat zwei. Danke für alles!

I highly and truly appreciate the people I worked with over the years, my first mentor and friend Prof. Yasser Novo Fernandez, and Prof. Dr. Fernando Guzman during my initial steps in scientific research. Those days at InSTEC have been a great source of inspiration to me. A big thank to Prof. Dr. Nelaine Mora-Diez for the great support and invitation to visit her Group at Thompson Rivers University, Canada. Thank you very much to the institutions, and programs that offered to me opportunities to visit and conduct research after my graduation. In Cuba, InSTEC. In Canada, the ELAP Program and Thompson Rivers University. In Italy, ICTP. In Japan, OIST. In The Netherlands, University of Groningen. And my current institution, BCCMS, University of Bremen, Germany. In all cases, the learning experience contributed directly to my development and to continue growing my love for science.

Lastly, I would also like to say some words dedicated to my family and friends in Spanish:

Mimi, Mamushka, ustedes hicieron todos los sacrificios inimaginables para que yo saliera adelante. Me remonto a todos mis recuerdos, y no podría existir un mejor hogar que el que ustedes me dieron. Un lugar donde dejaron que mi imaginación no tuviera límites, donde me educaron como una persona de bien y donde fui, soy y seré siempre feliz. Ustedes son mi orgullo, mi motivación y mi energía. Para mi tío Pedro y mi hermana Arianna Maria que siempre han estado conmigo, mis sobrinos Antony y Adam, por traerme tanta alegría. A mi papá que marcó un camino a seguir. Hagan de ustedes este logro, porque tienen todo que ver en mi vida.

A mi esposa Darielis de la Caridad, por los detalles, por el amor y tiempo compartido. Muchas de las paginas de esta tesis se han escrito contigo acompañándome.

Para mis amigos Kno, Orestes, Ariel, Danyer y Alejandro por la amistad y su ayuda de siempre.

I wish to acknowledge the people in Bremen, in Havana, in my hometown Esmeralda and around the globe for the friendship and constant support throughout the years. Thank you so much!

This thesis work has been carried out in the last 4 years at the Bremen Center for Computational Materials Science (BCCMS) at the University of Bremen and has been funded by DFG-RTG2247 grant (RTG-QM³ Program)

1

Introduction

THE THEORETICAL MODELING IN CONDENSED MATTER PHYSICS provides an alternative to the extremely difficult, costly or non-affordable experiments. The great power of theoretical modeling is based on three great pillars. Number one, the interpretation of difficult experiments, providing a deep understanding of experimental observations. Number 2, the confirmation of experimental findings due to the complexity and/or missing information is

presented. And number three, the prediction of a new behavior on the properties of a material, suggesting mechanisms and proposing new trends. All these key factors contribute to the synergy between theory and experimental facts. In this thesis, the ultrafast light-driven processes in TiO₂ and Gold Nanoclusters using simulation techniques based on the Density Functional Theory (DFT) and Density Functional Tight Binding (DFTB) approach and its time-dependent derivations are studied.

Photoinduced and electron transfer processes are of a fundamental importance in materials science, chemistry, biology and modern life, being crucial in areas and phenomena as diverse as photochemical reactions, molecular electronics, solar cells, photosynthesis, cellular respiration and vision, among others.^{1,2,3,4,5} These processes involve an electronic transition in which an electron is delocalized from a stationary state and is located in a different stationary state, which induces a change in the occupation number of both states. However, modeling these apparently simple processes is very challenging and demanding.⁶ To achieve efficient conversion, ultrafast charge separation and slow electron-hole recombination are desired.

An understanding of the processes of chemical reactions at the molecular level, where it is possible to investigate why some reactions occur or not, and even obtain methods to control the outcome of a chemical reaction, has been of interest to the scientific community for centuries. With the progressive development of better technologies, modern techniques and methods provided essential tools to scientists to see chemical reactions in detail. It was the work developed by Ahmed H. Zewail and coworkers whom, with their study of the atomic molecular in "slow motion" during a reaction, has seen what actually happens when the chemical bonds break down and new ones are formed. Zewail's technique uses laser

flashes of such minute duration that it manages to match the time scale on which the reactions take place, the femtoseconds.⁷ In the late 1980s, he did a series of experiments that led to the creation of the research area known as femtochemistry. For this contribution Ahmed H. Zewail was awarded the 1999 Nobel Prize in Chemistry.

Femtochemistry⁷ addresses the study of ultrafast quantum dynamics on the femtosecond time scale ($1\text{fs} = 10^{-15}\text{s}$) of atomic motions, which have vibrational periods between 10-100 fs, in nanoscopic dimensions. of the molecules. Femtochemistry has revolutionized the way we look at chemical reactions. Going from using ambiguous terms such as "activation", "barrier" or "Transition state" to being able to observe the changes that molecules undergo in real time.⁸ Nowadays, computational simulations on the nanoscale are widely used to complement experimental results, to test hypothesis and for inspiration on future experiments in femtochemistry. We know that matter is made of atoms, and the atoms are made of nuclei surrounded by electrons. The behavior of nuclei and electrons is governed by quantum theory. Unfortunately, although quantum mechanical equations can be written in a relatively compact form, they cannot be solved exactly due to the large number of degrees of freedom and interactions. Actually, the description of electronic structure and excited states dynamics is a great challenge, which has been taken on by many well recognized research groups using a variety of different approaches.⁸

Clarification of the mechanism and time-scale of the initial, rate-determining, steps during photoinduced charge transfer at the surface of a photocatalyst is meaningful and very significant.^{9,10} For instance, the description at electronic level of photoreactions on material surfaces is today a very active field. TiO_2 based materials are very relevant for industry and with a wide range of applications.^{11,12,13} The decomposition of pollutants has a great

interest for ecology and modern life because the environmental concerns nowadays.¹⁴ One photoreaction with relevance is the CO oxidation to CO₂ induced by solar light.¹⁵ This photoreaction is one of the main objectives of study in the present research thesis.

Another photoreaction of interest is the water splitting on TiO₂ anatase 101 surface. The H₂O-TiO₂ system for photocatalysis is crucial to a range of environmentally important applications including photoelectrochemical water splitting for clean carbon-free fuel production and to photocatalytic environmental remediation in general.¹⁶ One of the major challenges faced when developing effective systems for photocatalytic water splitting is to unravel the ultrafast dynamics during the early stages of the complex multi-electron processes. These critical first steps, particularly charge trapping and interfacial charge transfer, dictate charge separation and utilization which is a defining factor in overall quantum efficiency. Despite tremendous efforts, knowledge of these first steps remains highly speculative due to a lack of direct experimental evidence.

This research is part of a collaboration with an experimental partner at NanoLab DESY, Hamburg and the joint theoretical efforts between the MPSD, Hamburg and the BCCMS, Bremen. Inspired by the experimental work, the main focus of the investigation is the unraveling of the ultrafast nature of the mentioned photoreactions, and the elucidation of the charge transfer processes involved.

The light-induced charge transfer processes and the derived charge separation description become essential in the unraveling the mechanisms and reactions occurring in the nanoscale. Gold nanoclusters are of interest in other areas or applications, such as electronics, photovoltaic devices.^{17,18,19,20} The gold nanoclusters present good stability and promising pho-

tocatalytic performance.^{19,20} An incomplete understood phenomena is often reported, and the theoretical design of optoelectronic nanomaterials with the help of atomistic modeling is of paramount importance. The development of a theoretical approach is crucial in a depth understanding of electronic interactions and essential properties prior to the experimental device fabrication. This computational design is a challenge for fundamental research. The advantages of using DFTB based calculations, allowing a quantum description of the systems at a very low computational cost is very promising.

A second part of this doctoral thesis is related to Ehrenfest dynamics studies on the elucidation of ultrafast charge transfer process on a set of different thiolated gold nanoclusters formed by a labeled gold nanoclusters acting as a donor and pyrene as an acceptor. This work is a complement of previous experimental observations described in the literature with an unclear mechanism. The validation of the presented DFTB based scheme allows to propose new potential systems with superior electron transfer performance. More investigation on large organometallic clusters with phosphine ligands as protecting groups and pyrene ligand acting as acceptor is conducted here. For the first time, it is predicted the photoinduced charge transfer in these novel complexes. Phosphines are among the most important ligands in organometallic chemistry. The aim of this work is provide new insights on the role of the vibronic couplings of large organometallic clusters. The observation of the light-driven charge separation process and along with the associated vibronic modes is discussed, with the hypothesis that steric effects are at least as important as electronic ones.

The doctoral thesis has been divided into five main chapters (2,3,4,5,6), each containing a more extensive introduction to the corresponding topic. The Chapter 2 and 3 is related with the description of DFT and DFTB methodologies and the corresponding time-dependent

extensions, respectively. In the Chapter 4, a discussion on the fundamentals of excited-state processes and Ehrenfest dynamics is presented. In the Chapter 5 is proposed about the photoinduced charge transfer in functionalized gold nanoclusters. In the Chapter 6, the theoretical findings complementing experiments on TiO_2 will be described: the CO photooxidation and ultrafast photoinduced dynamics at the interface of water and TiO_2 anatase 101 surface. And a last part corresponding to an study about the femtosecond soft X-Ray absorption spectroscopy on TiO_2 nanoparticle.

*The electron density contains all information needed
to determine ground state properties of a system.*

Hohenberg-Kohn theorem

2

Density Functional Theory: An Overview

THE BASIC APPROACH to quantum chemistry uses the wavefunction ψ as the central variable. The reason is that one of the principles of quantum mechanics underlines that once we know ψ (or a good approximation to it) we have access to all the information that can be

theoretically calculated or estimated about a particular state of our system. However, there is a serious problem; the exact multielectronic wavefunction cannot be obtained due to its nature, it also depends on $4N$ variables, three spatial and one spin for each of the electrons which adds another difficulty.²¹

Unlike ψ , the electronic density $\rho(r)$ is an observable and can be experimentally measured by X-ray diffraction (XRD). Furthermore, it only depends on three coordinates, unlike ψ . It has been shown that electronic density offers all the necessary components to establish the Hamiltonian of the system as a function of it and this is precisely the foundation of the density functional theory (DFT). This method has the important advantage that it implicitly includes correlation effects in the calculations.²²

2.1 DFT FOUNDATIONS

The first theorem of Hohenberg and Kohn (1964) is the keystone on which the DFT has been built.²³ This theorem states that for systems with a non-degenerate ground state, the electronic density of the ground state $\rho_0(r)$ determines the external potential $V_{ext}(r)$ and the number of electrons. This theorem proves that $\rho_0(r)$ is determined by the molecular electronic Hamiltonian, and thus also by energy and other properties, and indirectly, the ground state wavefunction.^{22,23}

The electronic energy of the ground state E_0 is a "functional" of the function $\rho_0(r)$, and is represented by:

$$E_0 = E_v[\rho_0] \tag{2.1}$$

where the subscript v emphasizes the dependence of E_0 on the external potential $V_{ext}(r)$, which differs for different molecules.

The electronic Hamiltonian can be denoted as a function of the electron density as:

$$E_0 = E_v[\rho_0] = T[\rho_0] + E_{Ne}[\rho_0] + E_{ee}[\rho_0] \quad (2.2)$$

where T is the term referring to the kinetic energy of the electrons, E_{Ne} is the energy of attraction between the nuclei and the electrons and E_{ee} is the energy of repulsion between the electrons.

The second theorem of Hohenberg and Kohn,²³ establishes that the lowest energy obtainable for a system is the one that corresponds to the real electronic density of its base state. This is equivalent to the variational theorem and offers an operational way of finding the electronic density of the ground state of the system.^{22,23} The success of the DFT methods is due to the implementation of the Kohn and Sham formalism.²³ This formalism is a practical method to obtain $\rho_0(r)$ and E_0 from $\rho_0(r)$. It is based on the assumption that the electronic kinetic energy can be calculated using a set of orbitals that provide the electronic density of the system.

The Hamiltonian (\hat{H}_{KS}) is represented by the equation:

$$\hat{H}_{KS} = \sum_{i=1}^N \left[-\frac{1}{2} \nabla_i^2 + V_S(r_i) \right] \quad (2.3)$$

where the first term within the summation represents the operator of the kinetic energy of the electrons and is the external potential exerted by the nuclei. The operator describes a system of independent electrons by definition and therefore does not contain any electronic interaction terms. The connection of this artificial system and the real one is established by choosing the effective potential in such a way that the electron density is exactly equal to that of the ground state of the real system. Thus Equation 2.2 can be broken down as shown in Equation 2.4

$$E[\rho] = T_S[\rho] + J[\rho] + E_{Ne}[\rho] + E_{XC}[\rho] \quad (2.4)$$

Where $T_S[\rho]$ it could be calculated exactly for the non-interacting particle system, $J[\rho]$ is the coulombic potential of electron-electron interaction, $E_{Ne}[\rho]$ is the nuclei-electron interaction term and finally, $E_{XC}[\rho]$ is the correlation and exchange term which is unknown. There are a series of approaches for the development of this last term and once the most suitable one is established, the energy is minimized, maintaining the constraint that the Kohn and Sham orbitals are orthogonal. Thus a set of equations is obtained equivalent to the equations of HF, although with a different meaning. In summary we can say that the $E_{XC}[\rho]$ term includes everything that cannot be calculated exactly. One of the most active fields of the DFT is precisely the search for expressions so that they provide acceptable results.

2.2 EXCHANGE CORRELATION FUNCTIONALS.

The exchange-correlation energy $E_{XC}[\rho]$ is generally divided into two terms, the exchange component $E_X[\rho]$, and the correlation component $E_C[\rho]$, although only the combination of both makes physical sense. The term $E_X[\rho]$ is associated to the interactions between electrons

with parallel spins, while the term $E_C[\rho]$ essentially represents the interaction of electrons with opposite spin.²⁴

$$E_{XC}[\rho] = E_X[\rho] + E_C[\rho] \quad (2.5)$$

These two terms into which it decomposes $E_{XC}[\rho]$ also constitute electron density functionals and are known as exchange functional $E_X[\rho]$ and correlation functional $E_C[\rho]$.²⁴ These functionals can be of two types:

- local or depending only on electron density
- corrected or dependent on both electron density and gradient $\nabla\rho(r)$

2.2.1 LOCAL DENSITY APPROXIMATION (LDA)

The LDA is the simplest way to represent the correlation-exchange functional. In essence, this method implicitly assumes that $E_{XC}[\rho]$ at any point in space it is only a function of $\rho_0(r)$ and that it is given by the electronic density of a uniform gas of electrons, or what is the same, the system is in a medium in which the Electron density varies very slowly, so the exchange and correlation energy can be calculated using equations derived from a gas of uniform electron density. This model is quite remote from reality for both atoms and molecules, which are characterized by rapidly varying electron densities. The version of the LDA for open-layer systems is the so-called spin approximation of the local density, LSDA.²⁵

2.2.2 GENERALIZED GRADIENT APPROXIMATION (GGA)

At the beginning of the 80s, the first steps were taken for the development of other functionalities. The changes consisted of taking into account not only the electron density $\rho(r)$

at a particular point r , but also including its gradient $\nabla\rho(r)$. The latter made it possible to take into account the non-homogeneity of the electron density. This approximation considers a non-uniform gas of electrons for which it performs a Taylor series development of the density. Examples of the most commonly used exchange GGA functionalities are: Becke 88 (B)^{25,26,27,28,29,30,31} and Perdew-Wang (PW).³²

The best known correlation functional is the LYP, derived by Lee, Yang and Parr in 1988.³³ This functional was not built based on LDA, but taking into account a very exact equation of the correlation energy of the helium atom, it contains an empirical parameter. In general these GGA functionals represent a significant improvement compared to local methods (LDA; LSDA). However, the precision of these methods is not yet sufficient to correctly describe many chemical aspects of molecules. An example of the above is constituted by the van der Waals (vdW) interactions, where these fail.

2.2.3 PBE FUNCTIONAL.

Most GGA functionals contain some adjustable parameter so that the energies of a series of atoms are reproduced. Among the GGA functionals, the PW91 functional, developed by Perdew and Wang^{34,35} is the only purely ab initio one, as it was constructed using uniform electron gas data and exact conditions. The main problems presented by the functional PW91 are: a) the derivation is long and depends on many variables; b) the function is not trivial and c) it is overvalued; d) the parameters are not properly correlated; e) Analytical parameterization does not work properly at high density limits. In 1996, Perdew, Burke and Erzerhof³⁶ developed a new functional (PBE) based on the GGA and improving the functional PW91. In this new functional, an attempt was made to improve the description of the electronic cloud, to correct its behavior under a uniform field and to use a softer potential.

One way to represent inhomogeneities is through a density expansion in terms of its gradient or higher orders (D_{XC}):

$$E_{XC} = \frac{1}{2} \int \int \frac{\rho(\mathbf{r})\rho_{xc}(\mathbf{r}, \mathbf{r}')}{|\mathbf{r} - \mathbf{r}'|} D_{XC}[\rho(\mathbf{r}), \nabla\rho(\mathbf{r}), \nabla^2\rho(\mathbf{r}), \dots] d\mathbf{r}d\mathbf{r}' \quad (2.6)$$

With the incorporation of terms that take into account that the density of the medium is not homogeneous, it was possible to improve the results obtained by the LDA. This is what the different forms of the generalized gradient approximation (GGA) do, in which dependence on the exchange energy and correlation with the density and its gradient are introduced. This approach was devised by Perdew, Burke and Ernzerhof (parametrization-PBE), who considered that the energy of exchange and correlation is not only a functional of the density at a point, but also of its variation around a point. that point, that is, the magnitude of the density gradient.³⁶

The coefficients associated with the expansion D can be obtained from the verification of theoretical properties of the exchange and correlation potential such as long-range decay, symmetry or normalization properties. These coefficients have also been obtained by fitting experimental values such as structural parameters or thermochemical data. Within the GGA functionals, the most used in recent history has been the PBE method. A large part of the most relevant theoretical conditions of the term of exchange and correlation is satisfied by this functional. The exchange contribution in the D_{XC} expansion can be written as:

$$D_X^{PBE}(s) = 1 + \kappa - \frac{\kappa}{1 + \frac{\mu s^2}{\kappa}} \quad (2.7)$$

where $\mu = 0.2151$, $\kappa = 0.804$ and the dimensionless density gradient, $s = \frac{|\nabla\rho(r)|}{(2\kappa_s\rho)}$ where κ_s is the Thomas-Fermi shielding constant. The correlation energy can be calculated as

$$E_C^{PBE} = \frac{1}{2} \int \int \rho(\mathbf{r}) \left[\frac{\rho_C^{LDA}(\mathbf{r}, \mathbf{r}')}{|\mathbf{r} - \mathbf{r}'|} H[\rho, \xi, t] \right] d\mathbf{r} d\mathbf{r}' \quad (2.8)$$

where:

$$H[\rho, \xi, t] = \frac{e^2}{a_0} \gamma \eta^3 \ln \left[1 + \frac{\beta}{\gamma} t^2 \left(\frac{1 + At^2}{1 + At^2 + A^2 t^4} \right) \right] \quad (2.9)$$

In these expressions, $t = \frac{|\nabla\rho(\mathbf{r})|}{(2\nu k_s \rho)}$ is the dimensionless density gradient, $\beta = 0.066725$, $\gamma = 0.031091$, $\xi = \rho_\uparrow - \rho_\downarrow$ is the magnetization density, with $\eta(\xi) = \frac{[(1 + \xi)^{2/3} + (1 - \xi)^{2/3}]}{2}$ and the function A is :

$$A = \frac{\beta}{\gamma} \left[e^{-\frac{1}{2}} \int \frac{\rho_C^{LDA}(\mathbf{r}, \mathbf{r}')}{|\mathbf{r} - \mathbf{r}'|} d\mathbf{r}' \frac{1}{\gamma \eta^3 e^2 / a_0} - 1 \right]^{-1} \quad (2.10)$$

In the present thesis, the functional developed by Perdew, Burke and Ernzerhof (PBE) was used. It has been verified that the generalized gradient approximation (GGA) predicts

structural parameters in good agreement with experiments. However, this approximation usually underestimates the forbidden energy gap in semiconductors.³⁷

The greatest difficulty presented by this theory is to find adequate expressions for the

Chemical Accuracy	
+ dependence on virtual orbitals double hybrids: ω B97X-2, XYG3	
+ dependence on occupied orbitals	
hybrid-GGA: B3LYP, ω B97X-V	hybrid meta-GGA: M06-2X, M11
+ dependence on the kinetic energy density meta-GGA: TPSS, M06-L	
+ dependence on the gradient density GGA: PBE, BLYP	
dependence on the density LDA: GVN, GPW92	
Hartree World	

Figure 2.1: Jacob's ladder of density functional approximations. Adapted from ref. 39

term $E_{XC}[\rho]$, since if it were known precisely, the Kohn-Sham equations would allow the energy of the ground state of a system to be determined exactly, including all the correlation electronics that is considered as an effective average in the equations of Hatree-Fock (limit of this method). Great efforts have been made to be able to determine the best functional (function of a function). These include the local density approximation (LDA); the generalized (non-local) density approximation (GGA) that has led to the generation of the functionalities BP86, BLYP, PW91, etc. Functional mixing has also been considered; of the most successful hybrid functionals are B3LYP, B1B95, etc.³⁸ A classic representation of this continuous development of functionals and its meaning in terms of precision is shown in Figure 2.1.³⁹

2.3 TD-DFT

TD-DFT is the extension of DFT to time-dependent and excited-state problems, and is also one of the most popular methods (sometimes the only implementable method) in the electronic structure community for dealing with them. Again, the reason behind its popularity lies in its accuracy/computational cost ratio, which allows us to deal with larger and more complex systems. It can be used in combination with Ehrenfest dynamics.

In 1984 Runge and Gross published the generalization of DFT to the case of time-dependent potentials, now known as the time-dependent density functional theory (TDDFT).⁴⁰ The formalism is based on the fact that two densities $\rho(\mathbf{r}, t)$ and $\rho'(\mathbf{r}, t)$, which evolve from a common initial state and are influenced by two analytical potentials $v_{ext}(\mathbf{r}, t)$ and $v'_{ext}(\mathbf{r}, t)$ respectively, will not coincide if the potentials differ by more than an independent function of time.^{40,41,42} This one-to-one correspondence for the case of time-dependent densities and

potentials is the extension of Hohenberg and Kohn’s first theorem to the time domain. A direct consequence of this theorem is that, in principle, it is possible to find a time-dependent potential for which the fictitious system of non-interacting electrons evolving in its presence gives rise to a time-dependent density identical to that of the interacting system. The resulting equations for the non-interacting system are known as the time-dependent Kohn-Sham equations (TDKS):

$$-i\frac{\partial\psi_i}{\partial t} = \left[\frac{\hbar^2}{2m} \frac{\nabla^2}{2} + v_{ks}[\rho](\mathbf{r}, t) \right] \psi_i(\mathbf{r}, t) \quad (2.11)$$

where ψ_i are the Kohn–Sham orbitals and the density can be expressed as:

$$\rho(\mathbf{r}, t) = \sum_{i=1}^{N_{oc}} |\psi_i(\mathbf{r}, t)|^2 \quad (2.12)$$

where N_{oc} is the total number of occupied orbitals. As in the static version of DFT, the Kohn-Sham potential (v_{ks}) can be divided into an external contribution, a Hartree potential, and an exchange and correlation term.

$$v_{ks}(\mathbf{r}, t) = v_{ext}(\mathbf{r}, t) + v_{Hartree}(\mathbf{r}, t) + v_{xc}(\mathbf{r}, t) \quad (2.13)$$

However, in contrast to the ground state treatment, in the time-dependent formalism the exchange and correlation potential is functional of the initial wavefunctions of the interacting and reference system, as well as of all past densities $\rho(t < t)$.^{41,42} These conditions make TDDFT an inapplicable formalism for the vast majority of systems unless some approximations are introduced. First, if the initial state is nondegenerate, the dependence on

the initial wavefunction can be avoided by considering that, as a consequence of Hohenberg and Kohn's first theorem, this wavefunction is density functional of the ground state and, consequently, so is the time-dependent potential.^{41,42}

On the other hand, as mentioned before, the potential for exchange and correlation has memory of the past of density. However, if the potential changes slowly enough, its dependence on the past can be ignored in a local approximation in the time domain. In this context, the potential ends up depending only on the density present.^{41,42}

$$v_{xc}[\rho](\mathbf{r}, t) \approx v_{xc}[\rho(t)](\mathbf{r}) \quad (2.14)$$

This assumption is known as the adiabatic approximation and constitutes the analog in the time domain to the LDA approximation of the ground state. Fortunately, this approach works surprisingly well even outside the formally justifiable range.⁴² Once the previous approximations have been made (which are used for almost all currently available implementations of TDDFT, the time-dependent density evolution can be described through Equations 2.6, but substituting the unknown $v_{xc}[\rho](\mathbf{r}, t)$ for the exchange potential and correlation of the ground state associated with the instantaneous density at time t ($\rho(\mathbf{r}, t)$). Of course, as discussed before, this potential is also unknown but much more is currently known about the static trade-off and correlation effects approach than about their treatment in the field. temporal domain and the inclusion of memory effects.⁴¹

2.3.1 CASIDA EQUATION

A more extensive discussion in this topic can be found in reference 43.

It is possible to calculate the excitation energies using the time-dependent Kohn-Sham equations, in other words, it is possible to calculate the response of a system to the time-dependent external perturbation, which starts at a time t_0 . If the time-dependent perturbation is small, it is not necessary to solve the KS equations completely since perturbation theory is sufficient to determine the behavior of the system. In perturbation theory, TDDFT can be reformulated as an algebraic equation that describes the response in the frequency domain. Furthermore, instead of directly solving for the response to an external field of particular frequency, the resonant frequencies corresponding to the excitation energies of the system (and to the poles of the response functions) can be calculated.

This is achieved by the Casida equation⁴³, whose most general form is:

$$\begin{pmatrix} A & B \\ -B^* & -A^* \end{pmatrix} \begin{pmatrix} X_N \\ Y_N \end{pmatrix} = \omega_N \begin{pmatrix} X_N \\ Y_N \end{pmatrix} \quad (2.15)$$

where: A and B terms are the Hessians (also called coupling matrices), ω_N is the N-th excitation energy and vectors X_N, Y_N contain the corresponding transition amplitudes.

For real orbitals and frequency-independent DFT kernel (part of the Hessian), the equation can alternatively be simplified by defining:

$$CZ_N = \omega_N^2 Z_N \quad (2.16)$$

where:

$$C = (A - B)^{1/2}(A + B)(A - B)^{1/2}$$

$$Z_N = (A - B)^{1/2}(X_N - Y_N)$$

The Casida equation⁴³ has the form of an eigenvalue equation, with the excitation energies being the eigenvalues. Nowadays, this equation is part of many DFT codes and one way of calculating the excitation energies and excited state properties of a wide range of systems.

*I think I can safely say that nobody understands
quantum mechanics*

Richard P. Feynman

3

Density Functional Tight-Binding Approach

DENSITY FUNCTIONAL BASED TIGHT BINDING (DFTB) methods⁴⁴ are parameterised approximations to density functional theory. When properly fitted, DFTB can deliver results of comparable quality to first principles calculations (for example a chemically accurate pa-

parameterization) but at 100–1000 times lower computational costs.⁴⁵ The DFTB+ code⁴⁶ is an open source implementation of a range of ground and excited state, electron and phonon transport and post-DFT methods adapted to several forms of DFTB, with low order and linear scaling methods available for many problems. The code also integrates with a number of frameworks and external tools for tasks including high throughput calculations, specific property calculations, advanced thermodynamic calculations and machine learning. It will run on platforms between a laptop and GPU accelerated supercomputers and is designed to allow long term reproducibility of results.

3.1 BASICS ON TIGHT-BINDING METHODOLOGY

This method is an intermediate alternative between the resolution of the Schrödinger equation within the framework of the Born-Oppenheimer approximation and the direct resolution of said equation using the laws of Quantum Mechanics, which constitutes the basis of the "ab-initio" methods, or first principles. It involves the resolution of equations in which the electronic structure of the system is taken into account but, unlike first principles methods, it uses some kind of approximation. In this way, some of the important aspects that are lost in the description through empirical potentials are characterized, such as the quantum nature of the bond, correctly describing not only the interaction between the pairs of atoms, but also the angular character of the bond. same. In the same way, it also accounts for the electronic filling in the bonding and anti-bonding states of a system, controlling the bond forces and also the energy changes that would occur in it due to possible variations in the configuration of the system. Unlike the "ab-initio" methods, the Tight-Binding methodology makes use of a series of parameters that will be different depending on the nature of the system to be studied, which translates into a loss of transferability. However, it gains in

calculation speed, in addition to offering the possibility of describing systems with a greater number of atoms.

The electronic states of a system are characterized by a wave function generated by a linear combination of others that constitute a basis of the space of atomic wave functions, that is, those that are characteristic of an atom. In them, while the angular dependency resembles an atomic orbital, the radial dependency can be quite different. Usually, the number of wavefunctions that constitute the base is usually limited to only those that have a relevant importance in the formation of the bonds, that is, those that are the outermost of the atom. Thus, if $\psi^{(n)}$ is considered the wave function of the n-th eigenstate of the system to be described and $\varphi_{i\alpha}$ the i-th function of the chosen base, we have,

$$\psi^{(n)} = \sum_{i\alpha} c_{i\alpha}^{(n)} \varphi_{i\alpha} \quad (3.1)$$

where the subscript i denotes the position of the atom in question and α the symmetry of the corresponding atomic orbital, which takes on different values depending on its angular nature (s, p, d, ...). The coefficients of the expansion $c_{i\alpha}^{(n)}$ are calculated by substituting the wavefunction $\psi_{i\alpha}$ into the Schrödinger equation,

$$\hat{H}\psi^{(n)} = E^{(n)}\psi^{(n)} \quad (3.2)$$

where \hat{H} is the Hamiltonian of the system and $E^{(n)}$ is the energy of the nth eigenstate.

The idea of the Tight-Binding methodology is to replace the exact Hamiltonian with a parameterized one, that is, one in which the elements of the matrix of the Hamiltonian in the base used can be written based on a series of parameters that must be adjusted. previously. The eigenstates of the Hamiltonian will be obtained by solving the characteristic equation of the system. There are numerous contributions to the study of the Tight-Binding formalism. It is necessary to emphasize that what really differentiates this diversity of methodologies from each other is the way in which the energy problem is treated. In the work of Goringe et al.⁴⁷, different Tight-Binding methods that appear in the literature are excellently summarized.

The origins of the Tight-Binding methodology were centered on the study carried out by Slater and Koster on the electronic structure of large systems. In particular, for periodic systems and using the model proposed by Bloch (Bloch sum), Slater and Koster deduced that the matrix elements of the Hamiltonian, expressed in a basis formed by orthogonal wavefunctions, are written,

$$H_{i\alpha i\beta} = \sum_{R_j} e^{[ik(R_j - R_i)]} \int \psi_{i\alpha}^*(r - R_i) \hat{H} \psi_{i\beta}(r - R_j) dr \quad (3.3)$$

The fundamental strategy, in some way, defines the Tight-Binding methodology, is to replace the integral in this equation by a certain parameter that depends only on the internuclear distance $|R_i - R_j|$ and on the shape of the wave functions used. The first approximation adopted is known as a two centers approximation, in which the potential term of the Hamiltonian is replaced by a potential function that only depends on the atoms i and j , in which

the orbitals will be located. The next approach would be to include an extra term in the potential part of the Hamiltonian, which infers a certain non-local character, suggested by the influence of the rest of the atoms in the system. This is known as the three center approach. In conclusion, it could be stated that the Tight-Binding model is more efficient the better the parameterization chosen for the matrix elements of the Hamiltonian.

Although the Tight-Binding methodology was initially designed for the study of the band structure of periodic systems, it was quickly reaffirmed as a new atomistic method. In this sense, having knowledge of the configuration energy of an atomic system would be essential when defining its properties, both static and dynamic. From an atomistic point of view, the value of this energy can be written as a contribution of two terms,

$$E_{total} = E_{band} + E_{rep} \quad (3.4)$$

the first term for the energy of the band structure and the second term for a repulsive term in the form of a potential of pairs and that, therefore, will depend on the distance between each pair of atoms. The fact of adding the repulsive term to the band energy is interpreted as an effect provided by the difference between the ion-ion and electron-electron electrostatic interaction energies. Later it was shown, by means of Quantum Mechanics arguments based on the formulation of the Density Functional, that this approximation in the expression of energy is quite adequate.

3.2 BRIEF DESCRIPTION OF THE DFTB APPROACH

The Tight-Binding method based on Density Functional (DFTB)⁴⁶ is based on the second order expansion of the total Kohn-Sham energy obtained with DFT with respect to load fluctuations. The zero-order approximation is equivalent to a non-self-consistent standard computation TB, while for the second order a list parameter-free expression can be computed to easily determine the generalized values of the Hamiltonian matrix elements. These are modified by a self-consistent Mulliken charge redistribution (SCC). In addition to the usual band structure and short-range repulsive force terms, the final Kohn-Sham energy also includes the coulombian interaction between charge fluctuations. At large distances this explains the long-range electrostatic forces between two point charges and approximately includes self-interaction contributions from a given atom if the charges are on the same atom. Due to the complement of SCC, DFTB can be successfully applied to problems where deficiencies of TB without SCC are evident.^{46,48}

As mentioned previously, the most important limitation of tight-binding calculations arises from the transferability problems that occur when describing systems of a different nature. Due to this, it is necessary to make as many adjustments to the parameters involved in the Hamiltonian matrix elements as there are different systems to be modeled. Porezag et al⁴⁸ propose a method by which by means of DFT the elements of the Hamiltonian matrix can be calculated directly, thus avoiding the need to handle complicated adjustment methods. The procedure followed by these authors is described in the three fundamental steps described below: (This is the procedure implemented in DFTB+ code)

Step 1: Creating the pseudoatoms

In the first place, we start from a base formed by pseudoatomic wave functions written in terms of Slater-type orbitals and spherical harmonics,

$$\varphi_\nu(\mathbf{r}) = \sum_{n,\alpha,l,m}^{\nu} a_{n,m} r^{l+n} e^{-ar} Y_{lm} \left(\frac{\mathbf{r}}{r} \right) \quad (3.5)$$

This basis is used to solve self-consistently a modified Kohn-Sham equation,

$$\left[\hat{T} + V_{psat}(\mathbf{r}) \right] \varphi_\nu(\mathbf{r}) = \varepsilon_\nu^{psat} \varphi_\nu(\mathbf{r}) \quad (3.6)$$

where the potential $V_{psat}(\mathbf{r})$ is defined by:

$$V_{psat}(\mathbf{r}) = V_{nuc}(\mathbf{r}) + V_H(\mathbf{r}) + V_{XC}(\mathbf{r}) + \left(\frac{\mathbf{r}}{r_0} \right)^N \quad (3.7)$$

where the potentials V_{nuc} , V_N and V_{XC} are, respectively, the potentials, nuclear, Hartree and exchange and correlation. The last addend has the mission of forcing the wave function not to be located in areas far from the nuclei. A consequence of this is that the electron density will have a more compressed appearance than in the case of the free atom. A good choice of parameters contained in this last term is $N = 2$ and $r_0 = 2r_{cov}$ where r_{cov} is the covalent radius of the concrete element.

Step 2: Calculation of the elements of the matrix

Using the solutions $\varphi_\nu(\mathbf{r})$ of the modified Kohn-Sham type equation (3.6), we proceed with the Tight-Binding parameterization mechanism. An effective potential written as the sum of spherical potentials of atomic type is constructed for each structure,

$$V_{eff}(\mathbf{r}) = \sum_k V_0^{(k)}(|\mathbf{r} - \mathbf{R}_k|) \quad (3.8)$$

where \mathbf{R}_k is the position of atom k and $V_0^{(k)}$ is the Kohn-Sham potential for a neutral pseudoatom originating from the electronic charge density in compressed form, that is, the expression of the pseudoatomic potential without the last addend. Using this potential, the matrix elements of the Hamiltonian are calculated,

$$H_{i\alpha j\beta} = \begin{cases} \varepsilon_{i\alpha} & \text{if } \beta = \alpha \text{ and } j = i \\ \langle \varphi_{i\alpha} | T + V_0^{(j)} | \varphi_{j\beta} \rangle & \text{if } j \neq i \\ 0 & \text{rest} \end{cases} \quad (3.9)$$

The indexes i and j indicate the atom on which the potentials and wave functions are centered. The α and β indexes refer to the type of symmetry of the orbital. The diagonal terms of the matrix correspond to the eigenvalues of the Hamiltonian of the free atom, thus ensuring the verification of the limiting case, which is the isolated atom. It is observed that the approximation is to two centers, so the elements of the matrix only depend on the distances between each pair of atoms.

Step 3: Calculation of the repulsive part

Once the Hamiltonian is characterized, the calculation of the band structure energy is immediate, for example, by diagonalizing the matrix. The repulsive part is determined as the difference between the total energy, calculated in a self-consistent way (E_{total}^{AC}) and the band structure energy (E_{band}) in function of the interatomic distances,

$$E_{rep}(R) = E_{total}^{AC}(R) + E_{band}(R) \quad (3.10)$$

Then, it is convenient to give the repulsive potential a certain functional form, so that it can be treated analytically when determining its contribution, e.g, to forces or elastic properties. The tendency is to write this term as a sum of polynomials or in exponential form, involving a certain cutting radius, so that a smooth behavior can be guaranteed throughout its path.

3.3 SCC-DFTB

DFTB can be derived from DFT. In great details has been discussed before.^{44,49} The following discussion is focus only in mainful details based on ref. 49.

The DFT electronic energy of the system is obtained from solving the Kohn–Sham equation. Then, the total energy of the system is the sum of the electronic energy and the interaction energy of the nuclei. For a system with M nuclei and N electrons, it is expressed as follow:

$$\begin{aligned}
E[\rho] = \sum_i^M \langle \psi_i | & -\frac{1}{2} \nabla_i^2 + V_{ext}(\vec{r}) + \frac{1}{2} \int \frac{\rho(\vec{r})}{|\vec{r} - \vec{r}'|} d\vec{r}' | \psi_i \rangle + E_{XC}[\rho] \\
& + \frac{1}{2} \sum_{\beta}^N \sum_{\alpha \neq \beta}^N \frac{Z_{\alpha} Z_{\beta}}{|\vec{R}_{\alpha} - \vec{R}_{\beta}|} \quad (3.11)
\end{aligned}$$

In the SCC-DFTB approximation, the electronic density in DFT theory is substituted by a reference density plus fluctuations,

$$\rho(\vec{r}) = \rho_0(\vec{r}) + \delta\rho(\vec{r}) \quad (3.12)$$

equation (3.12) inserted in (3.11)

$$\begin{aligned}
E[\rho_0 + \delta\rho] = \sum_i^{occ} \langle \psi_i | & -\frac{1}{2} \nabla_i^2 + V_{ext}(\vec{r}) + \int \frac{\rho'_0}{|\vec{r} - \vec{r}'|} d\vec{r}' + V_{XC}[\rho_0] | \psi_i \rangle \\
& - \frac{1}{2} \int \int \frac{\rho'_0(\rho_0 + \delta\rho)}{|\vec{r} - \vec{r}'|} d\vec{r} d\vec{r}' - \int V_{XC}[\rho_0](\rho_0 + \delta\rho) d\vec{r} \\
& + \frac{1}{2} \int \int \frac{\delta\rho'_0(\rho_0 + \delta\rho)}{|\vec{r} - \vec{r}'|} d\vec{r} d\vec{r}' + E_{XC}[\rho_0 + \delta\rho] + E_{nn} \quad (3.13)
\end{aligned}$$

With $\rho'_0 = \rho_0(\vec{r})$ and $\delta\rho' = \delta\rho(\vec{r}')$. The second term corrects the double counting of the Coulomb term, the 3rd term corrects the new exchange-correlation contribution and the 4th term arises from the separation of the Coulomb energy into a part relative to ρ_0 and another

relative to $\delta\rho$.

The term $E_{XC}[\rho_0 + \delta\rho]$ expanded in a Taylor serie, (truncate after the second term)

$$E_{XC}[\rho_0 + \delta\rho] = E_{XC}[\rho_0] + \int \frac{\delta E_{XC}}{\delta\rho} \Big|_{\rho_0} \delta\rho d\vec{r} + \frac{1}{2} \int \int \frac{\delta^2 E_{XC}}{\delta\rho\delta\rho'} \Big|_{\rho_0} \delta\rho\delta\rho' d\vec{r}d\vec{r}' \quad (3.14)$$

equation (3.14) inserted in (3.13) and

$$\left(\frac{\delta E_{XC}}{\delta\rho} \right) \Big|_{\rho_0} = V_{XC}[\rho_0]$$

$$\begin{aligned} E = & \sum_i^{occ} \langle \psi_i | -\frac{1}{2} \nabla_i^2 + V_{ext}(\vec{r}) + \int \frac{\rho'_0}{|\vec{r} - \vec{r}'|} d\vec{r}' + V_{XC}[\rho_0] | \psi_i \rangle \\ & - \frac{1}{2} \int \int \frac{\rho'_0 \rho_0}{|\vec{r} - \vec{r}'|} d\vec{r}d\vec{r}' + E_{XC}[\rho_0] - \int V_{XC}[\rho_0] \rho_0 d\vec{r} + E_{nn} \\ & + \frac{1}{2} \int \int \left(\frac{1}{|\vec{r} - \vec{r}'|} + \frac{\delta^2 E_{XC}}{\delta\rho\delta\rho'} \Big|_{\rho_0} \right) \delta\rho\delta\rho' d\vec{r}d\vec{r}' \quad (3.15) \end{aligned}$$

The first term is analogue to the E_{bands} , the second line corresponds to the repulsive part. The last term includes the corrections to the fluctuations of the electronic density. The reference Hamiltonian is defined, dependent of ρ_0 .

$$E = \sum_i^{occ} \langle \psi_i | H^0 | \psi_i \rangle + E_{rep} + E_{2nd}[\delta\rho, \rho_0] \quad (3.16)$$

The described DFTB scheme is suitable when the electron density of a polyatomic structure can be well represented by a sum of atomic densities. However, the uncertainties of the standard DFTB method increase when the chemical bonds in the system are controlled by a more delicate charge balance between atoms, especially in the case of heteronuclear molecules and polar chemical complexes. To improve the calculation and transferability in the case of systems where long-range Coulomb interactions are present, the DFTB method was improved, giving rise to the tight-binding scheme based on the density functional with self-consistent charge correction (SCC-DFTB).⁵⁰

In this scheme, the electron density is corrected by including second-order contributions, which are neglected in the standard DFTB scheme. To include the electronic density fluctuations in a simple and efficient way, according to a TB approach, $\delta\rho$ is written as a superposition of atomic contributions $\delta\rho_\alpha$, with rapid decay along the distance from the corresponding atomic center

$$\delta\rho = \sum_\alpha^N \delta\rho_\alpha \quad (3.17)$$

where the atomic contributions can be simplified by a monopole approximation,

$$\delta\rho \approx \Delta q_\alpha F_{00}^\alpha Y_{00} \quad (3.18)$$

Here, Δq_α is the difference between the Mulliken atomic charge⁵¹ q_α and the charge q_α^0 of the neutral atom ($\Delta q_\alpha = q_\alpha - q_\alpha^0$); F_{00} denotes the normalized radial dependence of the electron density fluctuation in the α atom, which is approximated for spherical symmetry by the angular function Y_{00} . That is, charge transfer effects are treated, but changes in the shape of the electron density with respect to the reference density are ignored.

The SCC-DFTB total energy can be defined as following:

$$E^{SCC} = \sum_i^{occ} \langle \psi_i | H^0 | \psi_i \rangle + \frac{1}{2} \sum_{\alpha, \beta}^N \gamma_{\alpha\beta} \Delta q_\alpha \Delta q_\beta + E_{rep} \quad (3.19)$$

The DFTB+ code has utilities similar to ab-initio quantum simulation packages but is one to two orders of magnitude faster. With it you can, among other things, optimize the structure of molecules and solids and obtain densities of electronic states and band structures.

*Science can't solve the ultimate mystery of the nature.
And that is because, in the last analysis, we ourselves
are a part of the mystery that we are trying to solve.*

Max Planck

4

Excited-state processes and Mixed Quantum/Classical Dynamics

THIS CHAPTER DISCUSSES THE MIXED QUANTUM– CLASSICAL APPROACHES, WITH AN INTEREST ON THE EHRENFEST DYNAMICS AND ITS RT-TDFTB BASED SCHEME EMPLOYED IN THIS THESIS. ALSO, THE SURFACE HOPPING TECHNIQUES ARE BRIEFLY DESCRIBED.

The Born-Oppenheimer approximation is valid in the completely adiabatic case. In this situation, the nuclear dynamics is given by the potential corresponding to a pure electronic state (meaning only one eigenfunction of the electronic Hamiltonian). However, in the case which superposition of electronic states are presente, this approximation needs adjustments to keep simulating with success non-adiabatic dynamics. Several approaches exist in literature to address this problem. In the following sections 4.2 and 4.3 are discussed two of the fundamental methods.

The propagation of the classical equations of nuclear motion in an average potential, in which the energy of each electronic state contributes in an equal proportion to its electronic population is called the Ehrenfest method.^{52,53,54} On the other hand, we have the propagation of the classical trajectories in a single Born-Oppenheimer potential energy surface together with an algorithm that calculates the transition probability of the system between coupled surfaces. If a system jump occurs, the nuclear equations of motion propagate on the new surface. These last methods are the so-called methods of trajectory surface hopping (TSH).⁵⁵

4.1 PHOTOINDUCED PROCESSES AND BORN-OPPENHEIMER BREAKDOWN

Photoinduced processes are present in nature. For example, photosynthesis, photochemical smog (formation of ozone from oxygen in the stratosphere) and the process of vision (through a receptor protein sensitive to light, a biological pigment called rhodopsin that is found in the rods of the retina after absorbing light) and many others. In principle, the fun-

damental electronic state of any compound can give rise to innumerable excited electronic states, each one with a different electronic distribution that will confer different properties, with which each one will be able to give rise to a chemistry as rich as that of the fundamental state. In practice, only the excited states of lower energies are usually reactive, but this is sufficient for the reactivity to diversify greatly. Because of this, photochemical reactions have produced a considerable impact on different disciplines such as biology, medicine, chemical synthesis, electronics, engineering, etc. Despite its importance, the understanding of photochemistry is incomplete in particular on the electronic level. In this context, the theoretical description of the microscopic quantum scale and the simulation of the properties for system of interest are notorious fields in science and technology. Nowadays, many research groups around the globe have been working on these topics very active using a variety of different approaches.

The study of chemical systems is based on the separation of nuclear and electronic motion. In this regard, the Born-Oppenheimer approximation⁵⁶ is the most commonly used. This approximation is fulfilled very frequently since the speed of the electrons is much greater than the speed of the nuclei, due to the relationship between the masses of both, for instance for the hydrogen atom case is approximately 1/1836. The Born-Oppenheimer approximation⁵⁶ is related with the construction of the PES, from which it is possible to obtain a huge amount of information about the chemical behaviour. With the idea of each arrangement of atoms in space ponds to a particular energy. Changes in the structure go hand in hand with energy changes. The complete PES is accessible only for very small systems. The PES are generated by the solution of the electronic part of the Schrödinger equation. This solution gives an energy for every fixed position of the nuclei. When the energy is plotted as a function of geometries it generates the PES as a $(3N - 6)$ dimensional surface in general. And, at

the same time every electronic state has its own PES. Quantum chemical investigations are generally strictly limited to explore chemically relevant parts of the PES.

Conventional Born-Oppenheimer molecular dynamics only allows one to simulate nuclear motion on a single potential energy surface and therefore does not describe non-adiabatic processes involving non-radiative electronic transitions. This approximation breaks down when the dynamics of molecules in excited electronic states are considered.⁵⁷ Let us discuss briefly about the Born-Oppenheimer approximation breakdown:

For a system of N nuclei described by coordinates Q and N_e electrons described by coordinates x . The full Hamiltonian for the molecular system is:

$$\hat{H} = T_e + T_N + U(x, Q)$$

And the electronic Hamiltonian $\hat{H}_e = T_e + U(x, Q)$. The electronic wavefunctions $\phi_n(x, Q)$ and energies V_N are defined by $\hat{H}_e \phi_n(x, Q) = V_N \phi_n(x, Q)$

Solving the Schrödinger equation of the total Hamiltonian, $\hat{H}\psi(x, Q) = E\psi(x, Q)$, the exact wavefunction can be written as:

$$\psi(x, Q) = \sum_m \chi_m(Q) \phi(x, Q)$$

in which the exact eigenstates of the molecular system can be expanded in the eigenfunction of the electronic Hamiltonian. And, where $\chi_m(Q)$ represents the m th eigenstate for the

nuclei and $\varphi(x, Q)$ represents the m th eigenstate for the electron.

Inserting the full molecular Hamiltonian and the exact eigenstate of the system into the time-independent Schrödinger equation, can be obtained the non-adiabatic couplings:

$$[T_N + V_N(Q) - E]\chi_m(Q) = \sum_m \hat{\Lambda}_{nm}\chi_m(Q)$$

where : $\hat{\Lambda}_{nm}$ is the non adiabatic operator, describing the dynamical interaction between the electronic and nuclear motions.

With the Born-Oppenheimer approximation (called adiabatic approximation): $\hat{\Lambda}_{nm}$ is zero and,

$$[T_N + V_N(Q) - E]\chi_m(Q) = 0$$

On the other hand, with the application of the Hellman-Feynman theorem is possible to prove when/where the Born-Oppenheimer approximation breakdown. In the expression for the non-adiabatic operator:

$$\hat{\Lambda}_{nm} = \hbar^2 \sum_i \frac{1}{M_i} F_{mn}^i(x, Q) \cdot \nabla(Q_i) - \langle \varphi_n(x, Q) | \hat{T}_N | \varphi_m(x, Q) \rangle$$

where:

$$F_{mn}^i(x, Q) = \frac{\langle \varphi_n(x, Q) | \nabla(Q_i) \hat{H}_e | \varphi_m(x, Q) \rangle}{V_m(x, Q) - V_n(x, Q)}$$

Then, in the vicinity of a degeneracy, the derivative couplings $F_{mn}^i(x, Q)$ can be diverge and the Born-Oppenheimer approximation breakdown.

4.1.1 CHEMISTRY BEYOND THE BORN-OPPENHEIMER APPROXIMATION.

Going beyond this approximation implies that the motion of the electrons and nuclei is coupled, given rise to what is known as vibronic states, manifesting with new chemical and physical properties. The Born-Oppenheimer approximation⁵⁶ says that in a molecule the nuclei are essentially stationary compared to the electrons. This approximation, also referred to as the adiabatic approximation, significantly alleviates such difficulties by allowing separation of nuclear and electronic motions in molecular systems. This converts the impractical task of the solution of the molecular Schrödinger equation into two more practical steps: generation of potential energy surface (PES) by solving electronic Schrödinger equation at various geometries, and nuclear dynamics on the PES. The Born-Oppenheimer approximation is extremely powerful and often also accurate enough for most chemical processes. As a result, it is almost ubiquitously applied throughout chemistry.

Despite its utility in quantum mechanical calculations, this indispensable approximation is not always valid.⁵⁷ When a reaction takes place at high energy, usually through photoexcitation, or when electronic degeneracy is present at low energy, multiple coupled electronic states can become involved, making the process nonadiabatic. The BO approximation is also violated in photochemical processes, where absorption of a photon causes the system to be

electronically excited into the manifold of coupled electronic states, including vital biochemical processes such as vision, photosynthesis, and others processes in modern life as well, such as the photovoltaic effect, and solar energy conversion, etc.

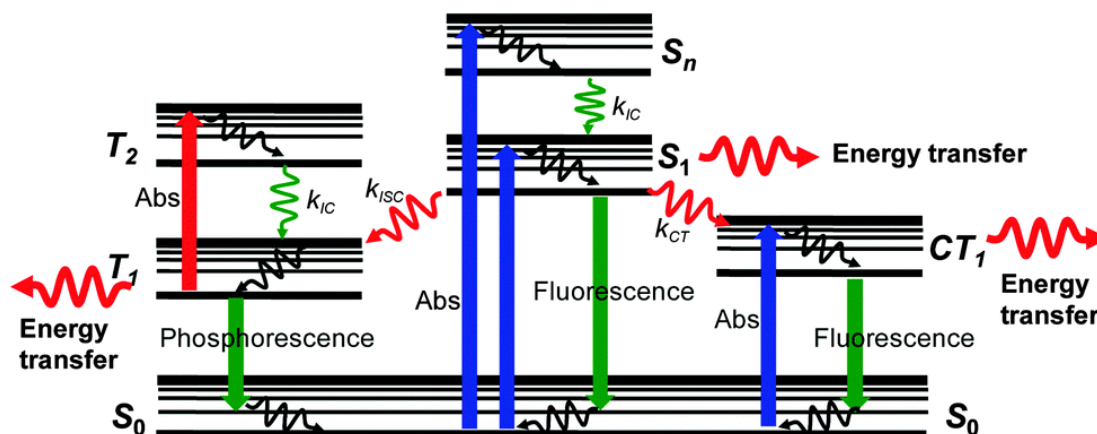


Figure 4.1: Diagram for the electronic states of a molecule and the possible transitions between those states. In Figure Abs represent Absorption process, the non-radiative processes k_{IC} internal conversion, k_{ISC} inter-system crossing, S_0 ground state, and S_1 , S_2 , S_n , T_1 , T_2 excited states with spin multiplicity singlet and triplet respectively.

The Jablonski diagram⁵⁸ presented in Figure 4.1 displays the excited states of a system and the processes involved on electronic transitions. Electronically nonadiabatic processes (also called non-BO processes) are defined as those in which the electronic state changes non-radiatively during the dynamical event. Electronically nonadiabatic processes are important and essential parts of visible and ultraviolet photochemistry, collisions of electronically excited species, chemiluminescent reactions, etc. In details, the excited states are very important for the understanding of optical experiments, various biological processes and design of new devices based on photo-induced charge transfer.

Theoretical applications addressing photo-induced processes have also become essential

alternatives, especially when experimental approaches are particularly difficult, expensive, or even nonviable. In this regard, a wide variety of methods have been proposed for performing nonadiabatic dynamics and it is possible to cite considerable literature about this topic.^{59,60,61,62,63,64,65} However, the theoretical description remains as a challenge today, and the full-dimensional quantum dynamical treatment of large systems is still a demanding task due to the exponential growth of computational resources needed for wavepacket propagation with increasing number of degree of freedom (DOFs). Additional complications arise due to the need to precompute the PESs, coupling matrix elements between electronic states, and atomistic description of the environment. In this context, the nonadiabatic Ehrenfest dynamics had been used with success capturing the essential features and reproducing with accuracy light-driven chemical reactions on materials surfaces.^{16,64,65}

4.2 EHRENFEST DYNAMICS

The seminal paper⁶⁶ of Paul Ehrenfest published on 1927 has shown that quantum mechanics does not contradict classical mechanics, but rather generalizes it – the latter can be regarded as a very good approximation to the former for a large class of physical phenomena. Second, he pioneered derivations of various kinds of classical equations of motion from underlying quantum mechanical models. Ehrenfest’s theorem simply states that expectation values of quantum mechanical operators obey the laws of classical mechanics. Derivations of the Ehrenfest’s theorem allow us to write the exact Ehrenfest equations for the nuclei as follow:

First Ehrenfest equation:

$$\frac{d\langle\vec{r}\rangle\psi}{dt} = \frac{\langle\vec{p}\rangle\psi}{m} \quad (4.1)$$

Second Ehrenfest equation:

$$\frac{d\langle\vec{p}\rangle\psi}{dt} = \langle-\nabla V\rangle\psi \quad (4.2)$$

An equation that, in terms of a force $\vec{F} = -\nabla V$, takes the expression:

$$\langle\vec{F}\rangle\psi = \langle-\nabla V\rangle\psi = \frac{d\langle\vec{p}\rangle\psi}{dt} \quad (4.3)$$

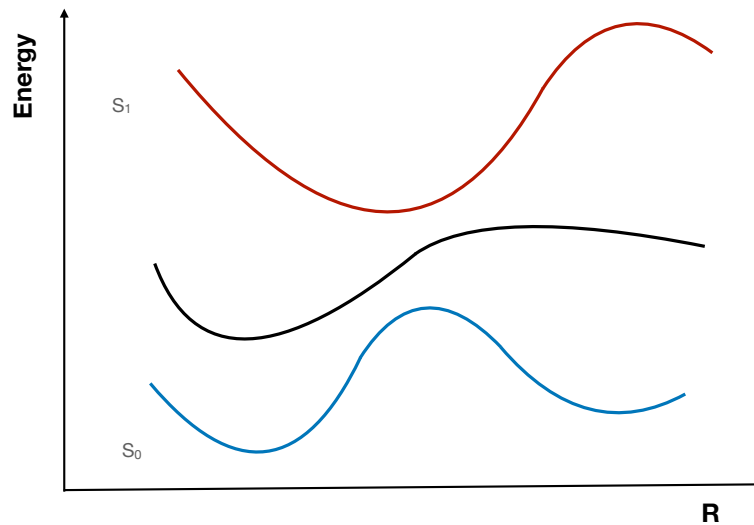


Figure 4.2: Ehrenfest approach

The Ehrenfest approach is based in the idea that the nuclei can be described classically and the electrons using quantum mechanics. With the system moves on a single potential

energy surface obtained by weighted averaging over all adiabatic states, as illustrated in Figure 4.2. This approach is the simplest of all the methods that seek to simulate non-adiabatic dynamics. This algorithm effectively incorporates several non-adiabatic effects.

The approximation fails when in situations involving tunnelling, or involving excited electronic states, particularly when states are nearby in energy. Conical intersections (or avoided crossings) break Ehrenfest, just as they break Born-Oppenheimer dynamics. Ehrenfest dynamics converge faster and better describe those systems in which the different excited states remain coupled throughout the dynamic. However, they are not suitable for the description of minor events during electronic relaxation, such as the activation of relaxation pathways with low probabilities and that give rise to secondary final photoproducts. Furthermore, nuclear motion continues to be described by the average of the contributions of each of the states even in regions of configuration space where they no longer remain coupled.

4.2.1 RT-TDDFTB EHRENFEST DYNAMICS

Because of the demanding task from a computational point of view to solve the TDSE, several approaches are employed, for instance: Multiconfigurational time-dependent Hartree (MCTDH), fewest-switches surface hopping (FSSH), Ehrenfest approach, etc. There are advantages and limitations in use each case mentioned as the number of degree of freedom that can be treated or the still demanding computational cost. In particular, the mean-field based Ehrenfest dynamics, in which the electrons are treated using quantum mechanics and the nuclei are described at the classical level, has been selected as an appropriate scheme for the current investigation.

The self-consistent SCC-DFTB formalism is used for the electronic structure description of the systems, the computation of the Hamiltonian, the overlap matrix elements, and the density matrix. The DFTB method is based on a localized non-orthogonal orbitals basis set, with semiempirical parameters. This framework has the advantage of being used to describe hundreds of atoms with accuracy and acceptable computationally. The derivation of the equations of motion for the wave function coefficients and the nuclear positions according to the Ehrenfest method for tight binding schemes have been previously published and discussed in great details. The following discussion is focus only in mainful details.

In this framework, the density matrix evolves in time following the Liouville-von-Neuman equation of motion, given by:

$$\frac{\partial \hat{\rho}}{\partial t} = -i(S^{-1}\hat{H}[\hat{\rho}]\hat{\rho} - \hat{\rho}\hat{H}[\hat{\rho}]S^{-1}) - (S^{-1}D\hat{\rho} + \hat{\rho}D^T S^{-1}) \quad (4.4)$$

where, $\hat{\rho}$ is the density matrix, \hat{H} is the Hamiltonian matrix depending on the density matrix, with the S^{-1} is the inverse of the overlap matrix, and D is the non-adiabatic coupling matrix and D^T is the transpose matrix of D . The matrix D is defined as $D_{\kappa\nu} = \langle \varphi_{\kappa} | \varphi_{\nu} \rangle$ where $|\varphi_{\kappa}\rangle$ and $|\varphi_{\nu}\rangle$ are a pair of atomic orbitals in a localised basis, in this case in the set used in DFTB+ scheme.

The equation 4.4 is integrated by the Leapfrog algorithm. The first part of the subtraction correspond with electronic terms and the second one with non-adiabatic terms. At each

electronic step, the time-dependent forces are computed and used to propagate the nuclei using the Verlet velocity algorithm. If the nuclei are fixed then the elements of the non-adiabatic are zero because the orbitals basis set are localized on the nuclei. Then, using the electronic terms in equation 4.4 for fixed nuclei can be employed to describe optical properties, as absorption spectra. To obtain the optical absorption spectrum of the system, an initial perturbation to the ground-state density matrix is applied with a Dirac-delta-pulse form perturbation:

$$\hat{H} = \hat{H}^0 + E_0 \delta(t - t_0) \hat{\mu} \quad (4.5)$$

where, \hat{H} is the Hamiltonian matrix, E_0 is the electric field applied, $\hat{\mu}$ is the dipole moment operator.

With the application of an small electric field pulse, the dipole moment can be described by the linear response regimen:

$$\mu(t) = \int_{-\infty}^{+\infty} \alpha(t - \tau) E(\tau) d\tau \quad (4.6)$$

where, $\alpha(t - \tau)$ is the polarizability along the axis over an electric field is applied. A Fourier transform is applied over the time dependent dipole moment, and the frequency dependent polarizability is taken using:

$$\alpha(\omega) = \frac{\mu(\omega)}{E_0} \quad (4.7)$$

The absorption spectra is proportional to the imaginary part of the frequency dependent polarizability. A damping function is applied to properly obtain a broadening of the peaks.

To study dynamic processes such as the photo-excitation of the system and photoinduced charge transfer processes, the laser-type perturbation is used. Basically, this perturbation simulates the action of a laser on a molecule or system as a monochromatic electric field that oscillates in time,

$$E(t) = E_0 \sin(\omega t) u \quad (4.8)$$

where E_0 is the intensity of the field, ω is the frequency with which we want to irradiate the system and u is the direction of polarization in which the laser is applied.

In the cases that a pulse-type perturbation laser is more appropriate,

$$E(t) = \begin{cases} E_0 \sin(\omega t) u \sin^2(\pi t / \tau) & \text{if } 0 \leq t \leq \tau \\ 0 & \text{if } t < 0 \text{ or } t > \tau \end{cases} \quad (4.9)$$

Where, starting at $t = 0$, τ is the final time of the pulse. In this way, the dynamics can be followed during the pulse and after it. After the pulse perturbation, the density matrix evolves in time following the Liouville-von-Neuman equation of motion described by equation 4.4. In this thesis, a pulse-type perturbation laser was used to study photoinduced charge-transfer dynamics, taking into account the experimental conditions.

4.3 SURFACE HOPPING

Instead of a single nuclear trajectory, a collection of trajectories is considered. Each of the nuclear trajectories will evolve on a single adiabatic surface, being able to jump to other surfaces, having behaviors as illustrated in the Figure 4.3. The SH trajectories by themselves have no physical meaning and many simulations are necessary for the result to acquire statistical validity. The collection of all trajectories are proceeded, obtaining an effective trajectory. In this way, an asymptomatic adiabatic behavior is always obtained, and non-adiabatic effects are considered thanks to the jumps between the adiabatic potential surfaces.

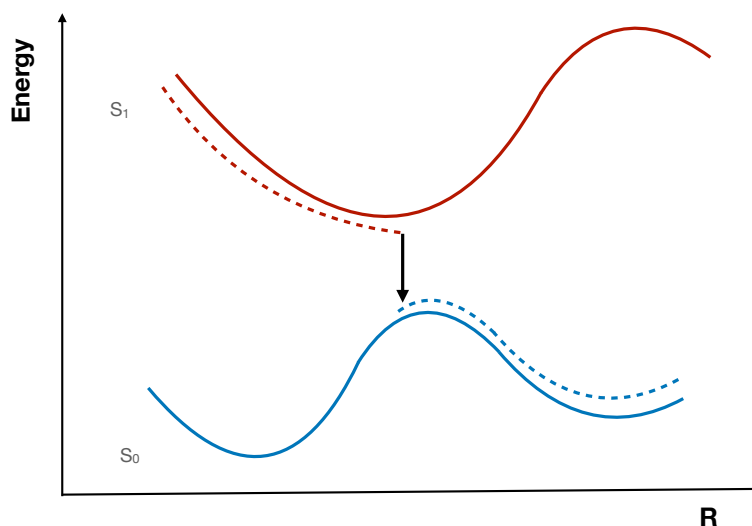


Figure 4.3: Surface Hopping method

The Fewest Switches Surface Hopping (FSSH) algorithm developed by Tully is one of the most popular approaches to perform nonadiabatic dynamics.⁵⁵ The jump criterion can be derived from the following two assumptions; first, we seek to have a number of paths on

each surface in such a way that the number of paths on each surface coincides at all times with the probability of being on that surface. The second assumption is that it is sought to have a minimum number of jumps between surfaces. When the system jumps from one state to another, it will clearly have a different energy (unless the energy of both states is degenerate). It is because of this that, in order to force the method to follow the conservation of energy, when a jump is made the nuclear speed is going to be adjusted in such a way that the energy is the same before and after the jump, since these jumps are related to the non-adiabaticity of the system. It could be said that Tully's method⁵⁵ splits the wave function in such a way that it propagates independently to each piece, to finally put everything back together, thus obtaining a globally quantum behavior. A set of packages with Surface Hopping implementations are PYXAID⁶⁷, NEXMD⁶⁸, Hefei⁶⁹, Libra⁷⁰, NEWTON-X⁷¹, among others. Many variants including decoherence are also available.

The SH method requires more trajectories to reach the convergence of the results and is not suitable for describing those systems in which the different excited states remain coupled throughout the dynamics. Furthermore, it suffers from inaccuracies related to forbidden jumps, energy redistribution after an effective jump, and electronic coherence, among others. However, it is more suitable for analyzing vibrational energy fluxes associated with specific excited states and can distinguish between different relaxation paths that occur simultaneously. Another disadvantage is that there is no clear way to incorporate nuclear quantum effects in the context of SH.

It doesn't matter how beautiful your theory is, it doesn't matter how smart you are. If it doesn't agree with experiment, it's wrong.

Richard P. Feynman

5

Photoinduced charge transfer in functionalized Gold Nanoclusters

THE MAIN PURPOSE OF THIS CHAPTER is to discuss light-driven charge transfer processes on pyrene labeling Gold Nanoclusters.^{72,73} Unraveling the unclear mechanism involved using RT-TDDFTB Ehrenfest dynamics. The results presented follow references 72,73

5.1 PHOTOINDUCED CHARGE TRANSFER IN PYRENE-FUNCTIONALIZED THIOLATED GNC

The attention on the chemistry of gold and the interest about gold complexes has been of a great importance for centuries. From alchemy to modern times with the description of physical chemistry properties of gold nanoclusters (GNC). Being today a hot topic and research focus of material science.^{17,18,19,20,74} Since the paper on 1857 by Michael Faraday⁷⁵ about the interaction of light with gold complexes in solution to current times the curiosity remains intact. Nowadays, the studies on photodevices and nanophotonics are growing with an special focus on photoinduced charge transfer processes. One clear example is the experimental work developed by M.S. Devadas et al⁷⁶ describing the ability of a Au₂₅-based GNC acting as an electron donor. In this experimental paper was probed the interfacial photoinduced charge transfer processes between the GNC and a pyrene derivative ligand, within 580 fs. The electrochemical and ultrafast time-resolved fluorescence and absorption techniques employed are of a great value but the understanding of mechanism involved still unclear. In this sense, the theoretical modeling is an strong key in the description of photoinduced events and the prediction and designing of systems at nanoscale.

The main objective of this first section is to understand the photoinduced charge transfer processes described by the experimental work of M.S. Devadas et al.⁷⁶ by using RT-TDDFTB Ehrenfest dynamics. A second objective is the description of the role of the ligand protected groups in the charge separation. And finally, a theoretical design and a based proposition of related systems with better performance on the photoinduced charge transfer. The systems under study are represented in Figure 5.1.

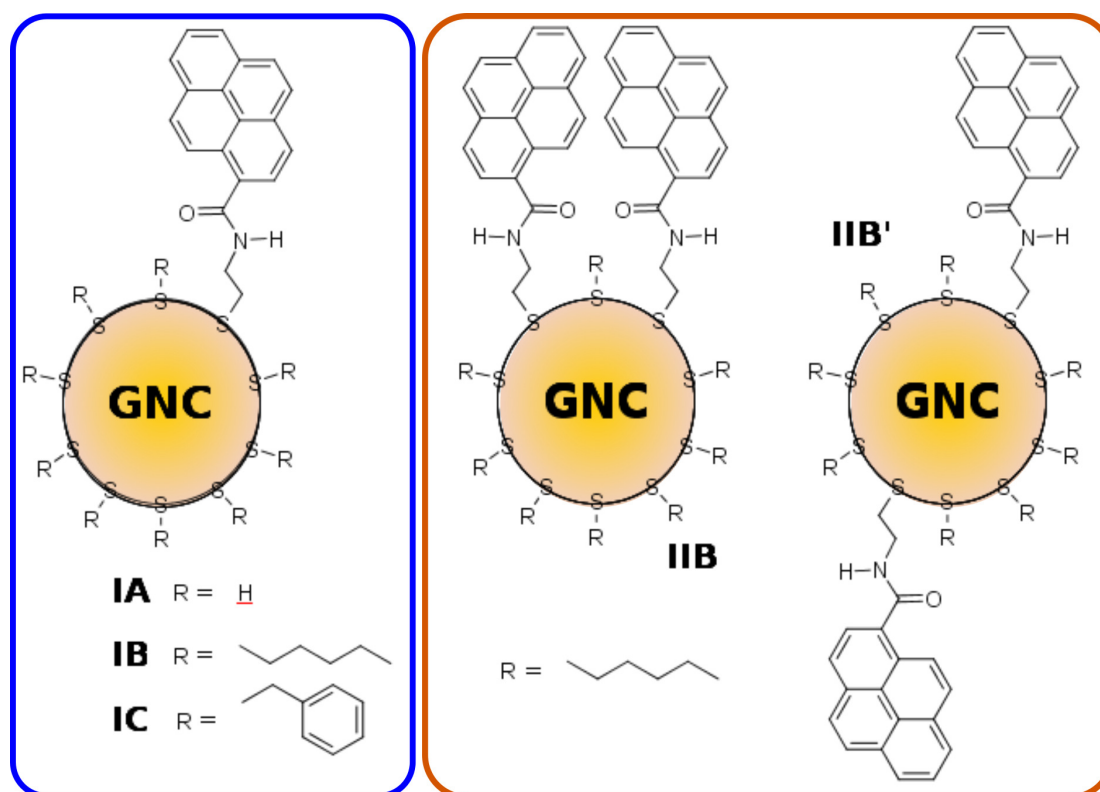


Figure 5.1: Schematic representation of the systems studied in the present work. On the left side, $[\text{Au}_{25}(\text{SR})_{17}\text{SPyr}]^{-}$, i.e., one pyrene molecule attached to the gold nanocluster $[\text{Au}_{25}(\text{SR})_{18}]^{-}$ (GNC) with different protecting groups R: H, hexyl and phenylethyl for IA, IB and IC, respectively. On the right side, two newly designed systems with pyrene molecules attached in two different positions.

The DFTB calculations have been performed using the DFTB+ code.⁴⁶ The *auorg*⁷⁷ set of DFTB parameters have been used. To obtain the absorption spectra by the RT-TDDFTB approach, the electric field intensity used is 0.001 V/\AA and with the propagation of 82684 steps and a time step of 0.0024 fs , in the linear response regime. The Ehrenfest dynamics have been performed by applying a \sin^2 shaped pulse for the electron dynamics during the photoexcitation with an electric field value of 0.1 V/\AA and an energy laser value of 400 nm (expressed in eV units equal to 3.09). The total duration of the pulse is 100 fs in all cases. The Verlet algorithm is employed for the nuclei evolution during the dynamics.

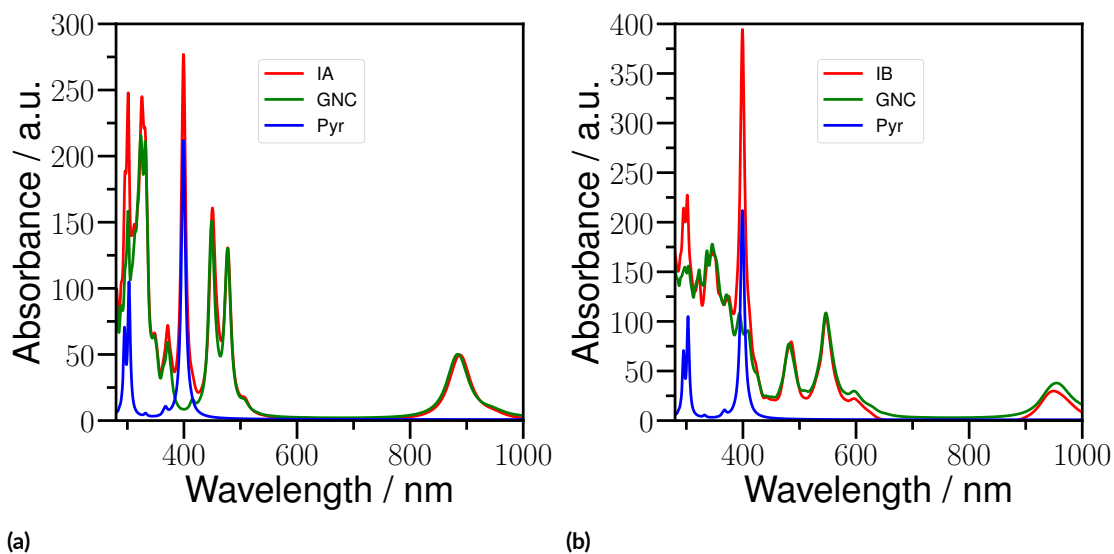


Figure 5.2: Absorption spectra for: (a) IA system. (b) IB system.

The Figure 5.2 displays the absorption spectra obtained for the systems IA and IB. Let's start to analyze the system IA displayed in Figure 5.2a. The total absorption spectra is formed by the sum of the individual parts corresponding to the GNC, the protecting groups (in this case H) and the pyrene. At 400 nm a high absorption peak belonging to the pyrene unit is obtained. The theoretical results here are in accordance to the experimental report by Dedavas et al.,⁷⁸, confirming the no presence of ground state interactions between the individual parts. Similar conclusions for the system IB are displayed in Figure 5.2b, in this case with the C_6H_{13} chains as protecting groups. In a direct comparison between the absorption spectra obtained for system IA and IB, the only difference is an red-shift of the bands corresponding to the GNC constituent. The rest of the systems under study in this section are considered in Figure 5.3. The maximum absorption band is illustrated at 400 nm corresponding to the pyrene unit. This value is considered as the energy value for the initial photoexcitation in all cases.

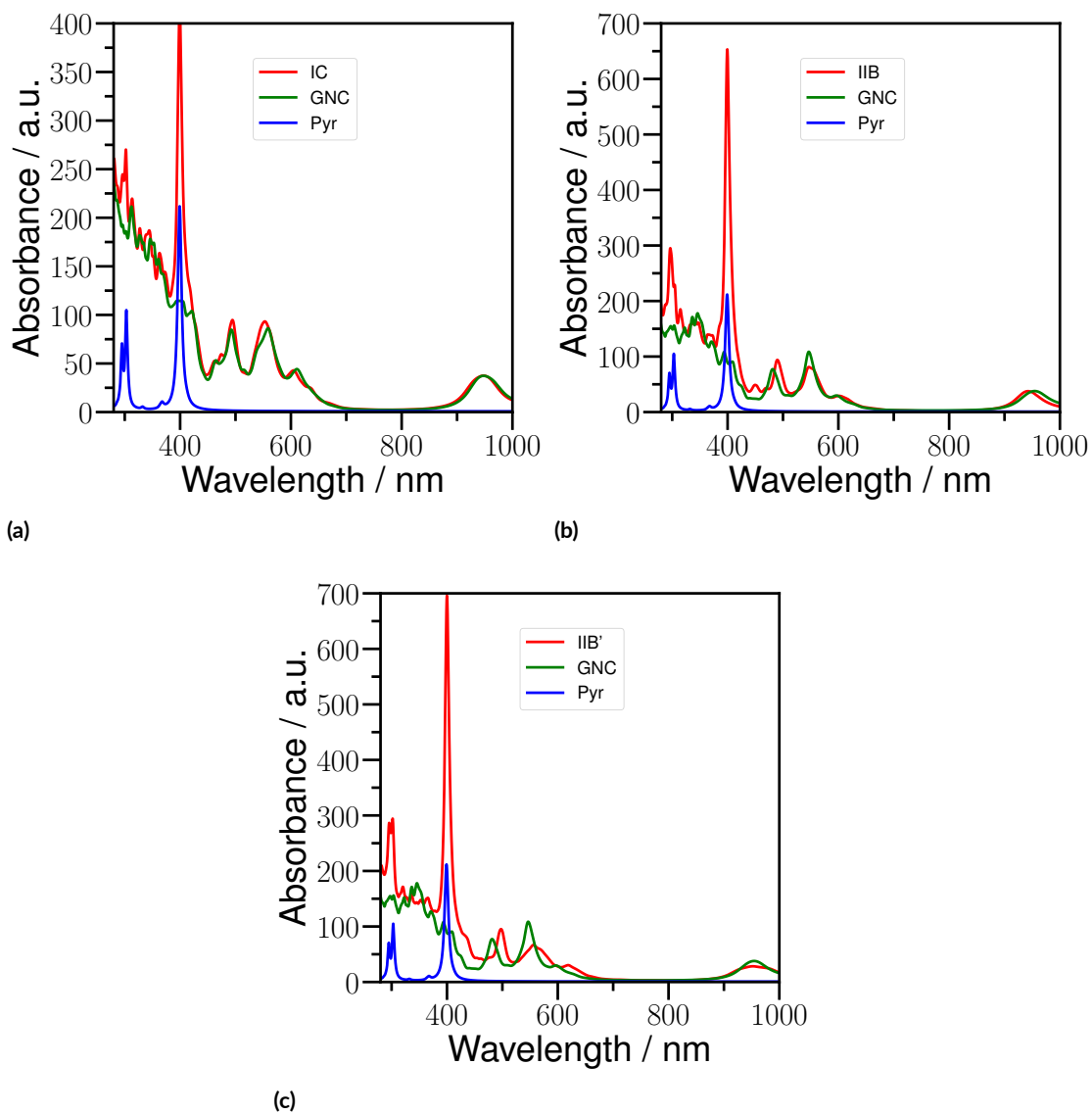


Figure 5.3: Absorption spectra for: (a) IC system. (b) IIB system. (c) IIB-prime system.

In experiments is reported the maximum excitation band of the pyrene unit at 345 nm.⁷⁸ This discrepancy in numerical values between the theoretical obtained and the experimental

findings are due to the limitations on the theoretical modeling regarding the no consideration of the solute-solvent interactions.⁷⁹ Take in to account that the theoretical calculations are carried out in the gas phase at 0K. Another factor to consider is that the DFTB based calculations are strongly related the DFTB parametrization used. By employing the the *auorg*⁷⁷ parameter set created with GGA functional some errors related to the no inclusion of a range-separation term can be a source of uncertainty. In a previous DFT research about the optical properties of the systems in consideration here, the results obtained are more accurate by using a more sophisticated functional considering range-separation term, in opposite to the GGA functional results with bands at lower energies.⁸⁰ For the future study of π -conjugated chromophore labeling Gold based systems, a possible development of DFTB parameters should correct this issues (unfortunately is not available for the systems containing Au and S) as presented for other atomic systems using range-separated type of functional, recently.⁸¹ In general, the RT-TDDFTB approach employed here obtain at a low computational cost with a good performance the absorption profile of the systems considered in accordance to previous DFT calculations and experimental results.

The charge separation illustrated in Figure 5.4 underlines an ultrafast photoinduced charge transfer in the dynamics, at the initial 100 fs (the pulse duration used). The Ehrenfest dynamics was performed using 0 K as Temperature value. For systems IA and IB, the pyrene unit displays an acceptor behaviour, with the GNC curve reproducing a donor character. These results are in accordance with the experimental findings reproduced by Devadas et al.⁷⁸ The system IA denotes a decreasing tendency after the first 300 fs. The system IB shown an stationary charge-separated state during the time window reproduced with the dynamics. These results are of a great importance because is underlying the presence of the hexyl chains in the stabilization of the charge separation after excitation. The role played by the chains

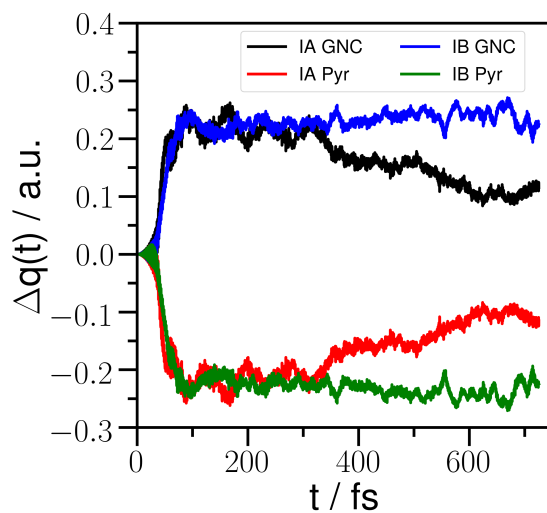


Figure 5.4: Δq as a function of time for IA and IB systems under study.

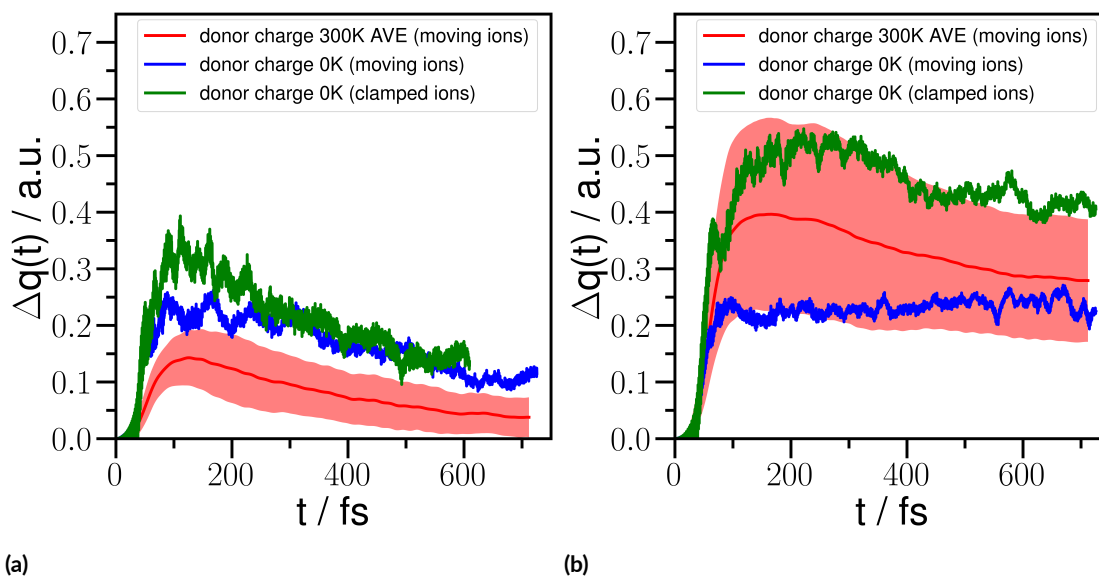


Figure 5.5: Changes in the Mulliken charges with respect to their ground-state values as a function of time for the donor cases, IA system (a) and IB system (b). Green curve corresponds with the electron dynamics at 0K. Blue curve represents the Ehrenfest dynamics at 0K. And red curve is the average obtained from the Ehrenfest dynamics at 300K for the decorrelated sampling configurations, with the red transparency as the standard deviation obtained, respectively, for each case under study.

ligands in the charge transfer mechanism is analyzed in more details later.

The photoinduced charge separation for systems IA and IB and the role of alkyl ligands and Temperature effects on the charge transfer mechanism involved is analyzed in Figure 5.5 (The donor character is represented for simplicity). The Ehrenfest dynamics results about the behaviour corresponding to clamped and moving ions are displayed by the green and blue curves, respectively. The nuclear motion should not affect the charge transfer involved as denoted Fig. 5.5a for system IA and H as protecting ligands. Similar conclusion for the system IB and the hexyl chains as protecting ligands is denoted in Figure 5.5b. The difference for the IB system is the decreasing on the total steady-state charge transferred, approximately by half. In our opinion, this behaviour is due to the presence of a new relaxation channel as more nuclear degrees of freedom are added in the case for the simulations including moving ions. The steady-state is reached sooner, with the increase of detuning between the electronic states involved on the charge transfer as reported in a previous work on nanodiamond/dye complex.⁸²

The effect of Temperature is highlighted by the red curves in Figure 5.5. The mean charge transfer value is obtained from a set of Ehrenfest dynamics performed on a sample of 25 configurations. These configurations were selected from a Born-Oppenheimer molecular dynamics using NVT ensemble at 300 K. The configurations used are decorrelated. More details can be referred in the Appendix B. The charge separation reported before is collected in all the cases sampled. This result underlines the no dependency of the process involved with the molecular geometry employed.

A comparison between the curves obtained for the cases of clamped and moving ions

curves (performed at 0 K) and the mean curve (performed at 300 K) presents a lower total charge separation as displayed in Figure 5.5a. The effect of the Temperature here for system IA denotes a decrease on the charge separation. In the case of system IB analyzed in Figure 5.5b, with the increase of Temperature in the Ehrenfest dynamics, the charge separation is bigger if compared to the curve corresponding to moving ions at 0 K. The initial stages of the dynamics even display a bigger difference, from 100 fs to 400 fs. The analysis performed from the Temperature effects in the dynamics is proposing the idea that the contribution of the nuclei movement at early stages of the photoinduced charge separation is important in the presence of alkyl chains as protecting ligands.

At this point, the study of the role of ligands in the charge separation performance is the main focus of the discussion. In Figure 5.6 is analyzed in details. The Figures 5.6a and 5.6b correspond to the charge separation analysis for system IA and IB using one conformation of the sampling performed at 300 K, respectively. In the case of Figure 5.6b is presented an analysis of the individual contributions of the GNC core, alkyl chains and pyrene unit. The alkyl chains are acting as donor mainly, with the GNC core with an initial donor character (at the start of the dynamics) and presenting an acceptor behaviour afterwards. In our opinion, the data exposed is clearly supporting a three-step mechanism for the system IB studied here. First step, a preparation step corresponding to the photoexcitation of the pyrene residue (approximately 30 fs). A second step, in which charge is directly transferred from the GNC core to the pyrene residue (approximately from 30 fs to 100 fs). And the last step, after approximately 100 fs in the dynamics, with the stabilization of the charge mediated by the alkyl protecting ligands with the charge transfer to the GNC and pyrene unit. The last step is crucial to underline the importance of the protecting ligands and the role played, with a donor character as reported and observed by the experimental findings of Dedavas et al.⁷⁸.

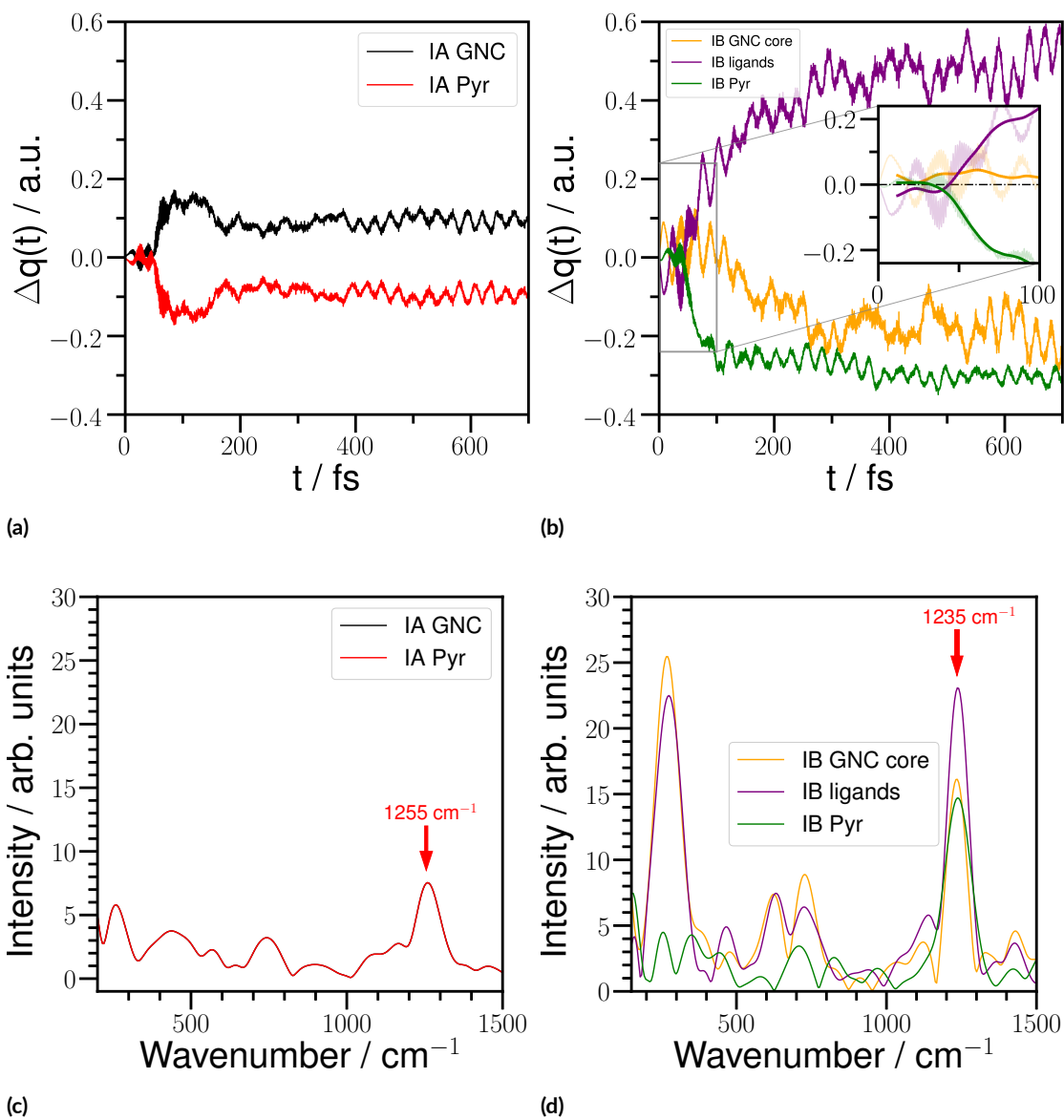


Figure 5.6: (Up) Δq as a function of time for one single frame from the NVT assemble presented in Fig. 5.5 for IA (a) and IB (b). (Bottom) Fourier intensity spectrum of the charge-transfer dynamics obtained above for the system IA (c) and IB (d).

The mechanism proposed can be extended to the results analyzed before to the Ehrenfest dynamics performed at 0 K, displayed in Figure 5.4.

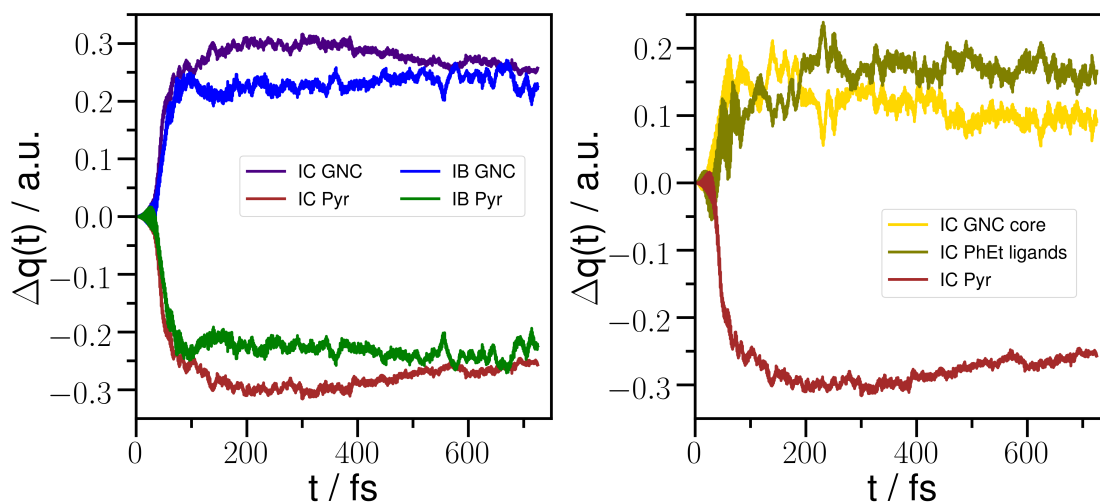
The Ehrenfest dynamics analyzed in Figures 5.6a and 5.6b also exhibit oscillations corresponding to a few tens of femtoseconds. The nature of these oscillations can be clarified by a Fourier transform analysis of the dynamics as discussed by Rozzi⁸³ and Falke⁸⁴ previously. The spectrum obtained for each corresponding case is presented in Figures 5.6c and 5.6d, respectively. In Figure 5.6d for system IB an intense signal at $\sim 1235 \text{ cm}^{-1}$ is displayed. This peak is associated to the C-C stretching mode of the hexyl ligands. It is also found as presented in Figure 5.6c for system IA a peak at $\sim 1255 \text{ cm}^{-1}$ attributed to the C-C stretching mode corresponding to the linker group of the pyrene unit. The lower intensity is due to the small number of C-C presented in system IA if compared to the system IB. In Figure 5.6d, more intense bands of interest are observed at $\sim 280 \text{ cm}^{-1}$ related to Au-S stretching modes and Au-S-C bending modes. With the bands in the region $600\text{-}800 \text{ cm}^{-1}$ corresponding to C-S stretching modes.^{85,86,87,88} The presence of these bands is underlying the coupling between the GNC core and the hexyl protecting chains. The presence of alkyl ligands as protecting groups is the principal cause on the peaks intensity. The presence of the alkyl chains is denoting a charge transfer mechanism involving vibronic couplings, highlighting the role of the alkyl protecting ligands. The photoinduced charge transfer has a contribution not only of the C-C, Au-S and Au-S-C vibrational modes of the system but also by the influence of Temperature in the Ehrenfest dynamics study as discussed above in Figure 5.5.

The interpretation and confirmation of the experimental observations on the photoinduced charge transfer described above conduct to perform simulations on the prediction on new labeled GNC. The idea is to explore the effect of new protecting ligands by replacing the C_6H_{13} ligand. The system IB demonstrated the interesting role of the protecting ligands

and the importance on the light-driven charge separation. The synthesis of new GNC with different protecting groups is well reported in literature.⁸⁹ At this point, the phenyl-ethyl (PhEt) units as ligands is an excellent candidate (system IC), and reported in GNC synthesis.⁹⁰

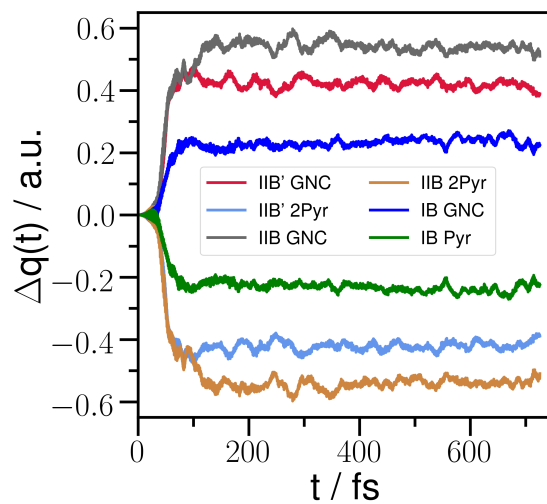
The absorption spectra of the system IC (see Figure 5.3a) is quite close to the one obtained for system IB, with an intense peak at 400 nm of the pyrene residue, and without the presence of ground-state interactions with the GNC. In Figure 5.7a is displayed the results about the photoinduced charge separation of the system IC, illustrating the ultrafast nature with stabilization on the charge separation after approximately 100 fs. The acceptor role of the pyrene unit and the GNC as donor are similar to the results obtained for system IB. For comparison purposes, the results corresponding to system IB are displayed as well in Figure 5.7a about the Ehrenfest dynamics results at 0K. In order to unravel the effect of the PhEt ligands, in Figure 5.7b is exhibited the individual contributions. In system IC, GNC core is acting as donor during the charge separation, being completely different behaviour that the one displayed by system IB above. This behaviour slightly differs from the mechanism proposed before for system IB. Then, in the case of system IC, the GNC core and the PhEt protecting ligands act as direct donors to the acceptor pyrene in the time window studied in the dynamics. It is important to mention that the PhEt ligands is not changing the charge transfer direction or the efficiency of the photoinduced process. As illustrated in Figure 5.7a, both systems IB and IC present a similar charge separation profile. The remarkable point, it is the fact that the GNC core is acting as electron donor in the case of presence of PhEt as protecting ligands, and as electron acceptor in presence of alkyl chains. The results underline the essential idea about the consideration of the protecting ligand shell on the designing of photodevices.

Following the previous idea, it is of a great interest about considering the number of chro-



(a)

(b)



(c)

Figure 5.7: (a) Δq as a function of time for the IC system. (b) Contribution analysis for the Δq as a function of time for the IC system. (c) Δq as a function of time for the IIB and IIB' systems and compared with the IB study case.

mophores on the photoinduced charge transfer process. During the experimental synthesis is possible to control the number of chromophores groups attached to GNC by the control of ligand exchange reactions.⁹¹ Then, to continue with the simulations, a GNC labeled with two pyrene units will be investigated. Two different configurations will be considered as presented in Figure 5.1. The two pyrene units are placed on neighbor positions (IIB) or on opposite sites (IIB'). Like the other cases under study here, the intense band at 400 nm corresponds to the pyrene unit, and the systems IIB and IIB' do not present ground-state interactions with the GNC.(see Figures 5.3b and 5.3c) With the inclusion of a second pyrene unit, an hyperchromic effect is observed in the increase of the absorbance peak at 400 nm.

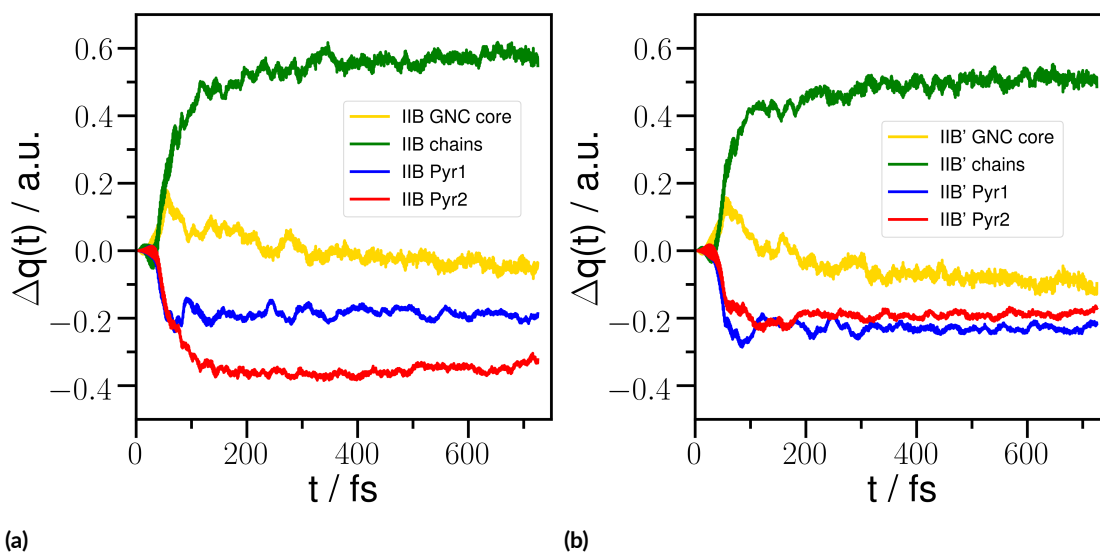


Figure 5.8: (a) Contribution analysis for the Δq as a function of time for the IIB system. (b) Contribution analysis for the Δq as a function of time for the IIB' system.

In Fig. 5.7c are displayed the results obtained Ehrenfest dynamics at 0 K for systems IIB and IIB'. The pyrene unit contribution on the charge separation is considered the two pyrene units altogether in these cases. The charge separation illustrates the GNC acting as

donor with the pyrene as acceptor (a charge transfer from GNC to pyrene) after 100 fs. Once more, an ultrafast nature is reported with no back charge recombination for the time studied in the dynamics. In a direct comparison with system IB, the total charge separation is close to two times bigger. In fact, system IIB presents a better charge separation than system IIB'. With the addition of a second pyrene unit, an increase on the charge separation is observed, depending as well on the position of the labeling.

To understand the higher charge separation of the IIB and IIB' systems, in Figure 5.8 are displayed for each corresponding case the individual contributions. The pyrene units presented in system IIB in neighbor positions are of higher acceptor character compared to the system IIB' with the pyrene units in each side of the GNC. In details, in system IIB, the two pyrene units exhibit a different contribution with one pyrene unit with superior acceptor behaviour. It seems that the direction on the functionalization matters on the photoinduced charge separation, with system IIB presenting the best performance. A more efficient charge transfer process is obtained by increasing the number of chromophores. In our opinion, these key factors are of paramount important in the designing and development of GNC based photodevices.

5.2 IMPACT OF VIBRONIC COUPLING EFFECTS ON LIGHT-DRIVEN CHARGE TRANSFER IN PYRENE-FUNCTIONALIZED MIDDLE AND LARGE-SIZED METALLOID GNC

The interest on metalloid GNC has been increasing and new large-sized and middle-sized structures were reported, recently.^{92,93} The synthesized large-sized $\text{Au}_{108}\text{S}_{24}(\text{PPh}_3)_{16}$ presents a core-shell description by an octahedral Au_{44} core enclosed by an $\text{Au}_{48}\text{S}_{24}$ shell with addi-

tional 16 Au(PPh₃) units.⁹² The second synthesized middle-sized Au₇₀S₂₀(PPh₃)₁₂ is characterized by an octahedral of Au₂₂ core surrounded by an Au₄₈S₂₀(PPh₃)₁₂ shell, with an overall tetrahedral symmetry.⁹³ These structural features are very attractive because they present an (AuS)₄ ring motif⁷⁴ instead, of the typical Au-S staple motif of the thiol protected GNC. With the core formed by Au atoms covered by PPh₃ groups except in the positions of the (AuS)₄ ring motif is a good reference for ligand exchange reactions and the possibility of featuring with linker molecules in the functionalization of GNC.

Previous DFTB calculations has been employed in similar studies of photoinduced charge-transfer in different compounds.^{72,94,95,96,97,98} In this context, with the reported studies on the novel metalloid GNC^{92,93}, and the newest DFTB parametrization by Irle et. al.⁹⁴ as inspiration, the present study is focus on the photoinduced charge-transfer on the novel metalloid gold-phosphine nanoclusters mentioned above labeled with a pyrene residue. In Figure 5.9 a representation of the systems considered in this study is presented. Being this study, in the best of my knowledge, the first time that excited-state calculations on these novel compounds is described.

In a theoretical work developed by Chadwick A. Tolman in the decade of the 70's of the last century, the electronic and steric properties of tertiary phosphines (PR₃) was quantified by introducing a parameter depending on the nature of the R groups in the PR₃ ligand, the π -acceptor capacity.⁹⁹ For the system under study in the present section, a central question here is about the π -acid character: What is the effect on the photoinduced charge transfer by varying the R group of the phosphine ligands? Following the Tolman electronic parameter (TEP)⁹⁹, in this work are considered triethyl phosphine (P(C₂H₅)₃), trimethyl phosphine (P(CH₃)₃), triphenylphosphine (PPh₃), and phosphine (PH₃). The π -acceptor capacity is

following the order: $\text{PH}_3 > \text{PPh}_3 > \text{P}(\text{CH}_3)_3 > \text{P}(\text{C}_2\text{H}_5)_3$.

A main objective is to elucidate if the order presented above of the introduced Tolman electronic parameter is modified by the excited-states properties and the importance to consider a parameter describing steric effects, the Tolman cone angle⁹⁹, for the ligands under consideration. Following the suggested Fourier transform analysis by Rozzi et al.⁸³, Falke et al.⁸⁴ and discussed in a recent publication⁷² in this section valuable details on the vibronic couplings and the elucidation of the mechanism involved are highlighted.

The metalloid GNC structures used were taken from the literature.^{93,94} For the pyrene labeling, an R group was substituted by the pyrene derivate ($-\text{CH}(\text{O})\text{NHCH}_2\text{CH}_3$ linker with the pyrene ring) and attached to a phosphine group. The geometries were relaxed at

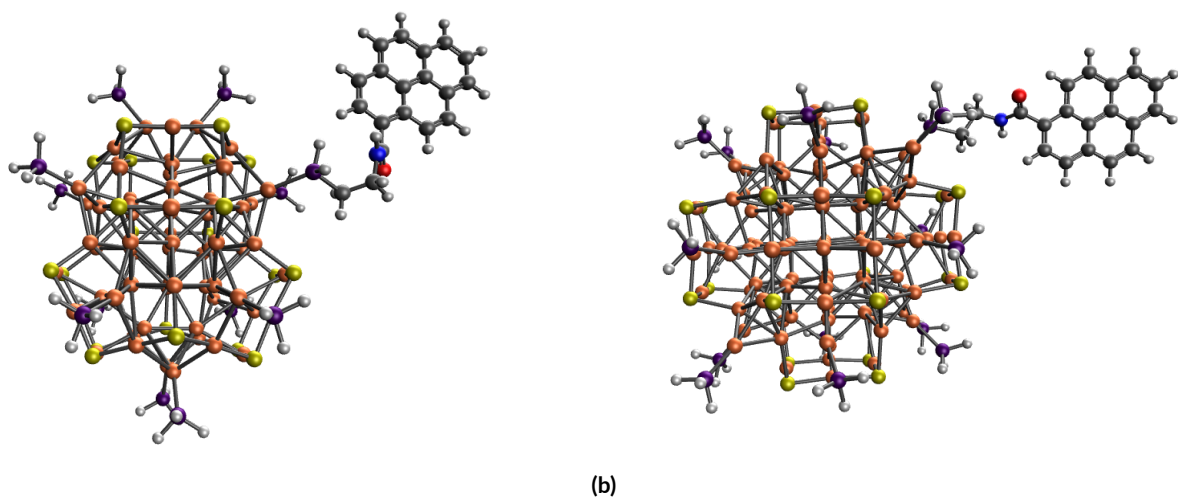


Figure 5.9: Molecular structure for: (a) $\text{Au}_{70}\text{S}_{20}(\text{PH}_3)_{15}\text{PH}_2\text{Pyr}$ and (b) $\text{Au}_{108}\text{S}_{24}(\text{PH}_3)_{15}\text{PH}_2\text{Pyr}$ systems. The orange, yellow, purple, red, blue and white represent the Au, S, P, O, N and H atoms, respectively. For simplicity and clarity the graphical representation of the rest of the systems under study are omitted.

the DFTB level of theory using the DFTB+ code.⁴⁶ A complete DOS and PDOS analysis of the systems of interest can be found in Appendix C. The set of DFTB parameters recently published for the description of the interactions of gold-phosphine⁹⁴ have been used. In the computation of the absorption spectra, an electric field intensity of 0.001 V/\AA is employed with the propagation of 82684 steps using a time step of 0.0024 fs , in the linear response regime. For the Ehrenfest dynamics, an electromagnetic wave, a \sin^2 shaped pulse is employed describing the electron dynamics during the light absorption with an electric field of 0.1 V/\AA and an energy laser of 400 nm (expressed in eV units equal to 3.09). The total duration of the pulse is 100 fs in all cases. For the nuclei evolution in the Ehrenfest dynamics based on the Verlet algorithm, a Temperature of 300 K is used.

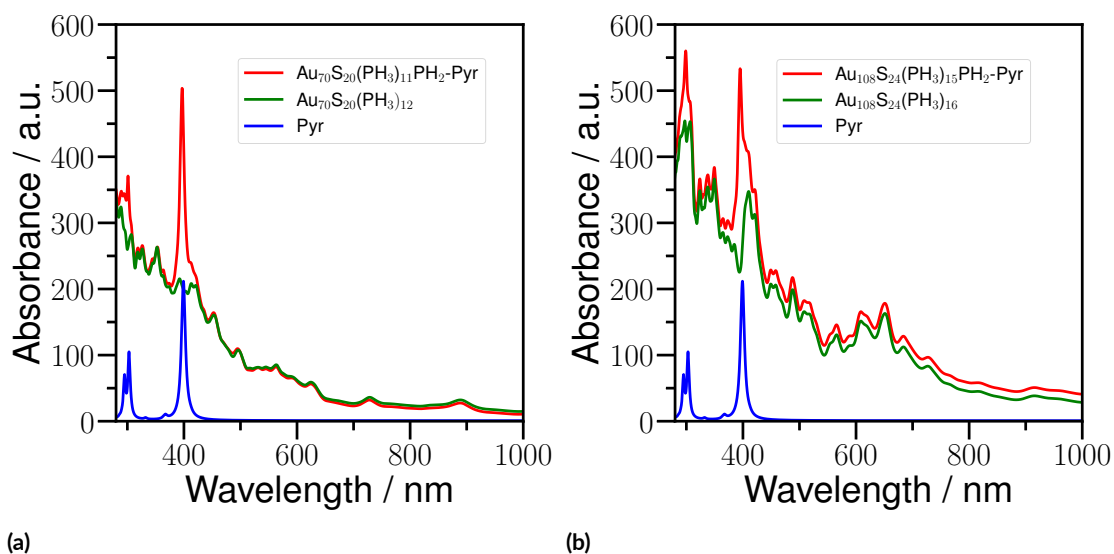


Figure 5.10: Absorption spectra obtained respectively, using RT-TDDFTB approach for the systems: (a) $\text{Au}_{70}\text{S}_{20}(\text{PH}_3)_{11}\text{PH}_2\text{Pyr}$, (b) $\text{Au}_{108}\text{S}_{24}(\text{PH}_3)_{15}\text{PH}_2\text{Pyr}$

In Figure 5.10 the absorption spectra of $\text{Au}_{70}\text{S}_{20}(\text{PH}_3)_{11}\text{PH}_2\text{Pyr}$ and $\text{Au}_{108}\text{S}_{24}(\text{PH}_3)_{15}\text{PH}_2\text{Pyr}$ is displayed. Clearly, an absorption peak corresponding to the pyrene residue is denoted at

400nm. This theoretical result has been announced before for thiolated GNC labeled with pyrene.⁷² Another publication reporting UV-Vis spectrum for gold-phosphine complexes using TD-DFT calculations reported as well a red-shift with a discrepancy of around 100-150nm from experimental findings.¹⁰⁰ For gold systems this behaviour is considered a typical one.^{101,102} The theoretical description here does not take into account solute-solvent interactions in the calculations. In my opinion, this limitation of the theoretical approach employed is the cause of a bathochromic effect. As mentioned in the previous section of this chapter, the experimental observations of Devadas et al.⁷⁶ compared to the theoretical work developed as complement describe a similar result. A full analysis about the individual contributions in the total absorption spectra for each case denotes that no ground-state interactions are presented, having the total absorption equal to the sum of the individual parts.

In Figure 5.11 the Ehrenfest dynamics results about the photoinduced charge transfer corresponding to $\text{Au}_{70}\text{S}_{20}(\text{PH}_3)_{11}\text{PH}_2\text{Pyr}$, and $\text{Au}_{108}\text{S}_{24}(\text{PH}_3)_{15}\text{PH}_2\text{Pyr}$ systems are displayed. The Figures 5.11a and Figure 5.11c present the charge separation obtained. The donor character is denoted with the purple curve and the acceptor contribution by the green curve, denoting the acceptor character of the pyrene residue. Clearly, an ultrafast and irreversible nature of the charge-transfer mechanism is denoted. The $\text{Au}_{70}\text{S}_{20}(\text{PH}_3)_{11}\text{PH}_2\text{Pyr}$ system presented in Figure 5.11a is displaying a better charge-separation compared to the $\text{Au}_{108}\text{S}_{24}(\text{PH}_3)_{15}\text{PH}_2\text{Pyr}$ system displayed in Figure 5.11c. For a deeper analysis on the mechanism involved, it is opportune to perform an analysis of the individual contributions of the components conforming the $\text{Au}_{70}\text{S}_{20}(\text{PH}_3)_{11}\text{PH}_2\text{Pyr}$ system and $\text{Au}_{108}\text{S}_{24}(\text{PH}_3)_{15}\text{PH}_2\text{Pyr}$ system in Figures 5.11b and 5.11d. First, describing the case of $\text{Au}_{70}\text{S}_{20}(\text{PH}_3)_{11}\text{PH}_2\text{Pyr}$ system in Figure 5.11b, an acceptor behaviour of the GNC core (blue curve) and a donor behaviour of the protecting ligands (red curve). Second, the description of the individual con-

tributions corresponding to the $\text{Au}_{108}\text{S}_{24}(\text{PH}_3)_{15}\text{PH}_2\text{Pyr}$ system in Figure 5.11b does not display a full donor-acceptor behaviour to the GNC and H protecting ligands, presenting

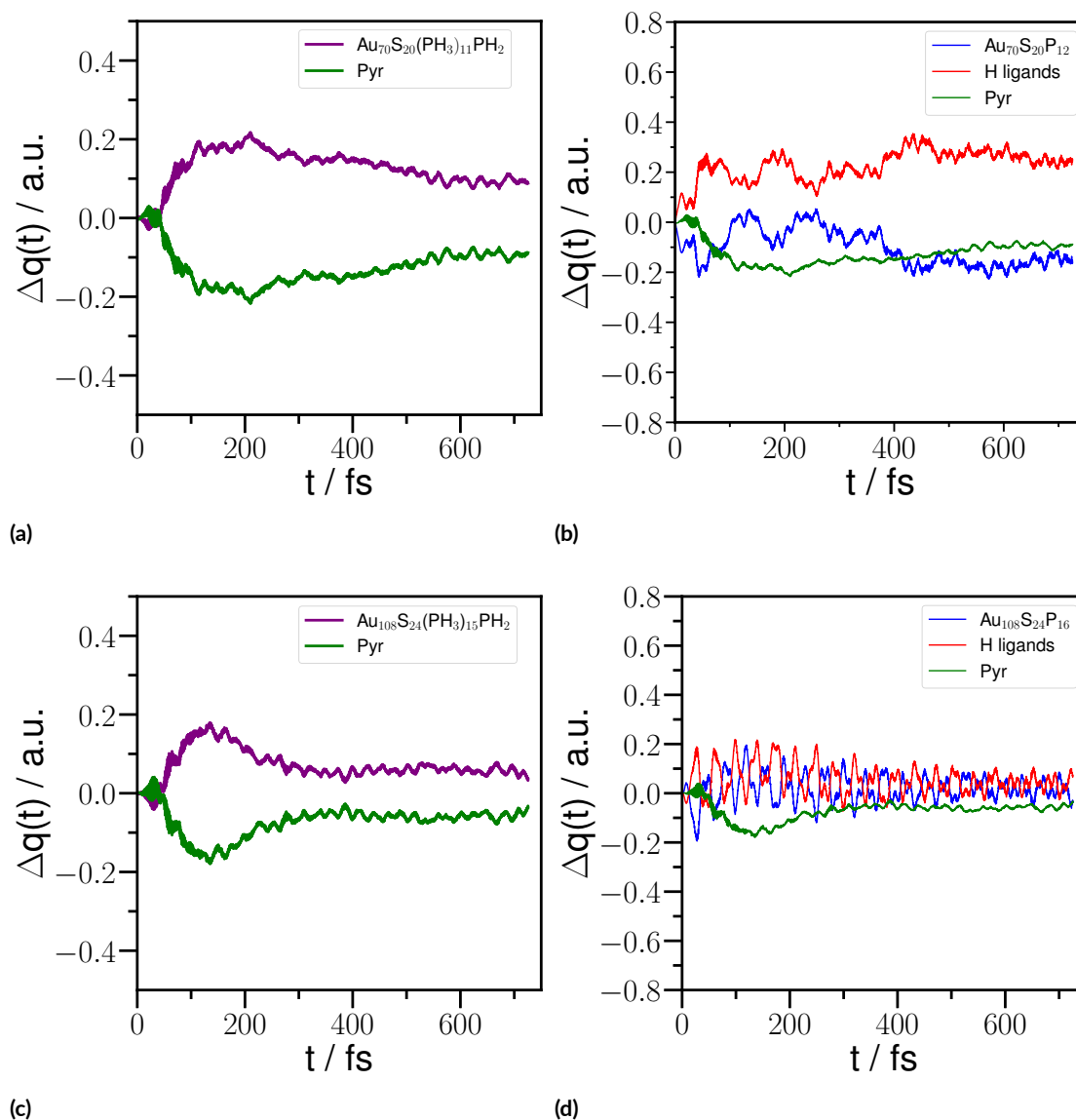


Figure 5.11: Changes in the Mulliken charges with respect to their ground-state values as a function of time: (a) $\text{Au}_{70}\text{S}_{20}(\text{PH}_3)_{11}\text{PH}_2\text{Pyr}$ and (c) $\text{Au}_{108}\text{S}_{24}(\text{PH}_3)_{15}\text{PH}_2\text{Pyr}$, with (b) and (d) displaying the individual contributions, respectively.

fluctuations during the investigated time of the dynamics.

The superior performance about the charge separation of $\text{Au}_{70}\text{S}_{20}(\text{PH}_3)_{11}\text{PH}_2\text{Pyr}$ system compared to $\text{Au}_{108}\text{S}_{24}(\text{PH}_3)_{15}\text{PH}_2\text{Pyr}$ system is obtained. This result is very important because it introduces the idea of an optimum GNC size. Experimental studies based on middle-sized GNC should be performed to highlight more this advantage. The P-H bending vibrational mode role is the fundamental reason in the behaviour denoted. A Fourier transform analysis of the Ehrenfest dynamics carried out is shown in Figure 5.12. The P-H bending vibrational mode is displayed at 950 cm^{-1} . A higher contribution on $\text{Au}_{108}\text{S}_{24}(\text{PH}_3)_{15}\text{PH}_2\text{Pyr}$ system is an efficient channel of relaxation on the charge transfer. The presence of vibronic couplings during the dynamics is fundamental in the charge separation.¹⁰³ In conclusion, increasing the size of the GNC does not contribute to a higher performance in the light-driven charge separation.

Continuing with the analysis of the rest of the systems involving phenyl, methyl and ethyl ligands as protecting ligands in Figure 5.13 the absorption spectra for the systems is shown. Similar conclusions to the absorption spectra analysis discussed above are highlighted. In all cases, an intense peak at 400 nm is displayed and it belongs to the pyrene residue. This value is the energy used for the laser pulse excitation on the Ehrenfest dynamics study. And the same computational details described above are employed for these systems.

The photoinduced charge transfer displayed in Figure 5.14 is highlighting the acceptor and donor role played by the pyrene residue and the GNC unit, respectively. An ultrafast nature is denoted, in Figure 5.14a during the initial photoexcitation (the duration of the laser pulse employed is 100 fs) at 45 fs a switching of the donor-acceptor character of the pyrene

residue is achieved and a clear charge separation is obtained. At around 500 fs the charge separation is stabilized. In the case of alkyl phosphine ligands, discussed in Figure 5.14b and 5.14c very similar to the previous discussion, an ultrafast photoinduced charge transfer mechanism is observed. With the pyrene residue playing as acceptor. In Figure 5.14b for the case of methyl units, the system presents a decreasing tendency of the charge separation during the 700 fs investigated in the Ehrenfest dynamics. In the case of ethyl ligands, after the first 250 fs of the dynamics is observed an stationary state. More than a difference in the values of charge separation, the relaxation after the first stage of the dynamics is different.

Next step in the analysis is to unraveling the contribution of the GNC core, and the ligands on the charge separation after photoexcitation. The phenyl ligands study case presented in Figure 5.15a clearly denotes an acceptor behaviour with the GNC core as donor

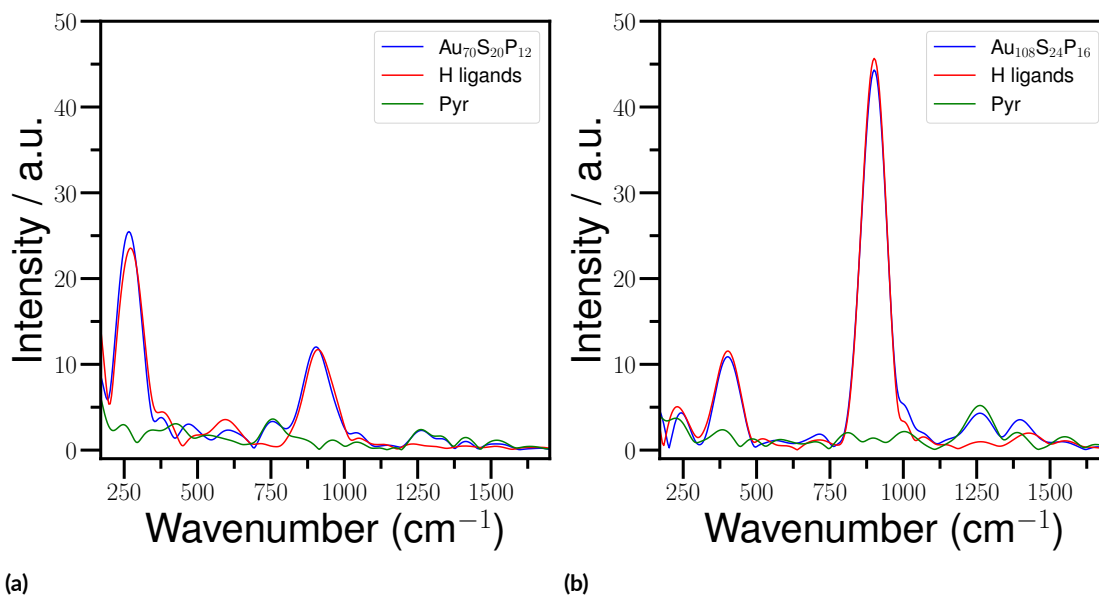


Figure 5.12: Fourier intensity spectra of the charge transfer dynamics obtained respectively for: (a) Au₇₀S₂₀(PH₃)₁₁PH₂Pyr and (b) Au₁₀₈S₂₄(PH₃)₁₅PH₂Pyr.

after the first 45 fs of the Ehrenfest dynamics. This behaviour is directly linked to the switching of the donor-acceptor character explained above. Compared to the results presented in Figure 5.15a for the phenyl ligands, the methyl ligands displayed in Figure 5.15b after 60 fs

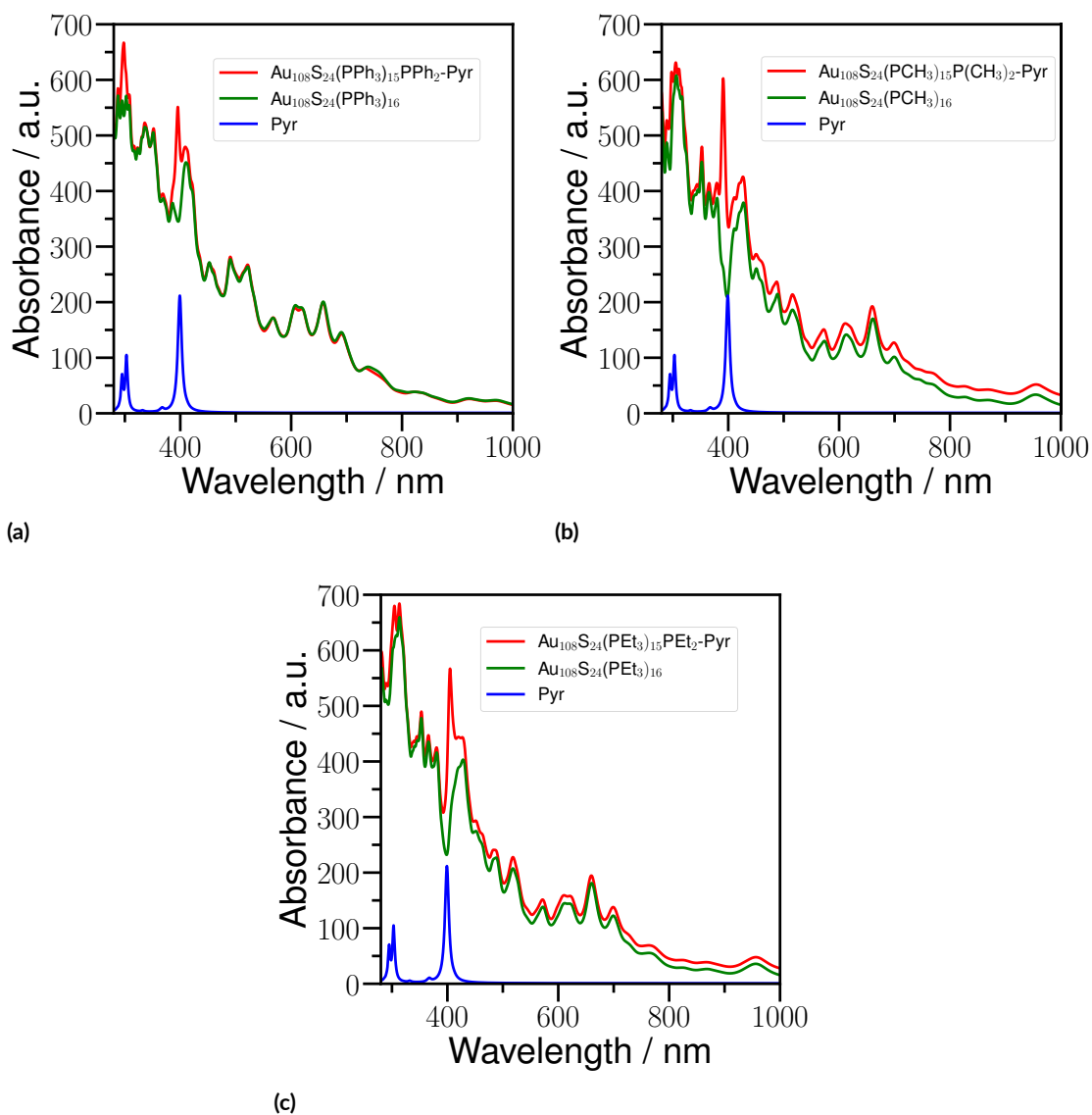


Figure 5.13: Absorption spectra obtained respectively, using RT-TDDFTB approach for the systems: (a) Au₁₀₈S₂₄(PPh₃)₁₅PPh₂Pyr, (b) Au₁₀₈S₂₄(PCH₃)₁₅P(CH₃)₂Pyr, and (c) Au₁₀₈S₂₄(P(C₂H₅)₃)₁₅P(C₂H₅)₂Pyr

a main donor character. The charge relaxation is describing fluctuations after 140 fs for the GNC core and methyl ligands. In the case of ethyl ligands presented in Figure 5.14c with a main donor character of the ethyl ligands, and the GNC core acting as acceptor is delimit-

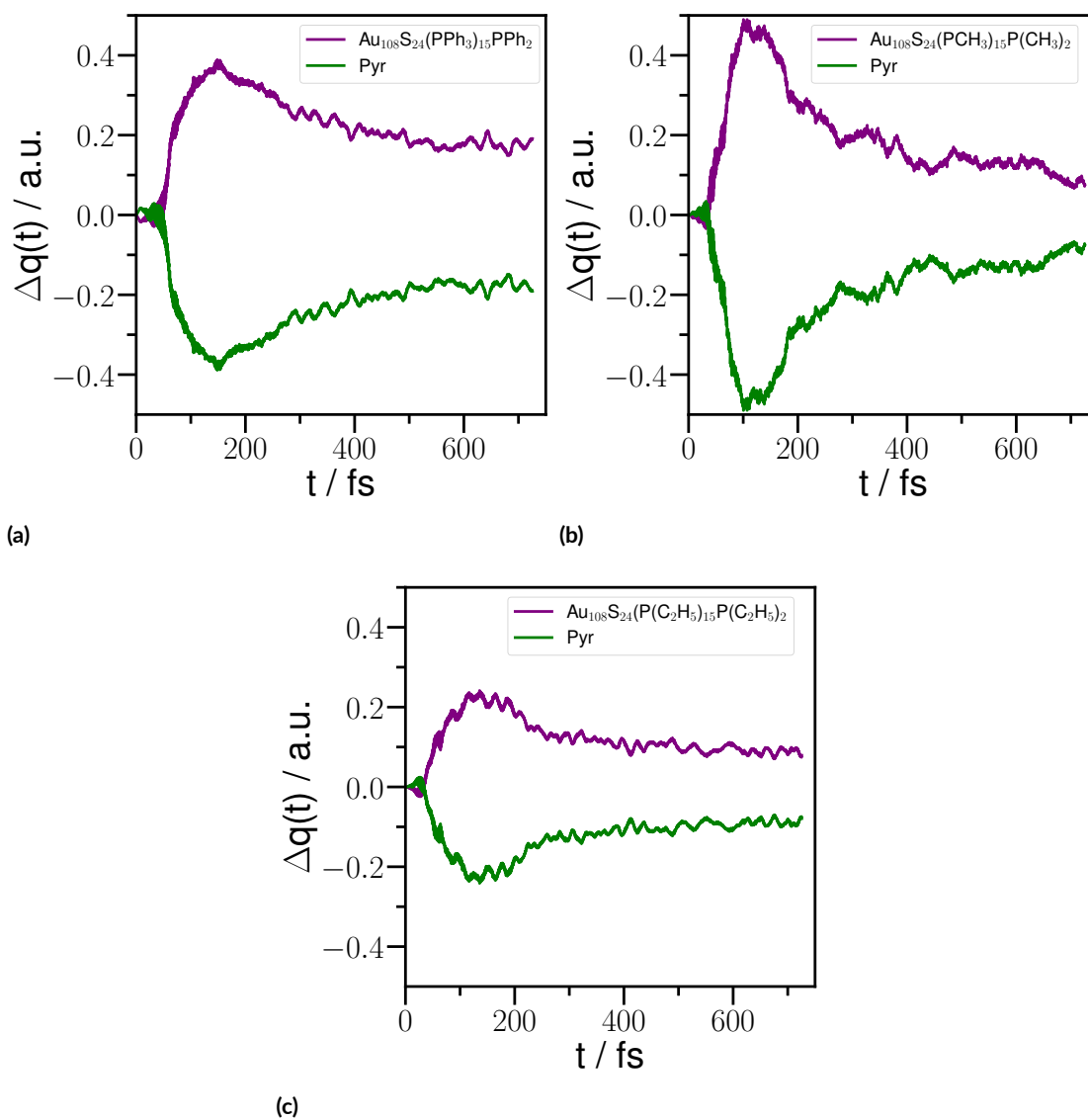


Figure 5.14: Changes in the Mulliken charges with respect to their ground-state values as a function of time: (a) $\text{Au}_{108}\text{S}_{24}(\text{PPh}_3)_{15}\text{PPh}_2$ Pyr, (d) $\text{Au}_{108}\text{S}_{24}(\text{PCH}_3)_{15}\text{PCH}_2$ Pyr, and (g) $\text{Au}_{108}\text{S}_{24}(\text{PC}_2\text{H}_5)_{15}\text{P}(\text{C}_2\text{H}_5)_2$ Pyr.

ited. From the behaviour discussed above, it is possible to underline the conclusion that the donor-acceptor features of the $\text{Au}_{108}\text{S}_{24}(\text{PPh}_3)_{15}\text{PPh}_2\text{Pyr}$ are crucial on a better charge separation compared to the alkyl ligands protected systems. The role played by the phenyl ligands as acceptor of charge and the superlative donor behaviour of the GNC core are crucial for the stabilization and better performance of the photoinduced charge-transfer displayed.

Emulating the previous discussion, a Fourier transform analysis of the dynamics have been performed to understand the nature of the oscillations in the charge separation presented during the dynamics. The full analysis is displayed in Figure 5.16. A detailed analysis of the vibrational modes presented for the $\text{Au}_{108}\text{S}_{24}(\text{PPh}_3)_{15}\text{PPh}_2\text{Pyr}$ system in Figure 5.16a is summarized as following: S-Au-S-Au-S symmetrical stretching and Au-S stretching are corresponding to the signal around 250 cm^{-1} , with S-Au-S stretching mode peaks related to the peak observed around 500 cm^{-1} . The =C-H bending, P-S stretching, and C-P stretching modes are at the region of the 700 cm^{-1} . The signals appearing in the region of the $1000\text{--}1300\text{ cm}^{-1}$ are the P-Aryl stretching and C-C stretching modes. The C=C stretching mode is observed around 1600 cm^{-1} .^{94,104,105,88} The discussed vibrational modes are in accordance to the reported Infrared (IR) spectra of $\text{Au}_{108}\text{S}_{24}(\text{PPh}_3)_{16}$ ⁹⁴ using DFTB approach and compared to experimental IR data. The presence of the vibronic couplings involved for this case is a signature of the stability and the performance on the charge separation predicted.

The analysis displayed in Figure 5.16b denotes a high peak at 1370 cm^{-1} corresponding to the C-H bending vibrations. The relaxation observed on the charge separation is linked to the major contribution of this signal. The presence of methyl protected ligands is not relevant for a more efficient photoinduced charge separation. The rest of the vibrational modes displayed are quite similar to the analysis before in the region under 500 cm^{-1} , with -Au-S-

Au-S symmetrical stretching, and Au-S stretching at around 250 cm^{-1} and S-Au-S stretching mode related to the signal near to 500 cm^{-1} .^{94,104,105,88}

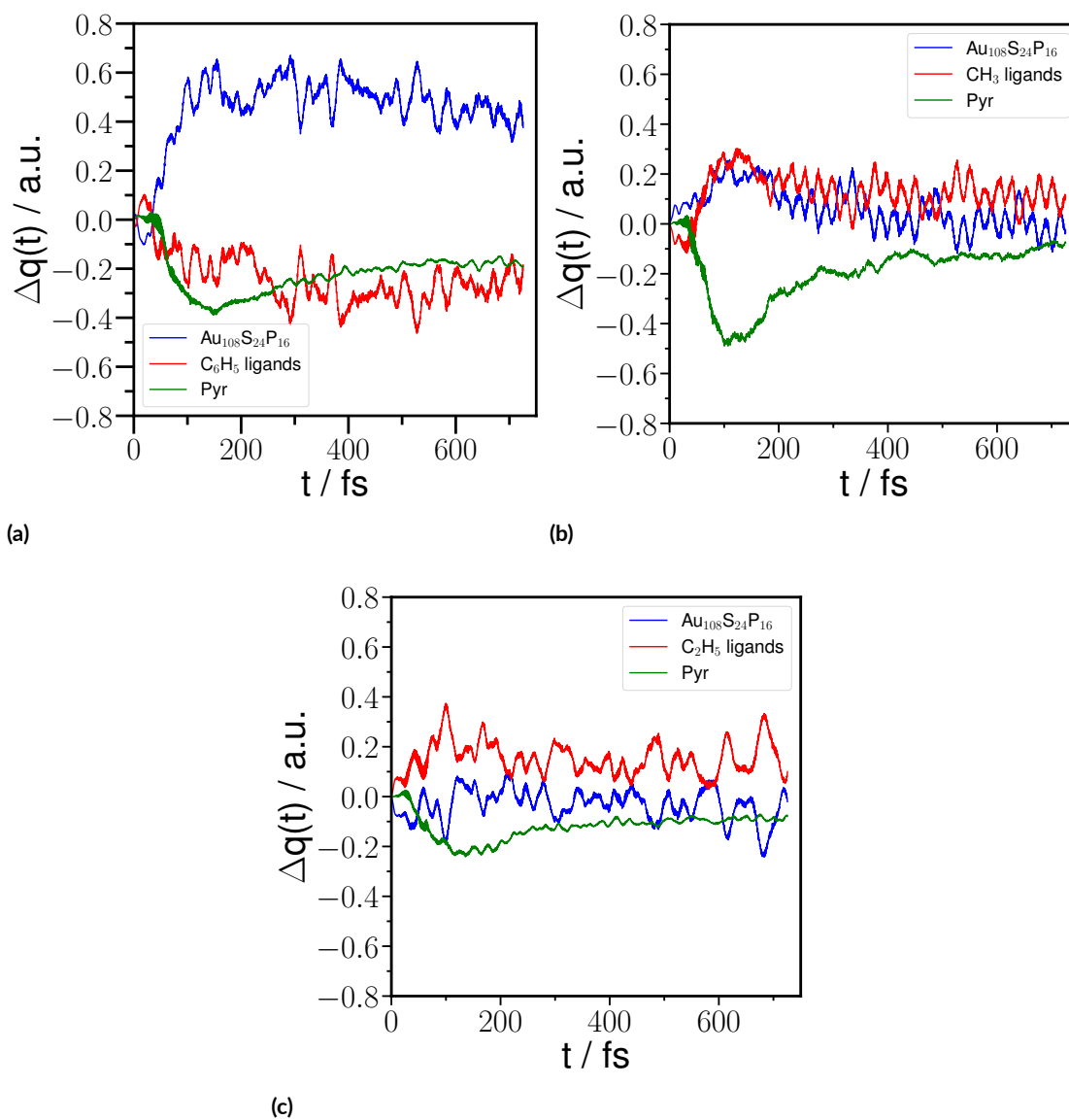
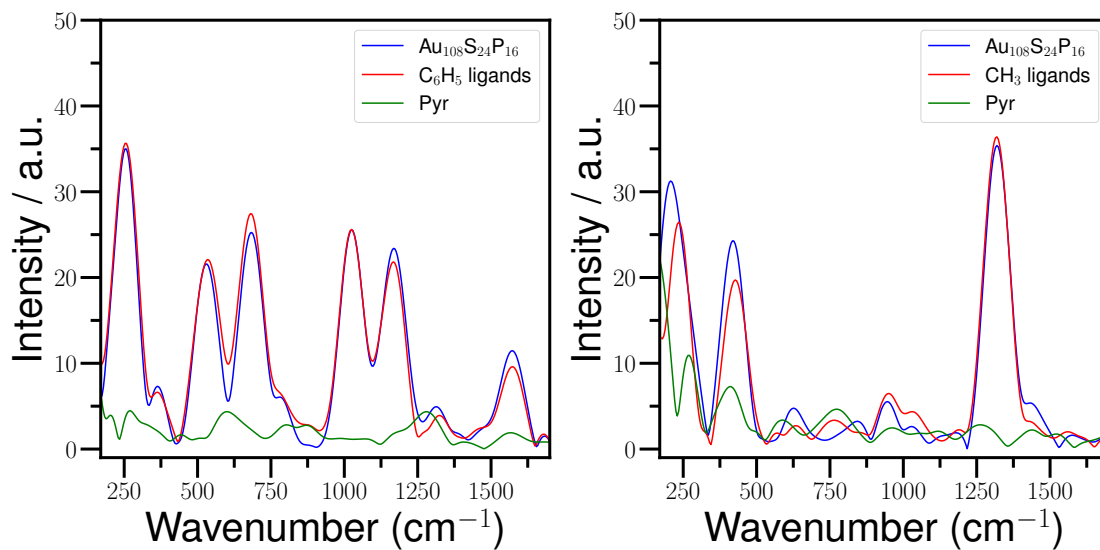
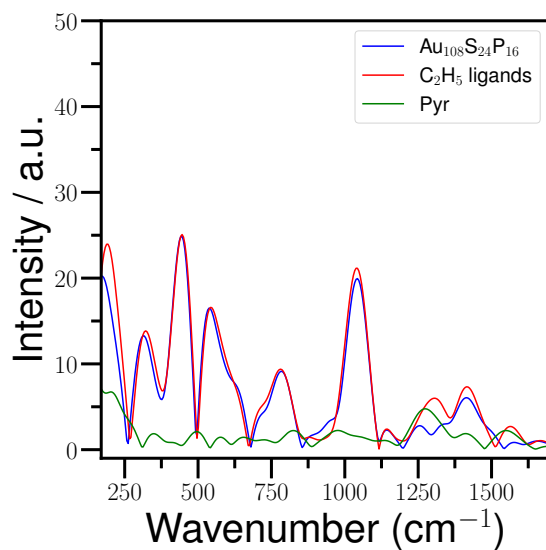


Figure 5.15: Individual contributions corresponding to the cases:
 (a) $\text{Au}_{108}\text{S}_{24}(\text{PPh}_3)_{15}\text{PPh}_2\text{Pyr}$, (b) $\text{Au}_{108}\text{S}_{24}(\text{PCH}_3)_{15}\text{PCH}_2\text{Pyr}$, and (c) $\text{Au}_{108}\text{S}_{24}(\text{PC}_2\text{H}_5)_{15}\text{P}(\text{C}_2\text{H}_5)_2\text{Pyr}$



(a)

(b)



(c)

Figure 5.16: Fourier intensity spectra of the charge transfer dynamics obtained respectively for: (a) Au₁₀₈S₂₄(PPh₃)₁₅PPh₂Pyr, (b) Au₁₀₈S₂₄(PCH₃)₁₅PCH₂Pyr, and (c) Au₁₀₈S₂₄(PC₂H₅)₁₅P(C₂H₅)₂Pyr

The ethyl protected ligands have a high contribution of the C-C stretching mode. The Figure 5.16c illustrates the presence of C-C stretching mode and C-H bending vibrations in the region of 1250-1400 cm^{-1} .^{104,105,88} The contribution of the peak corresponding to C-H bending vibrational mode is decreased. Peaks corresponding to P-C stretching mode at 750 cm^{-1} , P-CH₂-CH₃ band at 1100 cm^{-1} are displayed. Also, the S-Au-S-Au-S symmetrical stretching, Au-S stretching, and S-Au-S stretching mode^{94,104,105,88} are presented.

The nuclear motion is playing a key role on the mechanism involved in stabilize the photoinduced charge separation. The systems under study here are sensitive to the nature of the most predominant vibrational modes involved. The contribution of P-Aryl, P-C, C-C stretching modes is highlighted as positive for the charge relation during the dynamics. With the P-H and C-H bending modes being a negative point for the dynamics relaxation. The effects on the performance described are supporting the idea that the vibronic coupling and the protecting ligands should be one of the principles of designing new complexes based on GNC with ternary phosphine as protecting ligands with interest in photonics. The π -acceptor capacity expressed by the Tolman electronic parameter does not rule the behaviour on the performance for the photoinduced charge separation. For instance, the Au₁₀₈S₂₄(PPh₃)₁₅PPh₂Pyr system exhibited the higher performance on charge separation. With the limited predictive power of the Tolman electronic parameter shown here, the next discussion is addressed to explore insights on the steric effects by the consideration of the Tolman cone angle.

5.2.1 THE PHOTOINDUCED CT ABILITY WITH RESPECT TO THE TOLMAN CONE ANGLE

The Tolman cone angle¹⁰⁶ for the ligands under consideration present the following values illustrated in Table 5.1 (the values were taken from reference 106).

Table 5.1: Tolman cone angles for the ligands under study

Ligands	angle (degrees)
PH ₃	87
P(CH ₃) ₃	118
P(CH ₂ CH ₃) ₃	132
PPh ₃	145

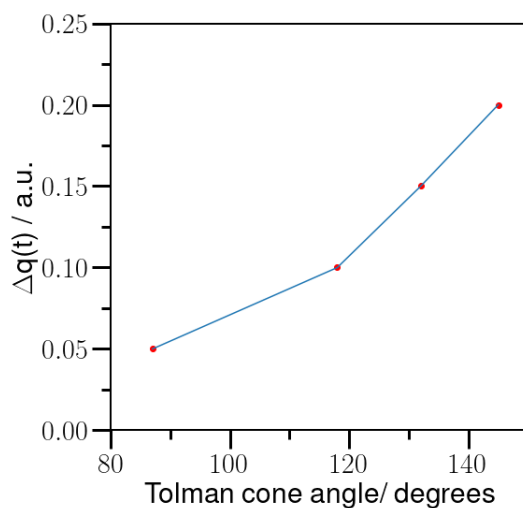


Figure 5.17: Main value of the changes in the Mulliken charges with respect to their ground-state values as a function of time for the stable charge-transfer state versus Tolman cone angle.

In Figure 5.17 is analyzed the tendency of the photoinduced charge transfer ability with the increase of the Tolman cone angle. A mean value of the changes in the Mulliken charges

with respect to their ground-state values as a function of time for the stable charge-transfer state is considered in y axis. (The presence of nuclear motion in the dynamics makes extremely complicated to select an specific value.) For the x axis, the data presented in Table 5.1 is considered. With the increase of the Tolman cone angle is observed an increase on the photo-induced CT ability. (for the cases under study) In conclusion, the steric effects are more significative than the π -acceptor capacity of the phosphine ligands considered.

For the first time, theoretical calculations predicted the ultrafast nature and irreversible charge separation of pyrene labeling novel metalloid GNCs. The insights provided clarify the advantage of the pyrene functionalization, with the $\text{Au}_{108}\text{S}_{24}(\text{PPh}_3)_{15}\text{PPh}_2\text{Pyr}$ system exhibited the superlative performance. A three-step mechanism is proposed, with an initial step corresponding to photoexcitation, followed by a donor behaviour of the pyrene derivate unit in the first 45 fs, finally, a clear charge separation dominated by the acceptor character of the pyrene derivative residue is observed. One important conclusion is the fact that the GNC size increasing does not improve the charge separation performance. The middle-sized GNC is an optimal size based in a comparison between the $\text{Au}_{70}\text{S}_{20}\text{P}_{16}$ core and $\text{Au}_{108}\text{S}_{24}\text{P}_{16}$ core. The steric effects related to the Tolman cone angle are of a paramount importance in the designing of functionalized devices for optoelectronics. The results obtained about photoinduced charge separation when compared to the π -acceptor capacity related of Tolman electronic parameter for the systems under study does not follow the initial order reported in the original work by Tolman in the 70's of the last century. In conclusion, the steric effects predominate over the π -acceptor capacity, in the criteria of selecting the best performance on the photoinduced charge separation.

Nature isn't classical, dammit, and if you want to make a simulation of nature, you'd better make it quantum mechanical, and by golly it's a wonderful problem, because it doesn't look so easy.

Richard P. Feynman

6

Theory meets experiments for laser-induced processes on TiO₂

BY SIMULATING EXCITED-STATE DYNAMICS, and modeling relevant spectra, computer simulations can help to translate experimental observations into atomic-level mechanistic pictures providing detailed insight into the primary steps of photo-chemical reactions. TiO₂

catalysts are cheap and biological inert with photoactive properties, being attractive for many applications. The interaction of organic molecules with TiO_2 surfaces have been studied with interest during the last decades.^{9,107,108,109} In this chapter, the results presented in section 6.1 follow reference 98 and the section 6.2 and 6.3 are part of publications in preparation in collaboration with experimental colleagues.

6.1 CO PHOTOOXIDATION ON TiO_2 ANATASE 101 SURFACE

The photo-catalytic activity of Bulk TiO_2 anatase and rutile for CO photooxidation to CO_2 has been studied before.¹¹⁰ The mentioned study reveals high catalytic activity for the CO photooxidation on TiO_2 anatase 101 in comparison with others TiO_2 polymorphs surfaces.¹¹⁰ The experimental results from Infrared Absorption Spectroscopy demonstrated that following an exposure of TiO_2 anatase 101 to CO at 100 K, an IR peak is observed. This signal is assigned to CO adsorption on TiO_2 with Carbon atom pointing towards the Ti_{5c} site.¹¹⁰ This experimental result is confirmed and reported in several theoretical studies.^{111,112,113} Mingchun et al.¹¹⁰ also reported the photoinduced oxidation of CO only when the TiO_2 anatase 101 surface is exposed to oxygen molecules and UV photons with energy of 3.4 eV. In this experimental work is discussed about the different orientations for the adsorbed CO and CO_2 and confirm the necessary presence of O_2 for the photoreaction to take place.¹¹⁰ IR data reveals that CO photo-oxidation is observed without the presence of any intermediates. This conclusion is very important because established the role of the photophysical processes in the CO photooxidation on TiO_2 anatase 101 surface.¹¹⁰

The adsorption and CO oxidation on TiO_2 anatase 101 has been investigated previously,

by using DFT calculations for the elucidation of the photoreaction processes.¹¹² The main focus was the oxidation process on a positive charged TiO₂ anatase 101 surface assuming the presence of a hole for the conversion of CO to CO₂.¹¹² Wanbayor et al.¹¹² concluded that further studies are required to clarify the details of the photo-catalytic oxidation of CO on the TiO₂ anatase 101 surface. To the best of our knowledge, there is no other theoretical work published regarding this topic. The insights into the CO photooxidation have been limited by the understanding of the charge carriers influence in this photocatalytic reaction. The number of publications is very scarce despite the interest in the chemistry of oxide surfaces and in particular of TiO₂ photocatalytic activity.

On the other hand, it is well-known in the literature that O₂ molecules present a triplet spin configuration and it is inert in the interaction with molecules with singlet spin configuration like the case of the CO molecule, no chemical reaction is possible. For the activation of O₂ it is necessary the triplet-singlet state transition or the O₂ electron acceptance. The last case is the most probable scenario. Setvin et al.¹¹⁴ reported two different charge states of O₂ were distinguished in an experimental work using AFM techniques for a single-crystalline mineral TiO₂ anatase 101 sample. The researchers in this publication confirm the presence of neutral O₂ molecules and O₂ molecules that accepted and electron from the surface.¹¹⁴

This results motivate theoretical studies about O₂ charge transfer on TiO₂ anatase 101 surface which would provide relevant information about this key process for photocatalysis, and in addition valuable information for the CO photooxidation. The CO oxidation is of huge environmental importance and is attracting the attention of research groups and industry. Recently, our experimental collaborators from the Nano Group at DESY, Hamburg, have reported about the ultrafast nature of the CO photooxidation on TiO₂ anatase 101. In

their study an optical laser of around 800 nm was used in an ultra-fast optical pump-soft X-ray probe experiments at FLASH in DESY. In this experiments the CO photooxidation has been observed at two different times with peaks of CO₂ formation at 2.1 ps and 7.3 ps. The understanding of the activation mechanisms for this laser-induced reaction is very challenging.¹¹⁵

The DFT periodic calculations were performed using the VASP code^{116,117,118,119} Calculations were carried out at the PBE level of theory¹²⁰ with an energy cutoff of 400 eV and the projected augmented-wave method.^{121,122} In order to model the anatase (101) surface an slab containing 36 Ti atoms and 72 O atoms in a supercell with 2x3 surface unit cells. The Brillouin zone was sampled with a 2x2x1 Monkhorst-Pack k-points grid. The triplet spin configuration of the O₂ specie is considered in the involved cases. In all cases, frequency calculations were performed to corroborate the minima reported. The van der Waals interactions were included by using dispersion corrections of DFT-D₃ method with Becke-Johnson damping.^{123,124} The DOS analysis was computed at the DFT level of theory with PBE functional¹²⁰, a (4x4x1) k-points grid and the semi-empirical nonlocal external potentials (NLEP).^{125,126,127}

The adsorption energy is calculated as :

$$E_{ads} = E_{complex} - E_{surf} - E_{mol}$$

where E_{surf} , E_{mol} and $E_{complex}$ are the corresponding total energies of the TiO₂ surface, the individual molecule(s) and the complex system formed by the physisorbed molecule(s) and the surface, respectively. By this definition, an exothermic process is denoted by a negative value

of the adsorption energy.

For the DOS analysis performed at the DFTB level of theory⁴⁶ a (4x4x1) k-points grid was used. The absorption spectra was obtained using linear response TD-DFTB approach (solving Casida equation) implemented in the DFTB+ code⁴⁶ and employing the *tiorg-0-1* set of parameters¹²⁸ modified. New repulsive potentials were created for Ti-O and Ti-C in the *tiorg-0-1* parameters set. In order to model the TiO₂ anatase 101 surface a Ti₂₄O₇₁H₄₆ cluster is used. In the construction of the cluster model, the cluster was saturated employing H atoms to passivate the peripheral O atoms and retain the neutrality. The cluster model was validated by periodic boundary condition calculations regarding electronic structure and geometries. The first 700 excitation energies of the TiO₂-O₂ system were calculated. With a covering of energetics of up to 3.7 eV. Only the excited states with a spin contamination of the expectation value of the spin square operator, $\langle S^2 \rangle$, lower than 0.5 were taken into account.

The results obtained using DFT calculations for the description of the electronic and structural properties on the adsorption of CO, O₂, and coadsorption of O₂ and CO on the TiO₂ anatase (101) surface are reported in Figure 6.1 and Table 6.1. The optimized geometries and energetics for CO and O₂ underlines the preference of both molecules to interact with the pentacoordinated Ti (Ti_{5c}) sites, in agreement with previous reports.^{110,129,130,131} The chemistry of CO is ruled by the intrinsic properties of the CO molecule with the C atom presenting a negative electronic partial charge based on the Lewis structure, explaining the C atom ending orientation in the interaction with Ti atoms.

The O₂ is adsorbed on Ti_{5c} active site of TiO₂ anatase 101 surface, with an adsorption

energy value of -0.15 eV and an interatomic distance of 2.76 Å. These findings are in agreement with previous results.[?] In the case of the coadsorption of CO and O₂ are considered two different configurations. The first case is the adsorption of CO and O₂ on two adjacent

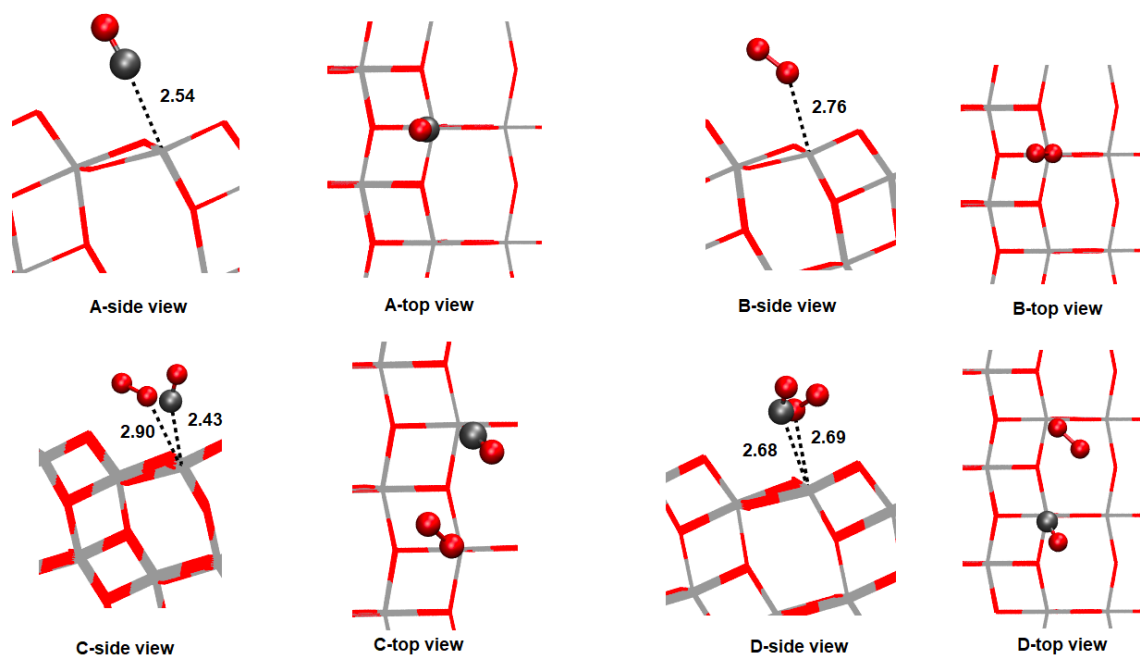


Figure 6.1: Optimized geometry obtained corresponding with: A)CO adsorption over TiO₂ anatase 101 surface; B)O₂ adsorption over TiO₂ anatase 101 surface ; C)coadsorption over a Ti5c binding site on TiO₂ anatase 101 surface; D) coadsorption over two adjacent Ti5c binding site on TiO₂ anatase 101 surface, respectively. Bond lengths are given in angstrom (Å).

Table 6.1: Energetic values for the adsorption energies in eV for the systems under study using $(2 \times 2 \times 1)$ k-points grid,PBE functional at DFT level of theory.

System	E_{ads} (eV)
CO adsorption	-0.27
O ₂ adsorption	-0.15
coadsorption-one-site	-0.48
coadsorption-two-sites	-0.37

Ti_{5c} active sites. The second case is the coadsorption of O and O₂ on the same Ti_{5c} active site. Interesting, the last case is the configuration more stable energetically by 112 meV. The interatomic distance of 2.43 Å between the C atom in an ending position and the Ti_{5c} active site is underlined. Being this value shorter than the result obtained for the CO adsorption case.

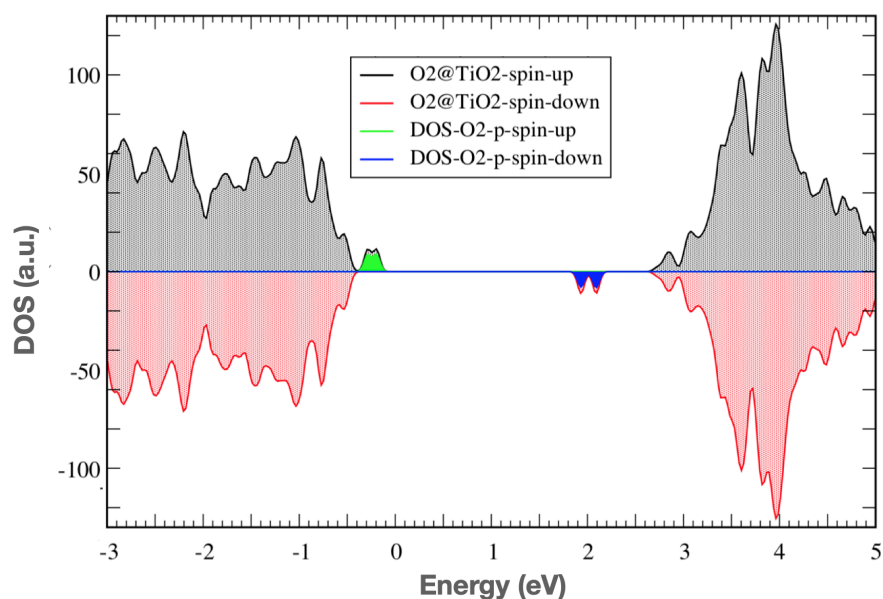


Figure 6.2: DOS for the O₂ adsorbed system using (PBE) functional at the DFT level of theory. The Fermi level was shifted to zero.

In Figure 6.2 is illustrated the DOS analysis corresponding to the O₂ adsorption on TiO₂ anatase 101 surface. The adsorption of O₂ molecule on the surface is linked to the break of the degeneracy of the π^* states, and the occupancy of two spin-up states and the unoccupancy of two spin-down states. The DFT calculations demonstrated the appearance of an intragap state corresponding to the antibonding π^* states of O₂ molecule. In Appendix C are displayed similar DOS and PDOS analysis obtained by DFTB calculations, reproducing

the DFT results discussed. The main features of this intragap state is the fact that a formation of a O_2 charge transfer (CT) complex is possible by using visible light or near infrared wavelength. At this point, the hypothesis about the presence of the intragap state related to the new presence of a peak in the absorption spectra is confirmed in Figure 6.3. The peak at approximately 1.6 eV is obtained with larger oscillator strength. Aligned to the experiments, the laser energy used is 1.6 eV and theoretically is described by our calculations. Usually, involving semiconductors is commonly accepted that it is necessary to employ UV light to create e/h pairs and these charge carriers are the responsible of the activation processes. The comparison in Figure 6.3 related to the new absorption peak at lower energies of the O_2 - TiO_2 charge-transfer complex is highlighting an alternative mechanism for the O_2 activation using visible light instead.

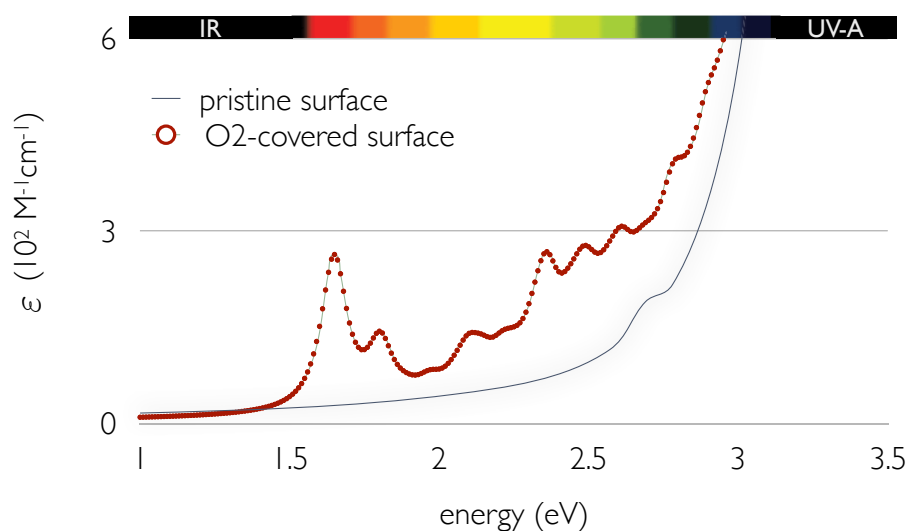


Figure 6.3: Absorption spectrum of the O_2 - TiO_2 charge-transfer complex and pristine TiO_2 . ϵ corresponds to the molar extinction coefficient as discussed in reference.

In Figure 6.4 is analyzed the nature of the charge transfer complex observed for the O_2 - TiO_2 system. The linear response TD-DFTB method is describing the excitation contributions

by the projection of the metal-to-ligand (ML), the ligand-to-metal (LM) charge transfer excitations and the transitions between the valence and conduction band. For the system in consideration, a weak absorption bands are observed in the visible region. The nature of the charge transfer excitations corresponds to transitions from the top TiO_2 valence band to the O_2 molecular states. The dominant contribution of the lower range of the spectrum is metal-to-ligand contribution, denoting the formation of O_2^- species and positive charged surface. And transitions from the highest occupied molecular orbitals to the conduction band are displayed in a minor level.

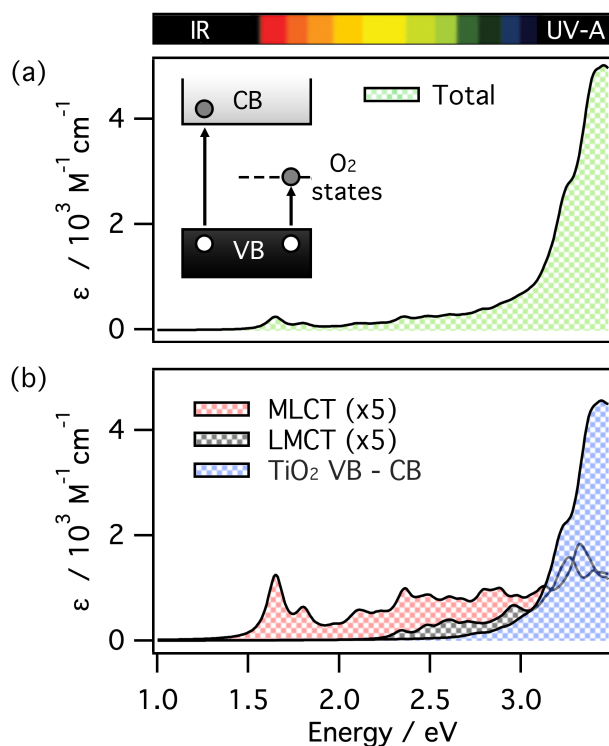


Figure 6.4: Absorption spectra of the $\text{O}_2\text{-TiO}_2$ CT complex. The total absorption spectrum (a) has been projected onto three separate components shown in (b) metal-to-ligand CT) transitions (red), ligand-to-metal CT transitions (black), and band-to-band excitations (blue).

For an efficient scheme for the O₂ activation, the recombination of the charge carriers is not desired. The electron trapping by the O₂ specie is favorable in the CO photooxidation mechanism. If compared to the band-to-band excitations, the small probability of the charge transfer event at the UV region is balanced with the effectiveness on the electron trapping corresponding to the charge transfer mechanism. Previously, an study about the degradation of NO on TiO₂ under visible and UV light illumination was exhibited , with the charge transfer process and the charge carriers generation are of similar intensity level.¹³²

In summary, the adsorption of O₂ on TiO₂ anatase 101 surface outlined a localized charge transfer state in the bandgap corresponding to the O₂ molecule. This charge transfer intragap state is directly associated to a new band at lower energies in the absorption spectra. This feature allow us to suggest the O₂ activation with light in the near IR region, the photoexcitation ruled by one photon with a charge transfer from the surface to the O₂ physisorbed molecule. The theoretical findings reported here are in accordance to the experimental observations and the previous work of M. Setvin et al.¹¹⁴ The formation of the charge transfer complex of the O₂ initiate the photooxidation of CO on TiO₂ anatase 101 surface after the absorption of one-photon with an energy below the band gap of the TiO₂ photocatalyst.

6.2 WATER-TiO₂ ANATASE 101 SURFACE

The water/anatase 101 adsorption has been reported before by several studies. One example is the DFT study of A. Vittadini et al.¹³³ describing the structure and energetics of the adsorption process. On the other hand, the study of several adsorption conformations and the

effect of the geometry in the photochemistry is incomplete. Our theoretical findings underline the importance of the adsorption configuration in the charge-transfer initial role in the water splitting reaction. The initial dynamics ruling this charge-transfer process is studied by using Ehrenfest dynamics simulations. The adsorption configuration display an effect on the photoinduced charge transfer processes. a net charge transfer from water molecules to the TiO_2 surface is observed right-away during the simulation. The Ehrenfest dynamics simulations start always from the electronic ground-state configuration of the system. It is added a perturbation to the Hamiltonian (in this case a laser pulse with a laser energy of 3.245 eV) in order to explicitly excite the system during the dynamic (imitating the experimental conditions. The simulations do not start our simulations from a certain excited state (in contrast to other methods) but it is created the photo-excitation in real time within the first 20 fs of the dynamics. Hence, in the method employed is possible not only to follow the charge transfer dynamics under the pulse but also the photo-excitation process at its beginning.

The theoretical results presented in this section provide new insights as follow: First, a dynamical picture in the understanding of the photocatalysis of water/ TiO_2 anatase 101 surface and the ultrafast charge transfer mechanism. Second, the impact of adsorption configurations in the photoexcited process for the water/ TiO_2 anatase 101 interface. And finally, a fully complement to the experimental observations. For the correct description of the electronic structure, adsorption processes over TiO_2 anatase 101 surface, and for the study of the evolution of the density matrix using real time propagation to compute absorption spectra and electronic dynamics calculations, the DFTB+ code⁴⁶ is employed. The present study is performed in periodic conditions with a 108 atoms and following lattice parameters: $a = 11.3313 \text{ \AA}$, $b = 10.1715 \text{ \AA}$ and $c = 30.0000 \text{ \AA}$ unit cell size for the TiO_2 anatase 101 surface. For the k-points sampling a (4x4x1) Monkhorst-Pack set is employed. The ma-

torg parameter set¹³⁴ and a hydrogen bonding damping (HBD) function equal to 4 is used increasing the accuracy of the description of Hydrogen bonds. For the modelling of dissociated adsorption a OH group is placed above a Ti_{5c} site and a proton H at a O_{2c} site.

The adsorption energies(E_{ads}) were calculated by:

$$E_{ads} = \frac{1}{n}(E_{complex} - E_{TiO_{2c}} - nE_{H_2O})$$

where:

$E_{complex}$, $E_{TiO_{2c}}$, E_{H_2O} , n are the total energy of the water- TiO_{2c} complex formed by water- TiO_{2c} anatase 101 surface, the TiO_{2c} anatase 101 surface, the water molecule and number of water molecules respectively. Within this definition for adsorption energy, a negative value indicates an exothermic process.

To obtain the absorption spectra by using the RT-TDDFTB approach, an initial perturbation to the initial ground-state density matrix is introduced. This perturbation has the shape of a Dirac delta pulse, and the density matrix evolves in time, and its evolution can be resolved by time integration of the Liouville-von Neumann equation of motion. An initial electric field of 0.001 V/Å value is used. In order to model the dynamics of an electromagnetic wave, a \sin^2 shaped pulse is employed describing the electron dynamics during the light absorption with an electric field of 0.1 V/Å and an energy laser of 382 nm (expressed in eV units equal to 3.245). The total duration of the pulse is 20 fs in all cases. For the nuclei evolution in the Ehrenfest dynamics based on the Verlet algorithm a Temperature of 90 K is used. This method employed had been used with success in previous studies.^{135,136}

For a more accurate understanding of the laser-induced properties of the H₂O adsorbed onto TiO₂ anatase 101 surface is necessary the study of several adsorption conformations and

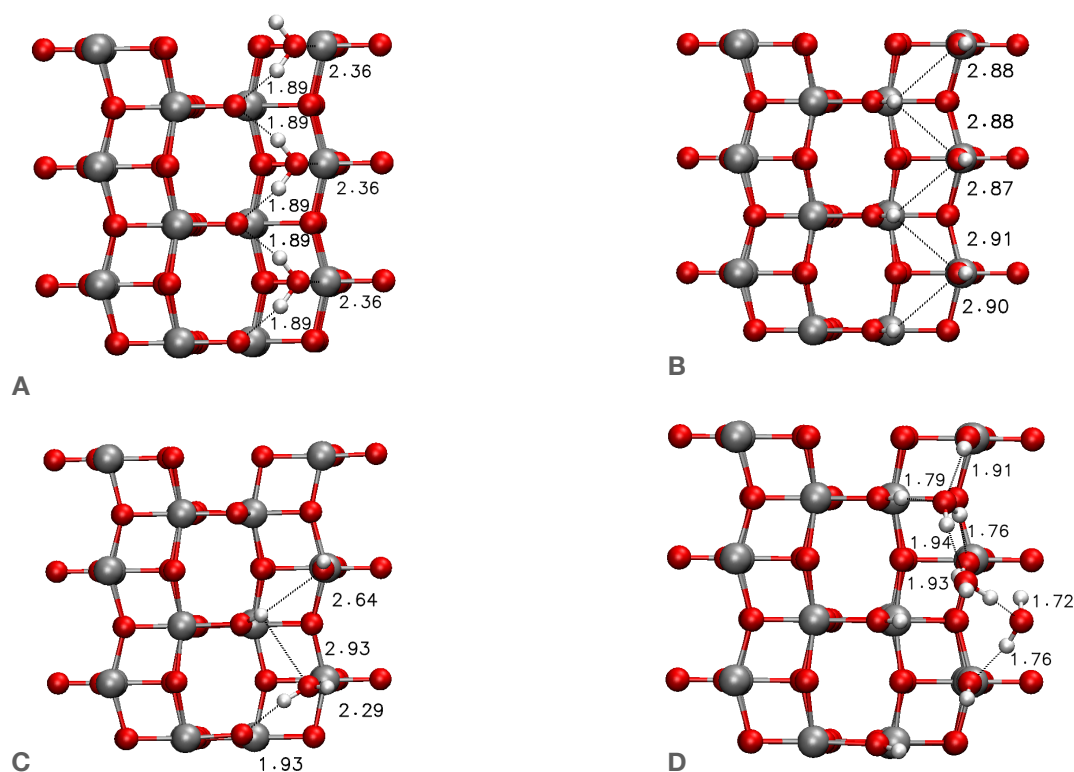


Figure 6.5: Molecular representation of a unit cell for the optimized geometry obtained for (A) molecular adsorption (undissociated) of H₂O molecules on TiO₂ anatase 101 surface (B) dissociative adsorption of H₂O molecules on TiO₂ anatase 101 surface (C) a mixture of molecular and dissociative adsorption of H₂O molecules on TiO₂ anatase 101 surface (D) molecular adsorption of H₂O molecules on the hydroxylated TiO₂ anatase 101 surface. Bond lengths are given in angstrom (Å).

System	E_{ads} (eV)
molecular adsorption	-0.85
dissociated adsorption	-0.57
both molecular and dissociated adsorption	-0.68
molecular adsorption on hydroxylated surface	-0.44

Table 6.2: Energetic values for the adsorption energies in eV per H₂O adsorbed molecule in the systems under study.

the effect of the geometry in the photochemistry of the systems studied here. The energetics and geometrical properties obtained for the systems analyzed here are comparable with the results obtained in previous studies.^{137,138,139} The energy results obtained at the DFTB level suggest the stability of the adsorption configuration for the systems studied here, confirming the possibility of OH groups presence on TiO₂ anatase 101 surface. The results obtained for the adsorption energy, $E_{ads} = -0.85$ eV, of the adsorbed water molecules over the most stable active site Ti_{5c} and the structural geometry (see Figure 6.5) were found to be in good agreement with theoretical and experimental data for the adsorption of water onto TiO₂ anatase 101 surface.^{137,140,141} The system with both molecular and dissociated adsorption, $E_{ads} = -0.68$ eV, is a more stable configuration in comparison with the dissociated adsorption system and the molecular adsorption over a hydroxylated surface, in agreement with previous reports.¹³⁸ For the hydroxylated systems a bond distance Ti_{5c}-OH is of 1.90 Å and there is a bond distance expansion for Ti_{5c}-O_{2c} in accordance with literature.¹³⁶

In the DOS analysis (see Figure 6.6), the TiO₂ anatase 101 surface the valence band is predominantly O 2p character with a minor presence of hybridized Ti 3d states. The conduction band is predominantly Ti 3d character with a minor presence of hybridized O 2p states. No significant changes appears when H₂O molecules are adsorbed molecularly (undissociated). The dissociatively adsorbed molecules present significant hybridization of the OH terminal group with the O 2p states of the surface at the top of the valence band.

At this point, the hypothesis to follow is that this last mechanism describes the charge transfer H₂O adsorbed onto TiO₂ anatase 101 surface by a two photons absorption with an energy around 3.2 eV. Based mainly in the fact of the experimental laser energy value used and the theoretical electronic structure description reported here. The initial dynamics rul-

ing this charge-transfer process is studied by Ehrenfest dynamics simulations using the energy value for a laser pulse of 382 nm (3.245 eV) with a total duration of the pulse of 20 fs. The adsorption configuration of H₂O affects the photo-induced processes on the TiO₂ anatase

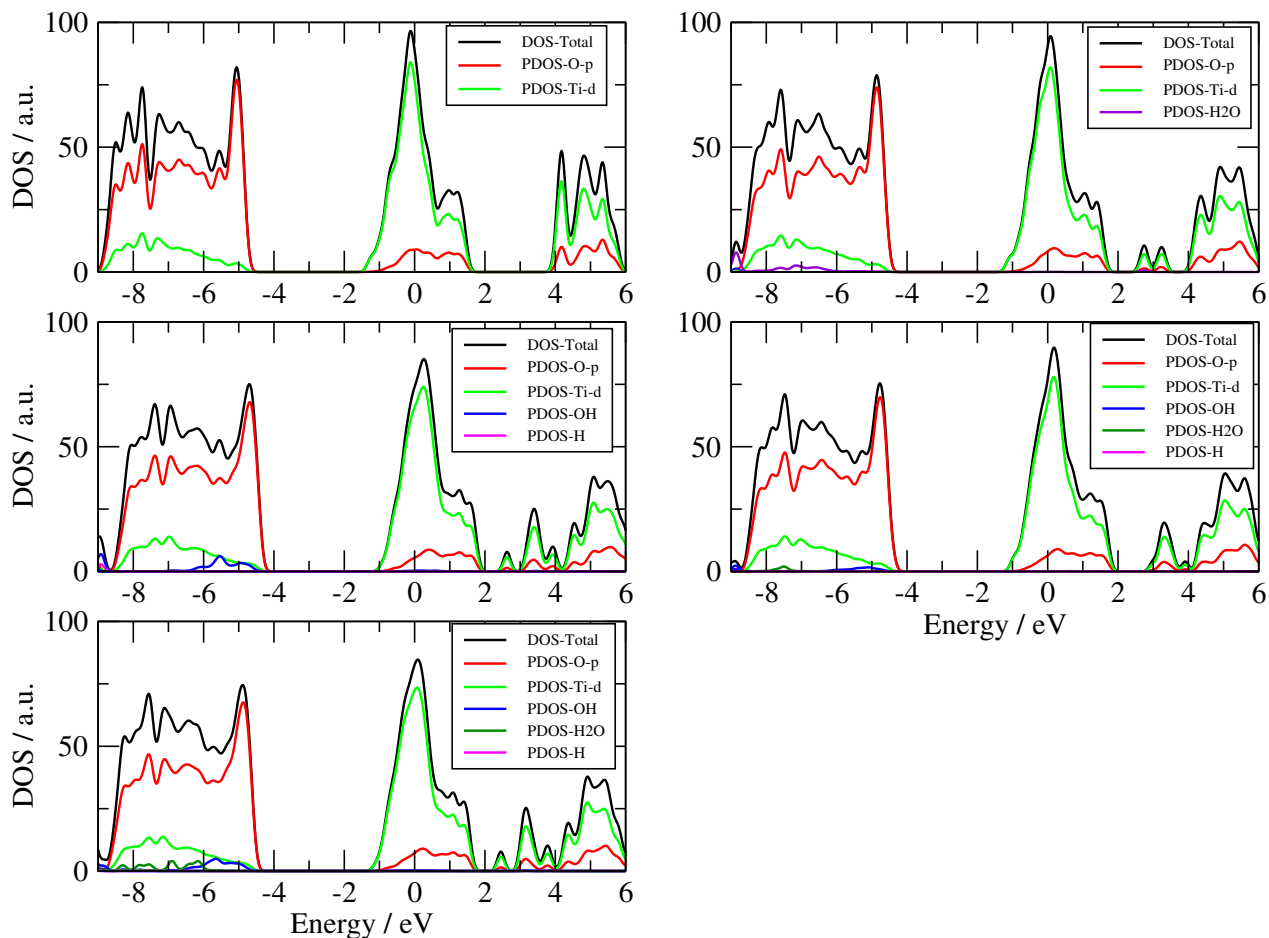


Figure 6.6: Density of States (DOS) and Partial Density of States (PDOS) for the systems under study. Top left represents the clean TiO₂ anatase 101 surface. Top right represents the undissociated water adsorption system. Middle left corresponds with dissociated water adsorption system. Middle right corresponds with undissociated water adsorbed over Ti_{5c} site and partial hydroxylated surface. Bottom left corresponds with undissociated water adsorbed over full hydroxylated surface.

101 surface as is shown in Figure 6.7.

In Figure 6.7, the black and red lines correspond with the instantaneous charge for the surface and the H₂O molecules respectively, with the green and blue lines representing an average value of the charge for the surface and the H₂O molecules respectively. The adsorption configuration display an effect on the laser-induced charge-transfer processes. For the systems with a complete dissociated adsorption and molecular adsorption on a complete hydroxylated surface, the charge transfer is displayed from the surface to the H₂O molecules. These configurations are the two less stable ones from the point of view of thermodynamics, reported in Table 6.2. The charge-transfer evolution in these two cases underline the presence of an excess of electrons in the surface favoring reduction processes. A similar conclusion was discussed by A. Selloni et al.¹⁴²

For the two most stable configurations (see Table 6.2), the molecular adsorption and a mixed molecular and dissociated adsorption, a net charge transfer from water molecules to the TiO₂ surface is observed right-away during the simulation. This qualitatively results are in agreement with the experimental charge-transfer observed by our collaborators at NanoLab in DESY, Hamburg. The mechanism proposed here is the generation of e⁻/h⁺ by the laser pulse. Next, the hybridized states belonging to the water molecules adsorbed and the O 2p of the TiO₂ anatase 101 surface contribute to the trapping of the h⁺ and the possible formation of hydroxyl radical (OH radical). Then the interaction of a close water molecule, acting as a donor, with this trapped holes denotes the charge transfer process. To illustrate this, in Figure 6.8 is presented the dynamics evolution for the undissociated water adsorbed over Ti_{5c} site and partial hydroxylated surface system. It is shown a new Hydrogen bonding formation between one of the Hydrogen in the molecular water physisorbed onto Ti_{5c} and a O_{2c}

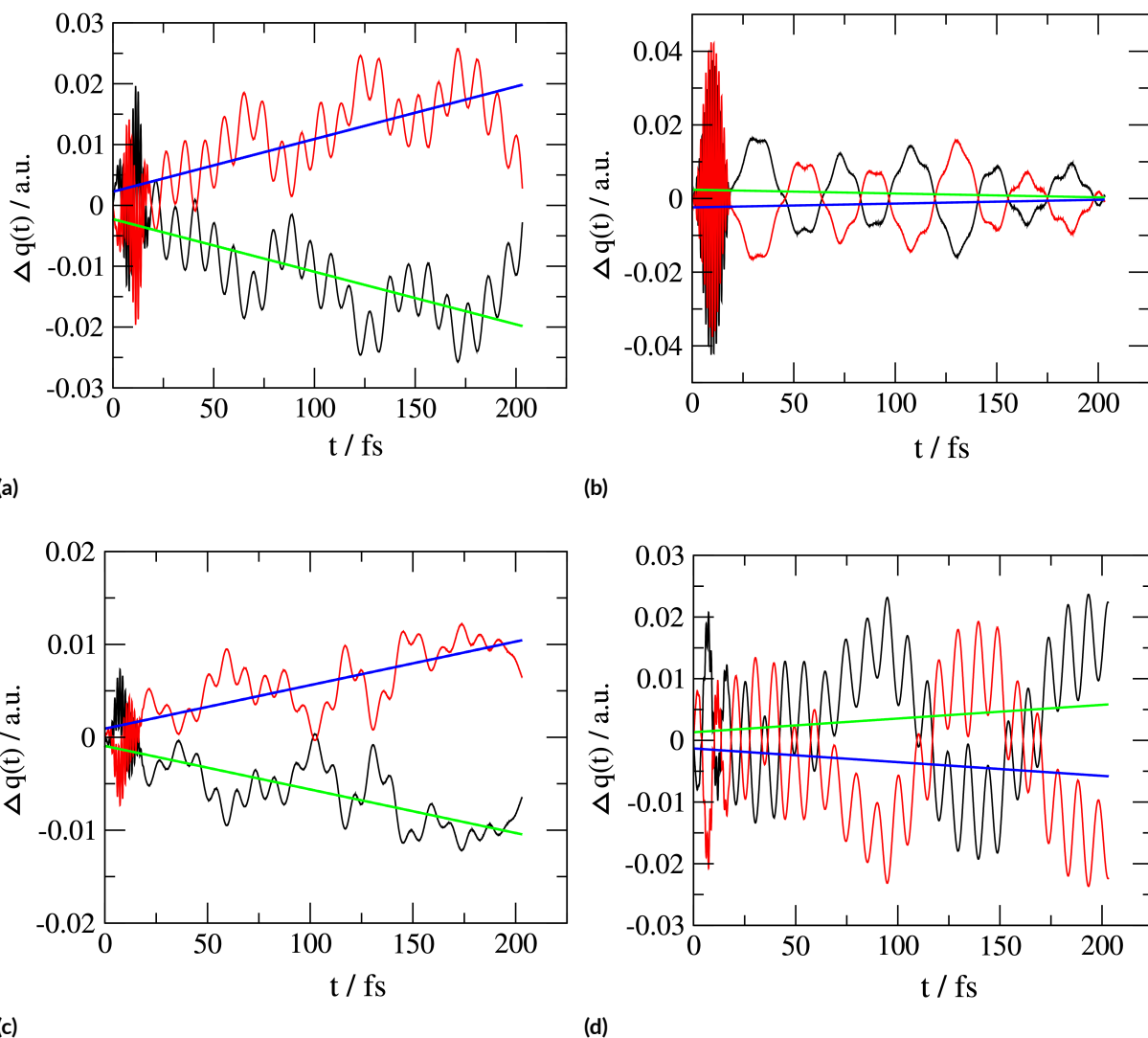


Figure 6.7: Changes in the Mulliken charges with respect to their ground-state values as a function of time for the systems under study. (a) undissociated water adsorption system. (b) dissociated water adsorption system. (c) undissociated water adsorbed over Ti_{5c} site and partial hydroxylated surface. (d) undissociated water adsorbed over full hydroxylated surface.

site. From an initial bond distance of 3.72 \AA to 1.98 \AA after 199.4 fs . The new Hydrogen bonding formation support the mechanism proposed above.

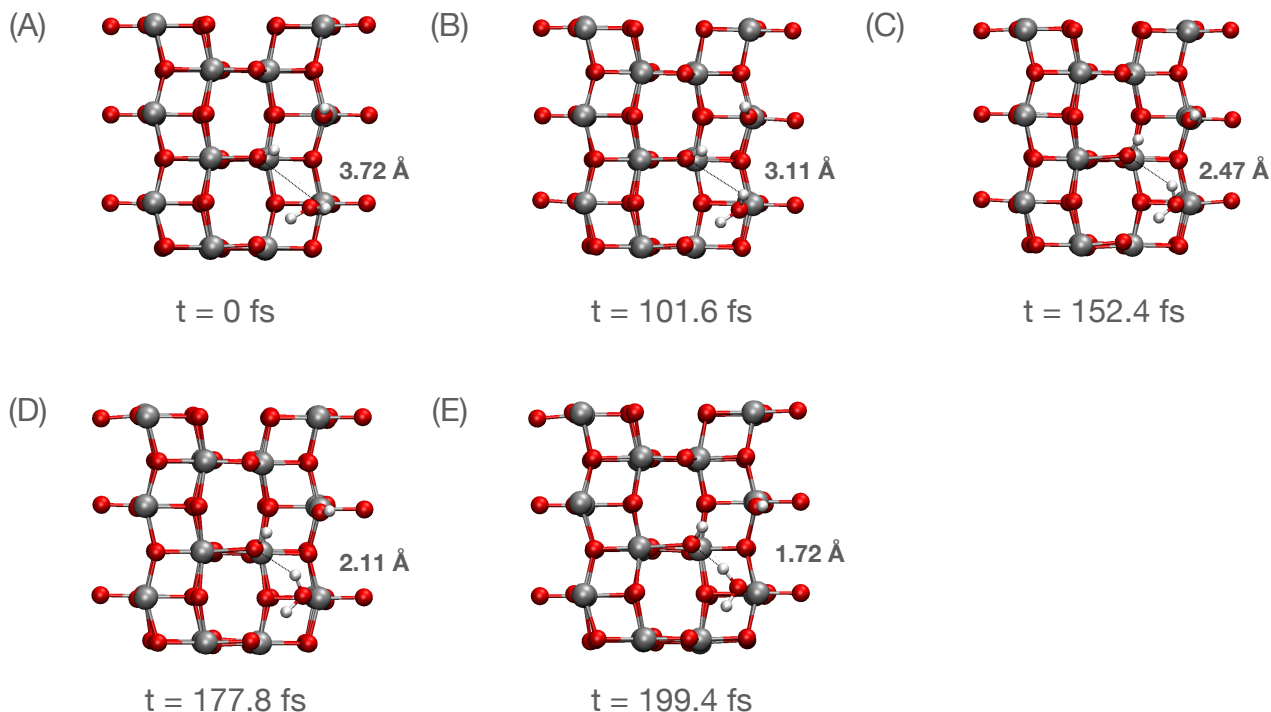


Figure 6.8: Dynamics evolution for the undissociated water adsorbed over Ti_{5c} site and a partially hydroxylated surface system. The Hydrogen bond formation: (A) time = 0 fs; (B) time = 101.6 fs; (C) time = 152.4 fs; (D) time = 177.8 fs; (E) time = 199.4 fs. The silver, red and white colors are used to represent Ti atoms, O atoms, and H atoms, respectively.

Previous research on the water oxidation on TiO_2 rutile 110 surface highlighting the role of excitations and OH species as important players was mentioned by Annapaola Migani et al.¹⁴³ The dynamics of the photogenerated hole at the Water/ TiO_2 rutile 110 interface was proposed by Kaxiras et al.¹⁶ Investigating the possibility of a hole-mediated splitting of molecular adsorbed water. The OH radicals are formed from the trapped holes. The study of Gyle Odling and Neil Robertson¹⁴⁴ reported that OH radicals are generated in the water/ TiO_2 anatase interface. Kenji Shirai et al¹⁴⁵ published a paper describing a hole trapping mechanism at the surface of TiO_2 anatase nanoparticles and the ability of water adsorbed enhance the hole trapping. In other paper, the hole-mediated water photooxidation

on TiO₂ 101 surfaces was presented by Cristiana Di Valentin.¹⁴⁶

These evidence support our hypothesis that different that the article of Cristiana Di Valentin¹⁴⁶ where the OH radicals are formed by the oxidation of water molecules and not resulting from hole trapping by OH surface, our paper determines a mechanism based on the key step of the hole trapping by OH groups adsorbed on Ti five-coordinate site and the hole transfer to molecular water adsorbed by the formation of an Hydrogen bond at around 200fs. The Ehrenfest dynamics performed allows to determine a net charge transfer from water molecules to the TiO₂ surface is observed right-away during the simulation. The mechanism proposed here is the generation of electron/hole pair by the laser pulse. Next, the hybridized states belonging the water molecules adsorbed and the O 2p of the TiO₂ anatase 101 contribute to the trapping of the h+ and the possible formation of hydroxyl radical (OH radical). Then the interaction of a close water molecule, acting as a donor, with this trapped holes denotes the charge-transfer process. The new Hydrogen bonding formation support the mechanism proposed above.

To obtain a clean water-surface is not easy from the experimental point of view. From our understanding the most real scenario is the case corresponding with undissociated water adsorbed over Ti_{5c} site and partial hydroxylated surface. This scenario display more hybridization favored by the presence of some OH groups in the surface in comparison with the undissociated adsorption (molecular adsorption) case. From our findings is possible to underline the importance of the adsorption configuration in the charge-transfer initial role in the water splitting reaction.

6.2.1 XPS BINDING ENERGIES CALCULATIONS FOR THE O_{1s} LEVEL CORE ON H₂O ADSORBED ON TiO₂ ANATASE 101 SURFACE

In X-ray photoelectron spectroscopy (XPS), electrons within a material absorb photons of a given energy. Based on the photoelectric effect, these electrons are emitted. By an analysis of the kinetic energy it is possible to calculate the binding energy. This approach is useful to get information on the identification of the chemical elements present in the material, the electronic states of the atoms, etc. A typical XPS spectrum is a plot of the detected number of photoelectrons versus the binding energy. Each element produces a set of characteristic peaks. At this point, the theoretical modeling of the XPS spectra by using DFT methods is the main interest in order to complete the analysis followed by the experimental observations. Also, this information provides another point in favour, as XPS data is a strong criteria to validate the most likely scenario selected for the proposed mechanism corresponding with undissociated water adsorbed over Ti_{5c} site and partial hydroxylated surface.

The VASP code^{116,117,118,119} was employed. Calculations were carried out at the Γ point and using PBE functional¹²⁰ with an energy cutoff of 450 eV and the projected augmented-wave method.^{121,122} To calculate the core level energies the Slater transition state approach was selected. The theoretical results (see Table 6.3) are similar to the findings in the experimental XPS. A shift of the O_{1s} core level is found for the corresponding peaks belonging to the O_{1s} core for the TiO₂, TiOH, H₂O (molecular adsorbed) respectively. The absolute Binding Energies present an inaccuracy up to a few eV, which is canceled when you refer to Binding Energies core level shifts.¹⁴⁷ Absolute energies are not meaningful, since VASP software usually reports valence energies only. Only relative shifts of the core electron binding energies are relevant.¹⁴⁸

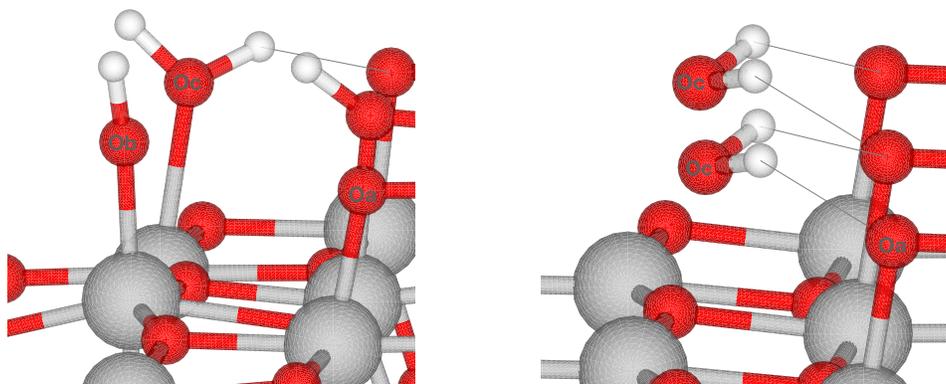


Figure 6.9: Configurations under study: **(left)** Mixed molecular and dissociative adsorption of H_2O molecules on TiO_2 anatase(101) surface **(right)** molecular adsorption (undissociated) of H_2 molecules on TiO_2 anatase 101 surface. Oa, Ob, Oc atom types are referred in Table 1 as the TiO_2 , Ti-OH, and molecular H_2O , respectively.

Table 6.3: Calculated and experimental (XPS) binding energies for the O1s core electron using VASP code and the KS core states half occupied energies. All values are expressed in eV.

	H_2O	Ti-OH	TiO_2
Mixed	545.0	542.1	541.4
Undissoc	544.3 544.4	-	541.4
Exp.	534.4	531.8	530.5

In the Mixed configuration scenario, before and after light exposure, different core level binding energies are obtained. A positive core level shift (increase of the binding energy) of the lattice oxide peak due to band bending and a negative core level peak (decrease of the binding energy) in the H_2O peak which can be related to hydrogen bond formation.

In the comparison between before and after light exposure, the geometry configuration

Table 6.4: Theoretical (XPS) binding energies for the O1s core electron for the **Mixed configuration** before and after light exposure using VASP code and the KS core states half occupied energies. All values are expressed in eV.

	H ₂ O	Ti-OH	TiO ₂
Before	545.0	542.1	541.4
After	544.1	542.0	541.5

reported in the Figure 6.9 (cases A and E respectively) mentioned above had been selected. As a reminder in Table 6.3 the results about the binding energies before light exposure has been reported.

6.3 X-RAY ABSORPTION SPECTROSCOPY OF TiO₂ ANATASE NANOPARTICLE

X-ray absorption spectroscopy measure the absorption of X-rays by atoms in a sample. Each element produces a characteristic absorption pattern. This spectra is a plot of absorption against energy. Applications include material science, and chemistry. The study of nanoparticles and structural changes during surface processes, and catalysis in general have been extensively described by using XAS techniques.

Recently, our experimental collaborators in Geneva, observed ultra fast decay of Ti L-edge bands in TiO₂ nanoparticles. Because in the Time-resolved NEXAFS experiment, it was initially observed an approx 6 eV broad at initial times and then after around 300 fs an approx 4 eV. The purpose of this work is to complement the experiments with theory focusing in the elucidation of the unclear behaviour presented. The DFT and DFTB methods in the past decades has provided explanation to many experiments, contributing with a deeper

progress on oxide-surface chemistry and unraveling of essential mechanisms in the nanoscale. This method employed had been used with success previously.¹¹⁵ With the theoretical modeling of the photoinduced electron/hole and the computation of the XAS spectra at different times is possible to complement the experimental work developed by our collaborators. These calculations will allow to a better understanding of the phenomena involved.

The $(\text{TiO}_2)_{153}$ nanoparticle was obtained using the *nanocut* tool.¹⁴⁹ The system was relaxed at the DFTB level of theory. All the calculations were performed using the DFTB+ code.⁴⁶ The set of DFTB parameters matorg have been used.¹³⁷ The quantum dynamics simulations based on the Ehrenfest approach in the RT-TDDFTB framework start from an electronic ground-state configuration, following the entire photodynamics. In this semi-classical method, the nuclei are driven by the instantaneous expectation value of the force at each time for the moving electron density. A perturbation to the Hamiltonian is added in the form of a laser pulse for the corresponding excitation, imitating pump-probe experiments. An extensive discussion can be founded in previously published papers.^{72,73} In the computation of the absorption spectra, an electric field intensity of 0.001 V/Å is employed with the propagation of 82684 steps using a time step of 0.0024 fs, in the linear response regime. For the Ehrenfest dynamics, an electromagnetic wave, a \sin^2 shaped pulse is employed describing the electron dynamics during the light absorption with an electric field of 0.1 V/Å and an energy laser of 266 nm. The total duration of the pulse is 40 fs in all cases. For the nuclei evolution in the Ehrenfest dynamics based on the Verlet algorithm, a Temperature of 298 K is used.

Figure 6.10b shows the calculated density of states (DOS) and partial density of states (PDOS) for system. The HOMO-LUMO gap (ΔHLG) obtained is 2.74 eV, aligned with the

validated result obtained previously.^{150,151} The Ti d orbitals and O p orbitals contributions to the bonding is clearly denoted. While the character of the unoccupied states is mainly of a Titanium d orbital nature. The frontier orbitals HOMO and LUMO are displayed in Figure 6.11a and 6.11b, respectively. The HOMO orbital extends only to one triangle lateral surface of the bipyramid shape of the nanoparticle. The LUMO orbital is corresponding to the four lobes shape of 3d orbitals of Ti atom, being delocalized.

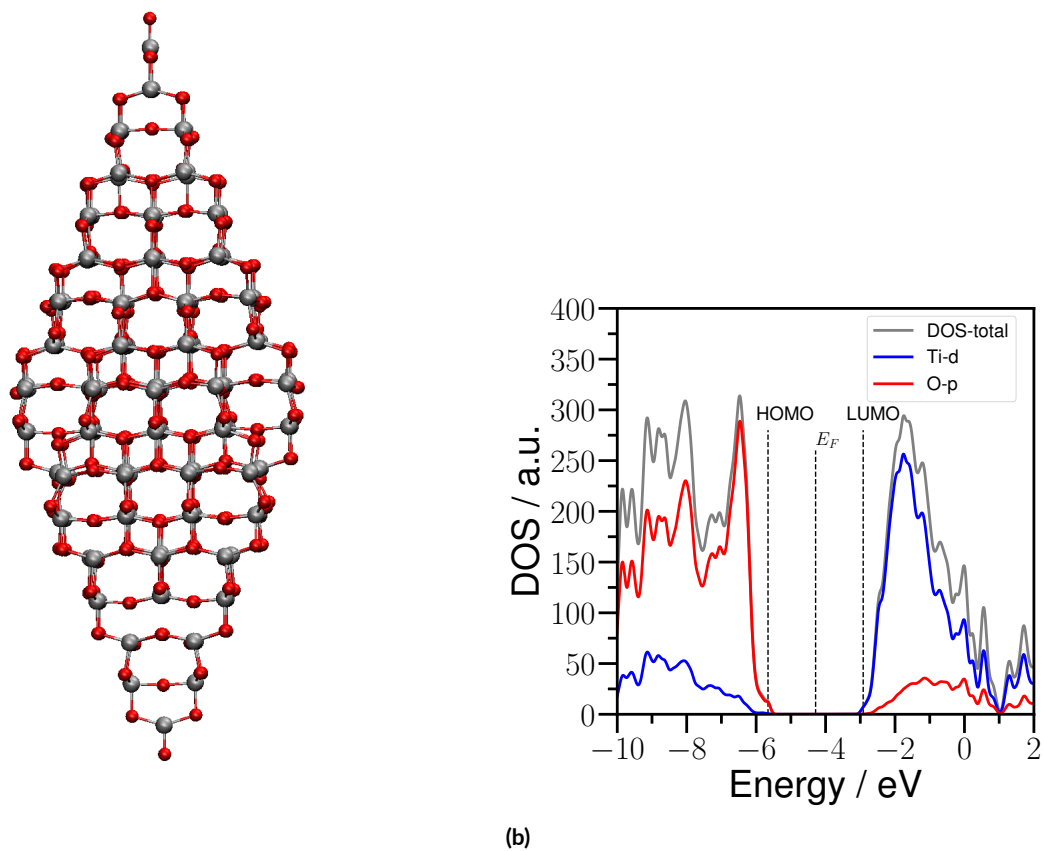


Figure 6.10: (a) $(\text{TiO}_2)_{153}$ nanoparticle system. (b) Density of States (DOS) and Partial Density of States (PDOS) analysis for the system under study.

Figure 6.12a displays a high absorption region below the 300 nm, in agreement with the 266 nm laser energy used in the experiments. The light-driven electron/hole formation process is discussed in Figure 6.12b with an ultrafast nature in accordance with experiments, being extremely efficient presenting no back charge transfer for the simulation time in consideration. The charge separation is based in the idea that with the electron/hole formation, the electron is related to Ti atoms centre and the holes to O atoms centre. (The charge separation is describing the ultrafast electron/hole formation (O atoms are donating charge (positive)

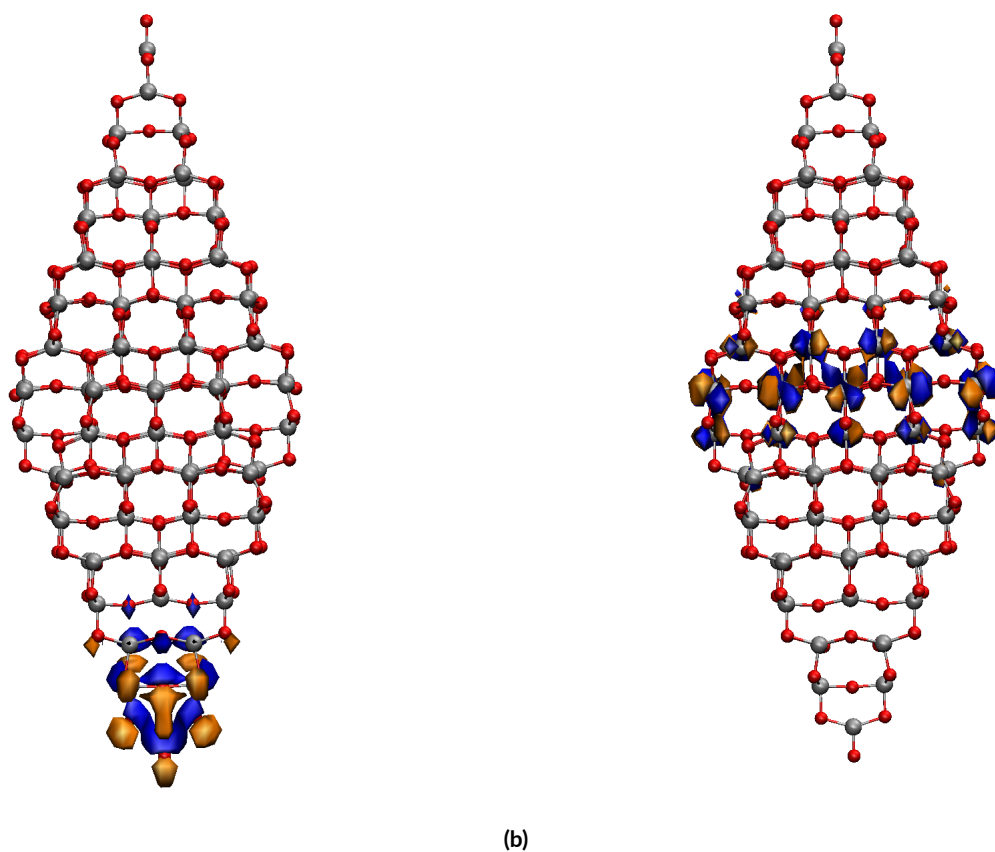


Figure 6.11: Frontier orbitals of the $\text{TiO}_2)_{153}$ nanoparticle: (a) HOMO (b) LUMO. Blue and orange colors correspond to the positive and negative isosurfaces. Isovalue $0.01 \text{ e}\cdot\text{au}^{-3}$

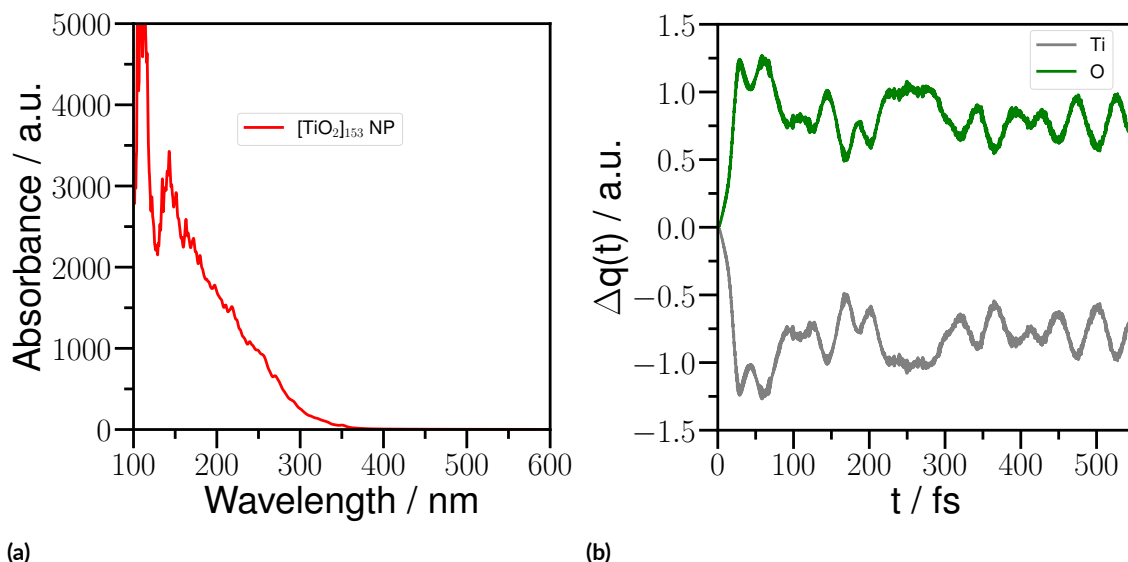


Figure 6.12: (a) Absorption spectra obtained using RT-TDDFTB approach (b) Changes in the Mulliken charges with respect to their ground-state values as a function of time.

and Ti atoms are accepting charge (negative)). In the discussion about photogenerated electrons and holes in semiconductors as TiO₂ anatase is well accepted the fact that the electron-hole lifetime is of several picoseconds, because is not possible a direct recombination and not only the life-time of the excited electron/hole pair is increased, also the diffusion and reaction time is increased.¹⁵² With no electron/hole recombination observed in the time scale studied in the Ehrenfest dynamics simulations, the role of excitonic properties should have an impact in the experimental behaviour reported. In our opinion, this results suggest the hypothesis that the polaron formation can induce lattice vibrations (small polarons by self-trapping on Ti⁴⁺ sites, causing the elongation of surrounding Ti–O bonds.).

The VASP code^{116,117,118,119} was employed to calculate the XAS for selected snapshots of the dynamics at initial state, at 150fs, and at 300 fs simulation time. The final state approx-

imation was used. Calculations were carried out at the Γ point and using PBE functional¹²⁰ with an energy cutoff of 450 eV and the projected augmented-wave method.^{121,122} The D2 method of Grimme¹⁵³ is included for dispersion corrections. A constant value of 0.5 eV for the Lorentzian broadening is used in the computation of the XAS spectrum.

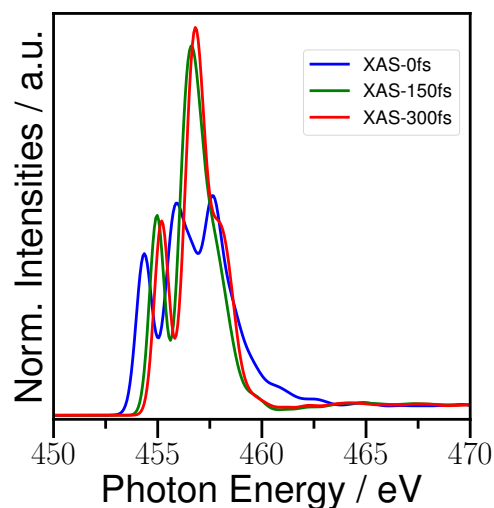


Figure 6.13: X-Ray Absorption Spectra for the $(\text{TiO}_2)_{153}$ nanoparticle system.

Due to limitations on the description of the core level energies by DFT methods is not captured the absolute values of the experimental peak positions.¹⁵⁴ Therefore, we applied a shift of 16 eV to the calculated peak positions of the spectrum to align to the experimental results, as done before.^{155,156} The results displayed in Figure 6.13 are in correspondence to the experimental observations, displaying a narrowing of the peaks corresponding with L-edge bands in TiO_2 nanoparticle.

For TiO_2 the most intense peak vibration is a typical phonon at 145 cm^{-1} .¹⁵⁷ Studies computing Raman spectra for TiO_2 nanoparticles reported six allowed modes appear at 144

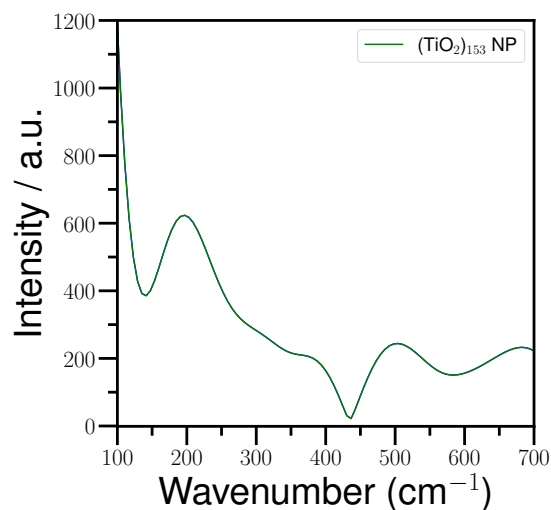


Figure 6.14: Fourier intensity spectra obtained from the Ehrenfest dynamics.

cm^{-1} (E_g), 197 cm^{-1} (E_g), 399 cm^{-1} (B_{1g}), 513 cm^{-1} (A_{1g}), 519 cm^{-1} (B_{1g}), and 639 cm^{-1} (E_g).^{158,159} To elucidate the nature of the oscillations during the Ehrenfest dynamics performed, a Fourier transform of the dynamics presented in Fig. 6.12b is showed in Fig. 6.14. The Raman bands are in good agreement with the described Raman frequencies of TiO_2 anatase, with a major contribution of the vibrational mode in the region of the 200 cm^{-1} .

Excitonic properties are predominant and direct linked to the observed behaviour from experiments. In our opinion, the photoinduced electron/hole formation and polaron effects are responsible for the narrowing of the peaks corresponding with L-edge bands in TiO_2 nanoparticles. The impact of the lattice vibrations underline the mechanism involved, with theory complementing the experimental results.

7

Conclusions

Computer simulations allow us to interpret with a reasonable accuracy, many physical processes that occur at the nanoscale when the systems are photoexcited. In the presented doctoral thesis, the three great pillars of the theoretical modeling have been supporting the research developed. From the description and understanding of the experimental questions addressed to facilitating the prediction of new observations with broad interest in the field of nanophotonics and nanotechnology.

The studies shown in Chapter 5 have focused on analyze the ultrafast photoinduced charge transfer in ligand protected Au₂₅ cluster labelled with a pyrene chromophore. Also, the theoretical outlook on light-induced charge separation of pyrene-functionalized middle and large-sized metalloid gold nanoclusters protected by phosphine ligands is investigated, with focus on the implications of electronic and steric contributions. Effectively, the applicability of the Ehrenfest dynamics on the ultrafast light-driven charge transfer processes in the studies mentioned is demonstrated, which represents a contribution to the experimental results and the future designing of nanodevices. In particular:

- Theory and experimental observations are in accordance, unraveling the ultrafast mechanism on the electron transfer from the ligand protected Au₂₅ cluster to the pyrene dye. The Ehrenfest dynamics based on RT-TD-DFTB approach used here is appropriate for describing the photoinduced events in such complex systems with a fast and low computational cost.
- A three steps mechanism is proposed as follow for the system IB:
 1. Initially the dye is photoexcited (< 50 fs),
 2. A charge transfer occurs directly from the Gold Nanocluster metallic core to the pyrene residue,
 3. The C₆H₁₃ protecting ligands stabilizes the photoinduced charge transfer by donating charge to the GNC core and pyrene unit.
- The results demonstrate the important role of the protecting ligands in the ultrafast charge transfer mechanism. Essentially, the importance of coherent vibronic couplings in the process is highlighted.

- The nature of the protecting ligands does not really modify the light-induced charge separation outcome, but do modify the mechanism of charge transfer, with pyrene residue acting as acceptor in any case, and the GNC core acting either as a donor or a second acceptor.
- With the increasing of the number of chromophores in the functionalization of the ligand protected Au₂₅ cluster system is obtained an increase on the amount of charge transferred, being the position of the labeling sensitive to control the charge transfer process.

The simulations performed on this thesis are a useful guidelines for designing gold-organics optoelectronic devices at the nanoscale. For the first time, an atomistic description of light-driven charge transfer dynamics in a set of pyrene-labeled middle-sized Au₇₀S₂₀(PH₃)₁₆, large-sized Au₁₀₈S₂₄(PR₃)₁₆ metalloid clusters is reported. In particular:

- The increasing of the size is not an advantage in order to achieve a superior light-driven charge separation, and middle sized GNC are possibly a optimal size. By a Fourier transform analysis of the dynamics, the effect of vibronic couplings is underlined. The systems investigated are sensitive to the nature of the predominant vibrational modes involved.
- The ultrafast nature and the missing back charge transfer are highlighted, proving the advantages of the functionalization using a pyrene derivate for photonics. For the complexes under study, Au₁₀₈S₂₄(PPh₃)₁₅PPh₂Pyr system exhibited the superlative performance.
- With the increase of the Tolman cone angle is observed an increase on the photoinduced charge transfer ability. This support the idea that the steric effects are more

significant than the π -acceptor capacity of the phosphine ligands considered.

The most important results of chapter 6 are derived from the study about photocatalysis on TiO₂ systems. The mechanism of the CO photooxidation on TiO₂ anatase 101 surface and the photoinduced hole transfer on H₂O-TiO₂ anatase 101 interface are explored. Additionally, the ultrafast decay of Ti L-edge bands in a TiO₂ nanoparticle is discussed.

Theory complements experiments that provide evidence of the ultrafast nature of CO photooxidation on TiO₂ anatase 101 surface. With the presence of O₂ molecule adsorbed on TiO₂ anatase 101 surface, a localized electronic state appears within the bandgap of the surface model. Theory highlights that different from the usual e/h pair generation, the O₂ activation is ruled by one photon interaction with energy of 1.6 eV, by accepting electron charge from the surface. This result highlights the possibility to trigger the photoreactions on TiO₂ with visible light instead of use ultraviolet light with shorter wavelengths.

Ehrenfest dynamics simulations fully corroborate experimental observations and allow us to clarify that interfacial hole transfer from TiO₂ to molecularly adsorbed water takes place within 285 fs. Our calculations suggest that this is preceded by the efficient trapping of the hole at the surface by hydroxyl species (OH) that form following the dissociative adsorption of water, highlighting the central role these species play during the photocatalytic process. This leads to a new Hydrogen bond forming between the surface and a physisorbed water molecule thereby facilitating efficient interfacial charge transfer, with the corresponding geometrical rearrangement resulting in a transient peak shift of the H₂O related core level component to lower binding energies.

The ultrafast decay of Ti L-edge bands in a $(\text{TiO}_2)_{153}$ nanoparticle is investigated by using ground-state and excited-states calculations. The theoretical X-Ray Absorption Spectra obtained for selected simulation times corresponding to initial state, at 150 fs, and at 300 fs of the dynamics corroborates the narrowing of the peaks corresponding with L-edge bands in the TiO_2 nanoparticle. The light-driven electron/hole formation is directly connected to the role of excitonic properties on the lattice vibrations with a superlative contribution of the vibrational mode in the region of the 200 cm^{-1} .

The insights provided in this thesis are of a great importance due to the accurate explanation of photoinduced charge transfer processes. The findings reported are applicable to a range of photocatalytic systems with interest in interdisciplinary fields such as materials science and physical chemistry. Making the methodologies employed a valuable tool in future research works.



List of Publications

1. Michael Wagstaffe, Lukas Wenthaus, **Adrian Domínguez-Castro**, Simon Chung, Guilherme Dalla Lana Semione, Steffen Palutke, Giuseppe Mercurio, Siarhei Dziarzhyski, Harald Redlin, Nicolai Klemke, Yudong Yang, Thomas Frauenheim, Adriel Dominguez, Franz Kärtner, Angel Rubio, Wilfried Wurth, Andreas Stierle, and Heshmat Noei. Ultrafast Real-Time Dynamics of CO Oxidation over an Oxide Photocatalyst. ACS Catal. 2020, 10, 22, 13650–13658. DOI: <https://doi.org/10.1021/acscatal.0c04098>

2. **Adrian Domínguez-Castro**, Carlos R. Lien Medrano, Khaoula Maghrebi, Sabri Mes-saoudi, Thomas Frauenheim, and Arnaud Fihey.
Photoinduced Charge-Transfer in Chromophore-Labeled Gold Nanoclusters: Quan-tum Evidence of the Critical Role of Ligands and Vibronic Couplings.
Nanoscale, 2021,13, 6786-6797. DOI:<https://doi.org/10.1039/D1NR00213A>
3. **Adrian Domínguez-Castro** and Thomas Frauenheim.
Impact of vibronic coupling effects on light-driven charge transfer in pyrene-functionalized middle and large-sized metalloid gold nanoclusters from Ehrenfest dynamics.
Phys. Chem. Chem. Phys., 2021,23, 17129-17133 DOI:<https://doi.org/10.1039/D1CP02890A>
4. Michael Wagstaffe, **Adrian Domínguez-Castro**, Lukas Wenthaus, Steffen Palutke, Dmytro Kutnyakhov, Michael Heber, Federico Pressacco, Siarhei Dziarzhyski, Helena Gleißner, Verena Kristin Gupta, Harald Redlin, Adriel Dominguez, Thomas Frauen-heim, Angel Rubio, Heshmat Noei, and Andreas Stierle
Ultrafast photoinduced dynamics at the interface of water and anatase TiO₂ (101)
(Paper in preparation)

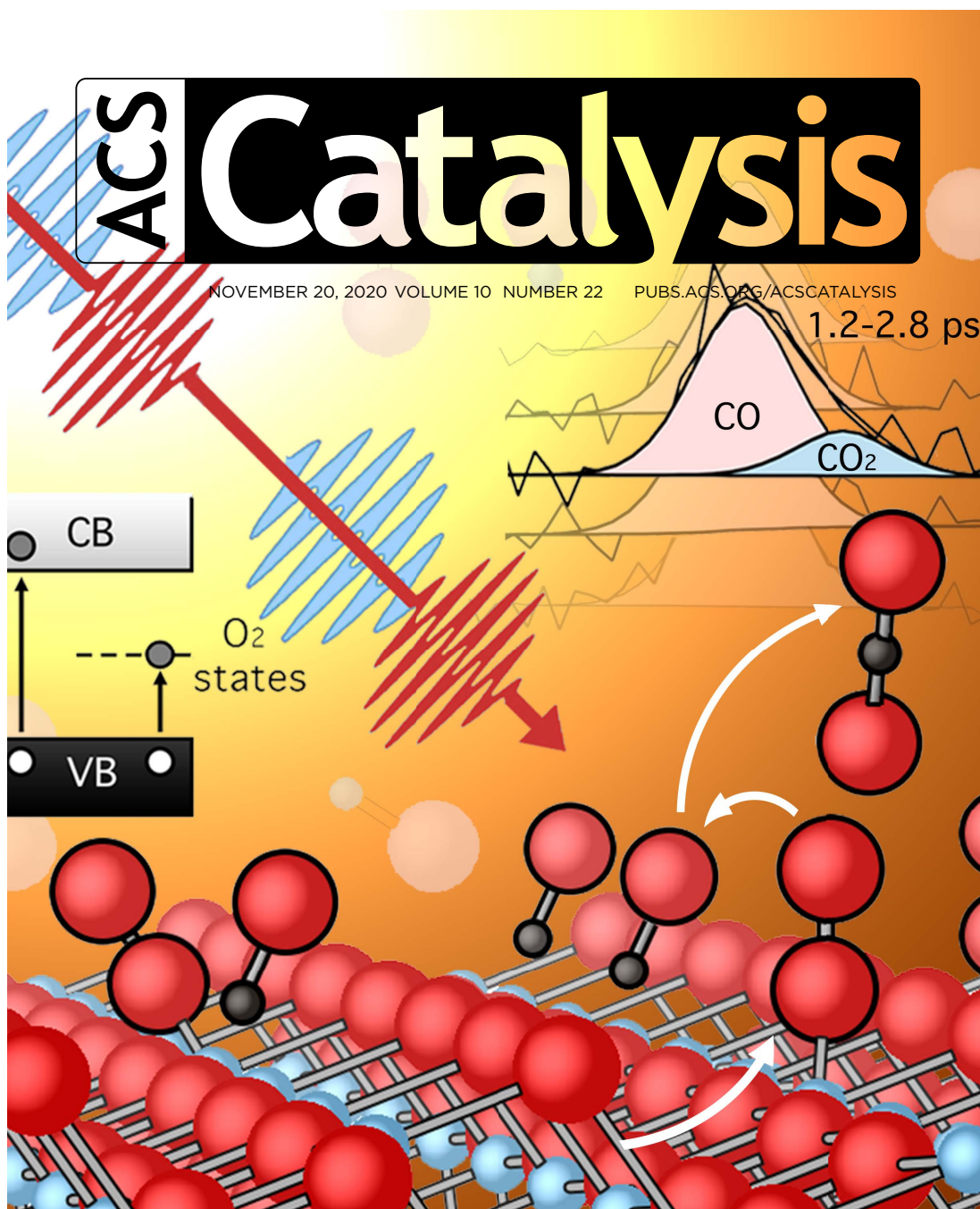
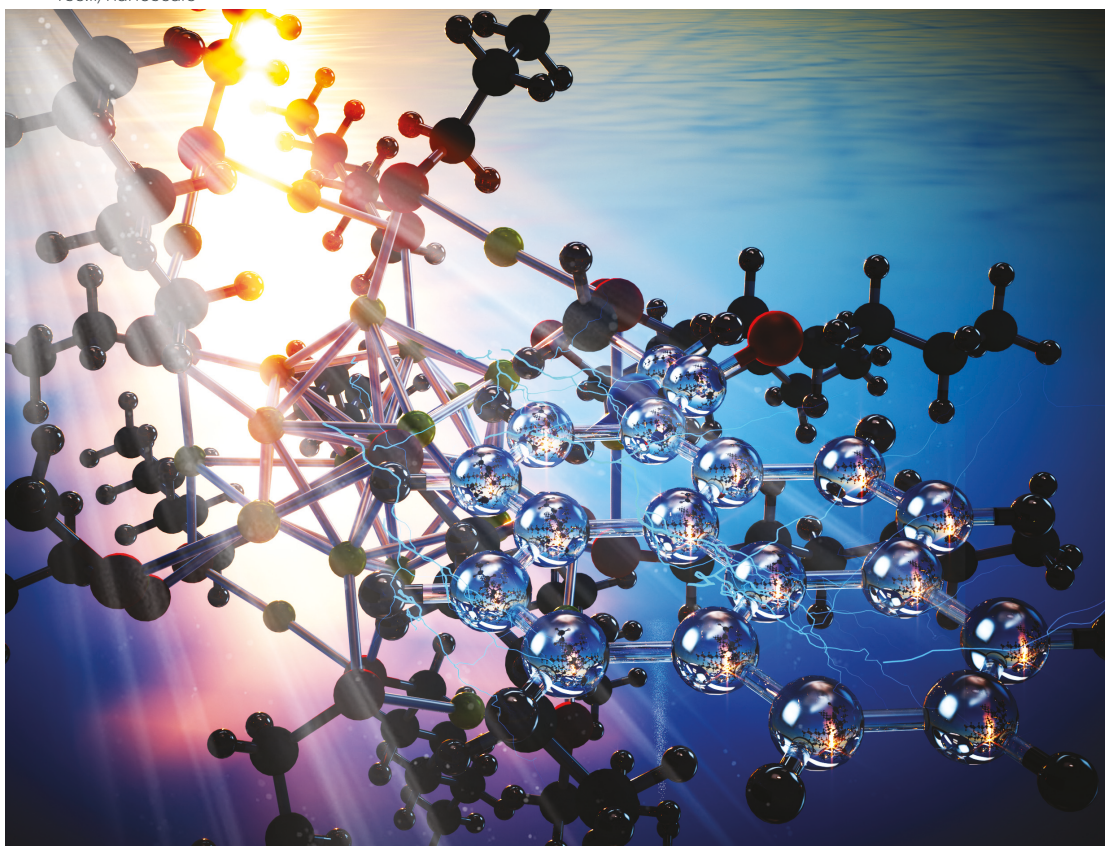


Figure A.1: The paper number 1 was selected as Cover of the ACS Catalysis journal.

Volume 13
Number 14
14 April 2021
Pages 6681-6998

Nanoscale

rsc.li/nanoscale



ISSN 2040-3372



PAPER

Carlos R. Lien-Medrano, Thomas Frauenheim,
Arnaud Fihey *et al.*
Photoinduced charge-transfer in chromophore-labeled gold
nanoclusters: quantum evidence of the critical role of ligands
and vibronic couplings



Figure A.2: The paper number 2 was selected as Inside Cover of the Nanoscale journal.

B

Appendix section 5.1

B.1 STUDY OF THE EFFECT OF THE TEMPERATURE IN THE CHARGE-TRANSFER PROCESSES: A CONFIGURATION SAMPLING

All the calculations were performed using the DFTB+ code. For the Bohr-Oppenheimer MD simulations, 25 ps were simulated. The equation of motion is integrated using the Velocity Verlet algorithm, with a time step of 0.25 fs. Temperature was set by a linear increas-

ing during the first 1000 steps and controlled at $T = 300$ K, using Andersen thermostat. Were selected 25 configurations. The initial configuration was taken at 12.5 ps, and every 0.5 ps between each one, in order to ensure decorrelation. The interval time is bigger than the decorrelation time calculated of 90 fs and 80 fs for Au₂₅ cluster-thiolated-pyrene system and Au₂₅ cluster-thiolated with C₆H₁₃ chains-pyrene system, respectively. (See below VAF Figures). Ehrenfest dynamics for each selected configuration and initial velocities sampled from the MD were performed. For the Ehrenfest dynamics, an electromagnetic wave, a sin² shaped pulse is employed describing the electron dynamics during the light absorption with an electric field of 0.1 V/Å and an energy laser of 400 nm (expressed in eV units equal to 3.0996). The total duration of the pulse is 100 fs in all cases. This method employed had been used with success in previous studies.

Figures B.1 and B.4 are represented the Classical MD Analysis demonstrating the stability of the systems under study here and validating the simulations. Figures B.2 and B.5 correspond with the VAF calculation for each case studied, respectively. And Figures B.3 (a) and (b), B.6 (a) and (b) the changes in the Mulliken charges with respect to their ground-state values as a function of time, are shown. Note, that in the first case under study (B.3) donor is referred as the Au₂₅ cluster-thiolated and acceptor is referred as the Pyrene residue. For the second case under study (B.6) donor is referred Au₂₅ cluster-thiolated with C₆H₁₃ chains cluster and acceptor is referred as the Pyrene residue.

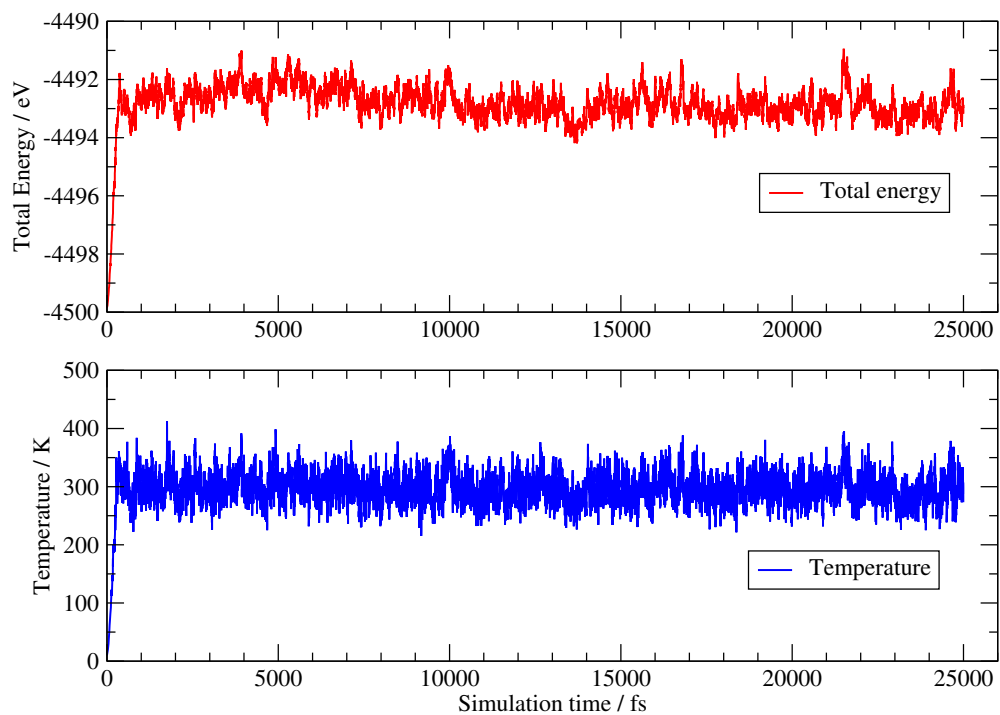


Figure B.1: Classical MD analysis: (up) Total Energy (bottom) Temperature during the simulation time for the IA system.

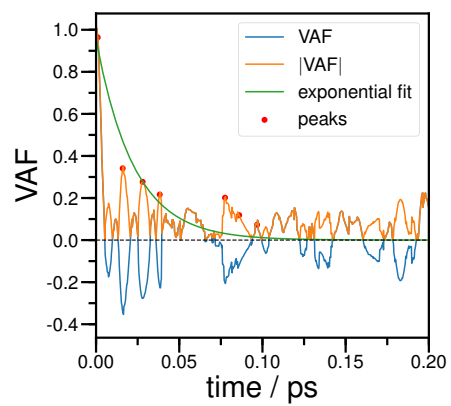
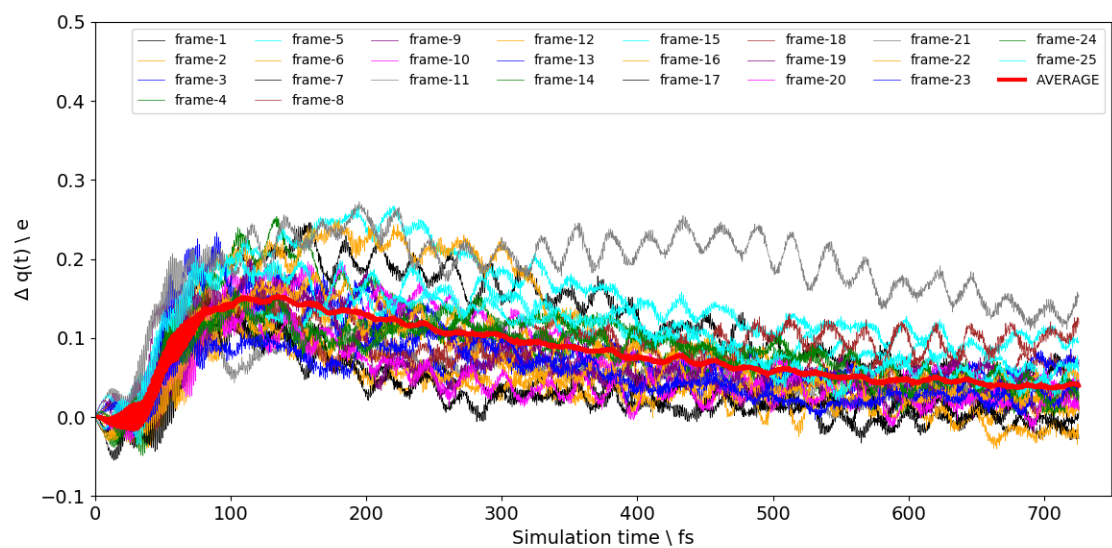
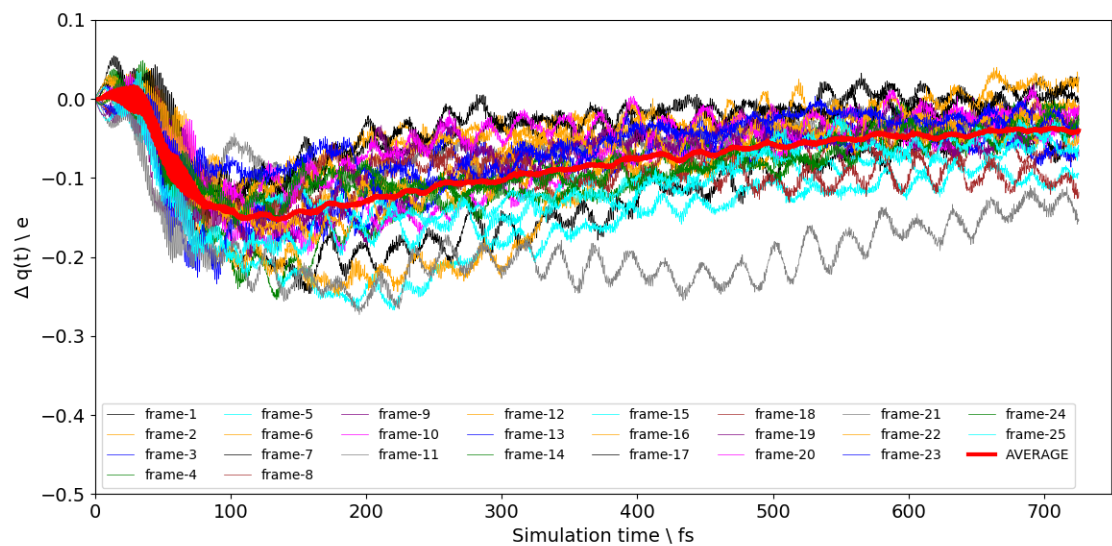


Figure B.2: Velocities autocorrelation function corresponding to the second half of the NVT dynamic.



(a)



(b)

Figure B.3: Changes in the Mulliken charges with respect to their ground-state values as a function of time for the donor in the IA system. (a) Donor contribution (b) Acceptor contribution. The average curve calculated from all the configuration sampled is represented in red.

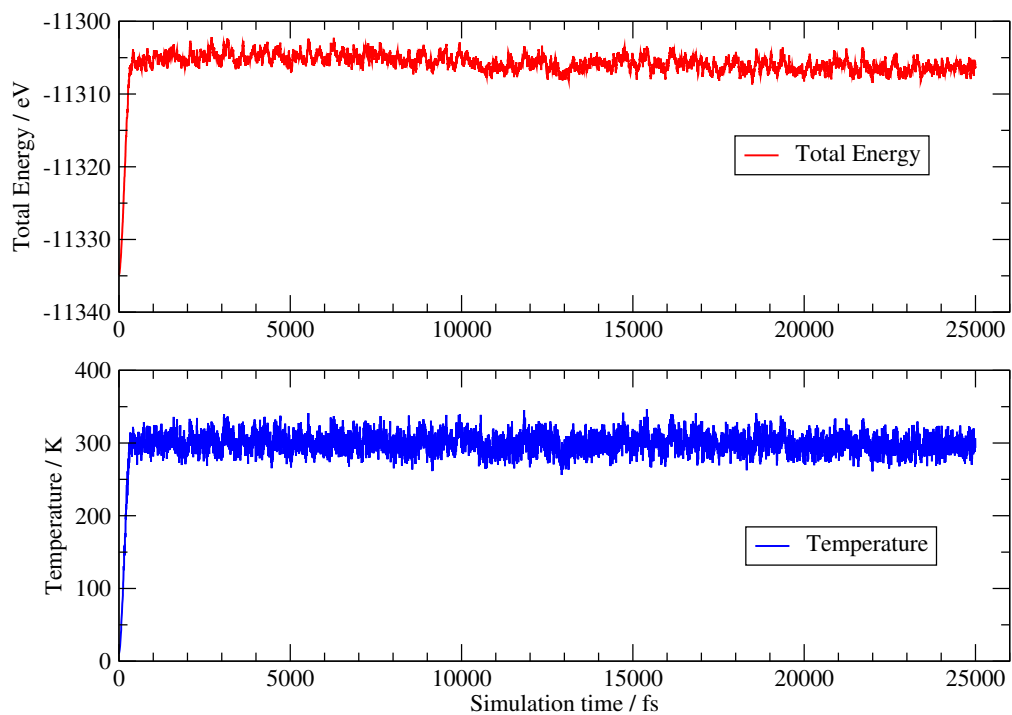


Figure B.4: Classical MD analysis: (up) Total Energy (bottom) Temperature during the simulation time for the IB system.

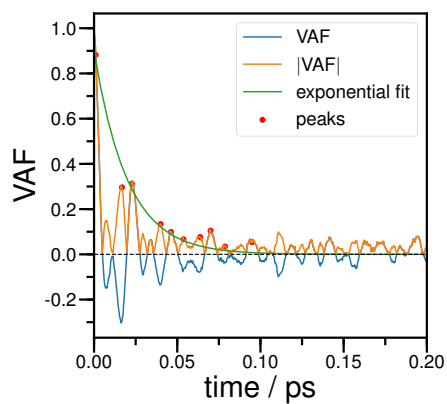
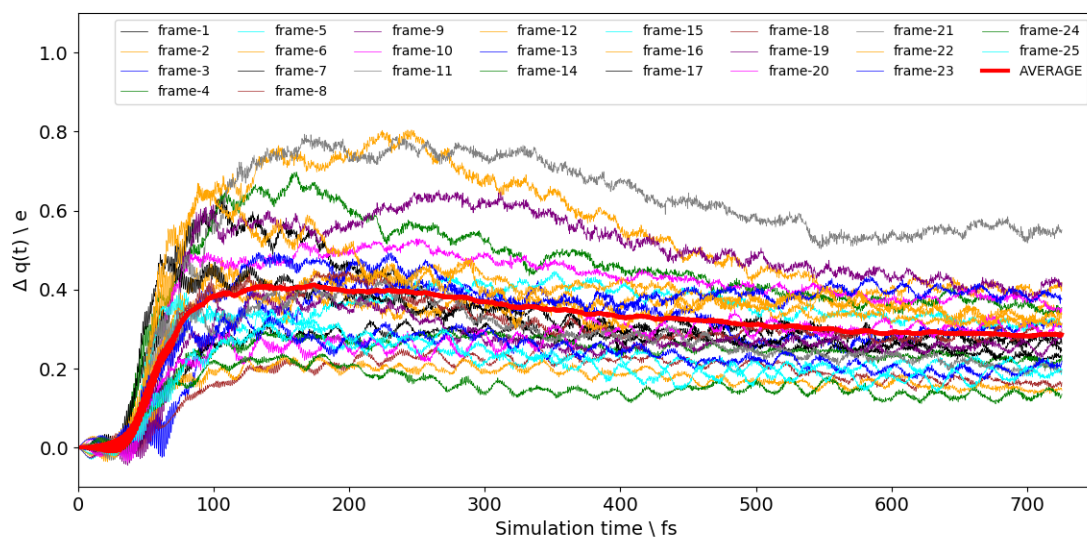
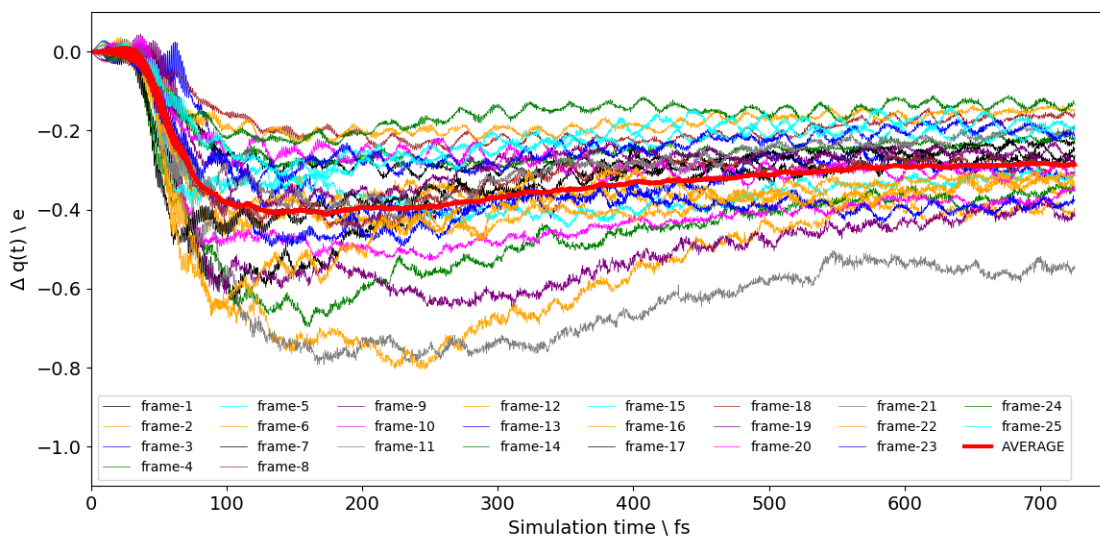


Figure B.5: Velocities autocorrelation function corresponding to the second half of the NVT dynamic.



(a)



(b)

Figure B.6: Changes in the Mulliken charges with respect to their ground-state values as a function of time for the donor in the IB system. (a) Donor contribution (b) Acceptor contribution. The average curve calculated from all the configuration sampled is represented in red.

C

Appendix section 5.2

C.1 ELECTRONIC STRUCTURE - DENSITY OF STATES

A DOS and PDOS is shown in Figure C.1 for $\text{Au}_{70}\text{S}_{20}(\text{PH}_3)_{11}\text{PH}_2\text{Pyr}$ and $\text{Au}_{108}\text{S}_{24}(\text{PH}_3)_{15}\text{PH}_2\text{Pyr}$ systems. The ΔHLG values reported of 0.46 eV and 0.47 eV for the middle-sized GNC systems and 0.63 eV and 0.65 eV for the large-sized systems, respectively. Practically, there are no variation on the ΔHLG values on the labeling with pyrene residue.

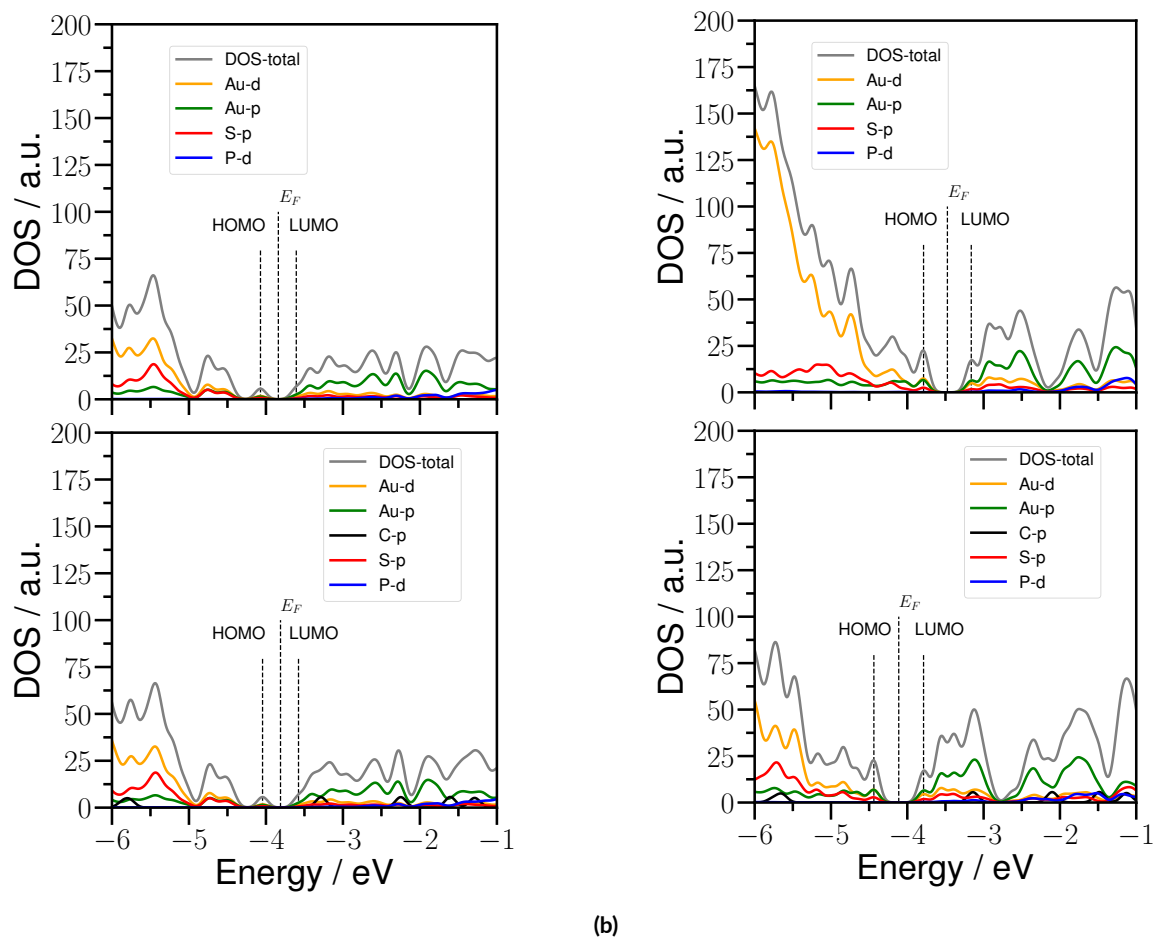


Figure C.1: DOS and PDOS analysis respectively for:
 (a) (top) $\text{Au}_{70}\text{S}_{20}(\text{PH}_3)_{12}$ system; (bottom) $\text{Au}_{70}\text{S}_{20}(\text{PH}_3)_{11}\text{PH}_2\text{Pyr}$ system
 (b) (top) $\text{Au}_{108}\text{S}_{24}(\text{PH}_3)_{16}$ system; (bottom) $\text{Au}_{108}\text{S}_{24}(\text{PH}_3)_{15}\text{PH}_2\text{Pyr}$ system

In Figure C.2 is displayed the calculated density of states (DOS) and partial density of states (PDOS) for $\text{Au}_{108}\text{S}_{24}(\text{PPh}_3)_{16}$ system (on top) and $\text{Au}_{108}\text{S}_{24}(\text{PPh}_3)_{15}\text{PPh}_2\text{Pyr}$ system (on bottom). The HOMO-LUMO gap (ΔHLG) for $\text{Au}_{108}\text{S}_{24}(\text{PPh}_3)_{16}$ system is 0.62 eV, in consonance with the validated result obtained by Irle et al.⁹⁴ The ΔHLG for $\text{Au}_{108}\text{S}_{24}(\text{PPh}_3)_{15}\text{PPh}_2\text{Pyr}$ system is 0.47 eV. From the DOS and PDOS analysis in Figure C.1, the Fermi level is decreased

resulting in the introduction of an electron acceptor dye as the pyrene derivative, from 2.90 eV for $\text{Au}_{108}\text{S}_{24}(\text{PPh}_3)_{16}$ to 3.46 eV for $\text{Au}_{108}\text{S}_{24}(\text{PPh}_3)_{15}\text{PPh}_2\text{Pyr}$ system, a shift of 0.56 eV. A reduction if compared with the value of $\text{Au}_{108}\text{S}_{24}(\text{PPh}_3)_{16}$ system. The Gold d and orbitals and Sulfur p orbital contribution to the bonding is clearly denoted in both cases. While the character of the unoccupied states is mainly of a Carbon p orbital nature. In the case of the LUMO orbital of the $\text{Au}_{108}\text{S}_{24}(\text{PPh}_3)_{15}\text{PPh}_2\text{Pyr}$ system the Carbon p orbital nature is re-

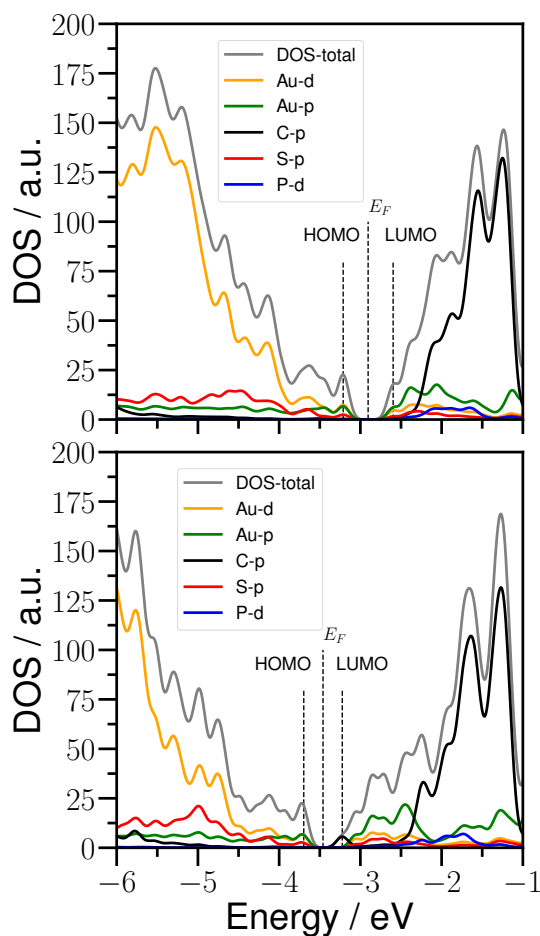


Figure C.2: DOS and PDOS analysis respectively for: (top) neutral $\text{Au}_{108}\text{S}_{24}(\text{PPh}_3)_{16}$ system; (bottom) neutral $\text{Au}_{108}\text{S}_{24}(\text{PPh}_3)_{15}\text{PPh}_2\text{Pyr}$ system.

markable. The barrier for excitations is decreased and the pyrene-labeled system can be more easily excited. In Figure C.3 for alkyl phosphine ligands is illustrated, the Δ HLG calculated for $\text{Au}_{108}\text{S}_{24}(\text{PCH}_3)_{16}$ and $\text{Au}_{108}\text{S}_{24}(\text{PC}_2\text{H}_5)_{16}$ systems is 0.63 eV and 0.62 eV, respectively. For the pyrene-labeled complexes with methyl and ethyl groups, a Δ HLG of 0.25 eV and 0.08 eV is computed.

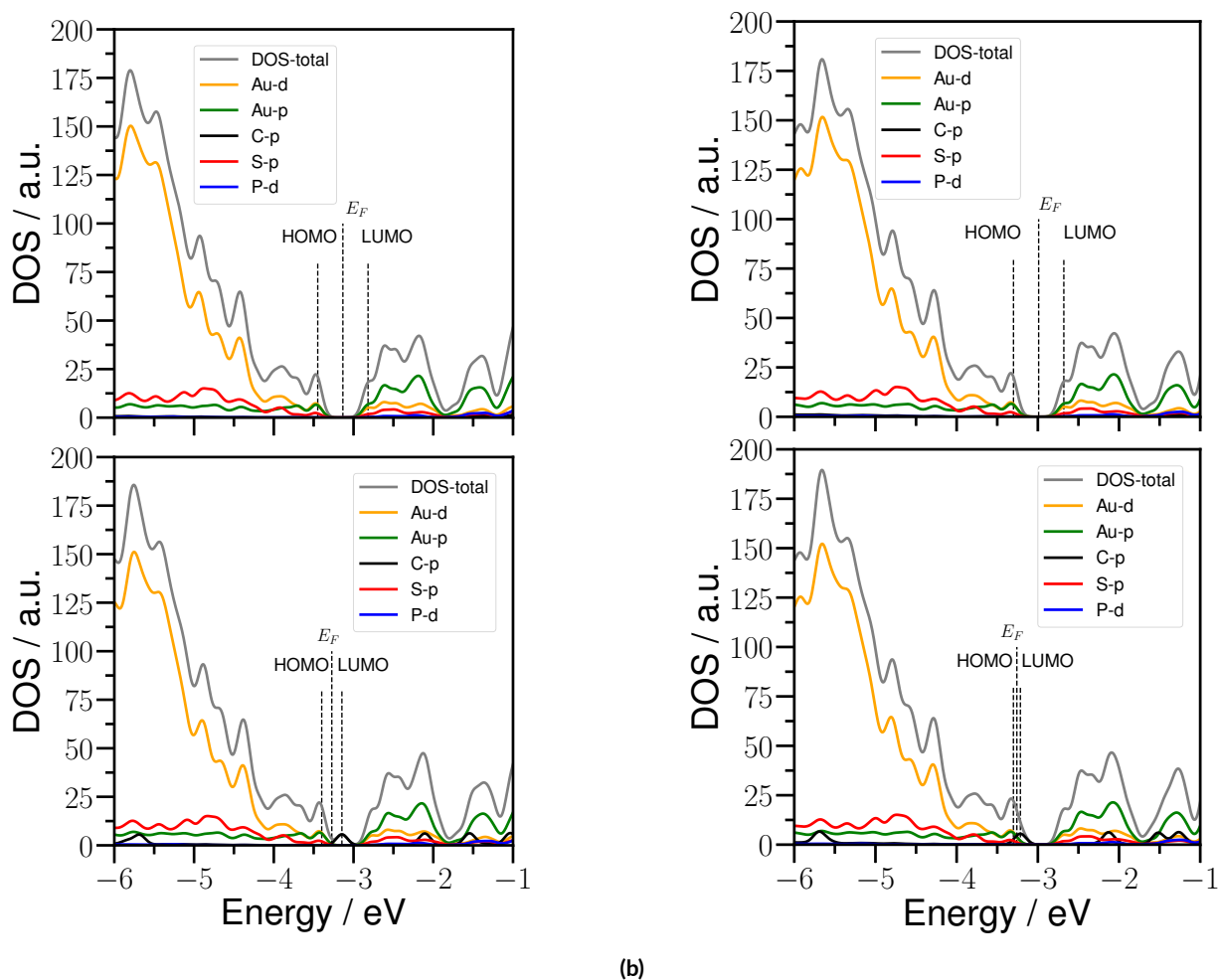


Figure C.3: DOS and PDOS analysis respectively for:
 (a) (top) $\text{Au}_{108}\text{S}_{24}(\text{PCH}_3)_{16}$ system; (bottom) $\text{Au}_{108}\text{S}_{24}(\text{PCH}_3)_{15}\text{P}(\text{CH}_3)_2\text{Pyr}$ system
 (b) (top) $\text{Au}_{108}\text{S}_{24}(\text{PC}_2\text{H}_5)_{16}$ system; (bottom) $\text{Au}_{108}\text{S}_{24}(\text{PC}_2\text{H}_5)_{15}\text{P}(\text{C}_2\text{H}_5)_2\text{Pyr}$ system.

D

Appendix section 6.1

The Figures represent the density of states (DOS) of the O₂ adsorption, O₂/CO coadsorption and TiO₂ pristine surface using DFTB approach respectively.

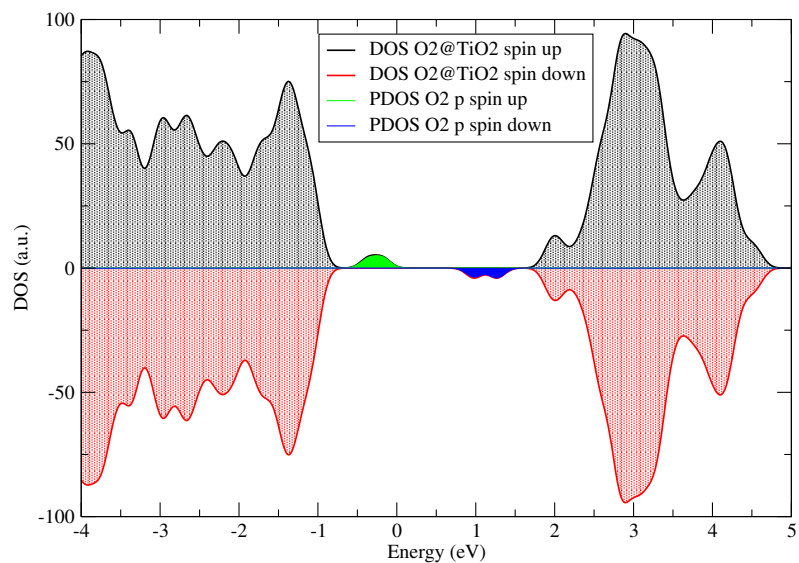


Figure D.1: DOS of the O₂ adsorption over TiO₂ anatase 101 surface using DFTB approach

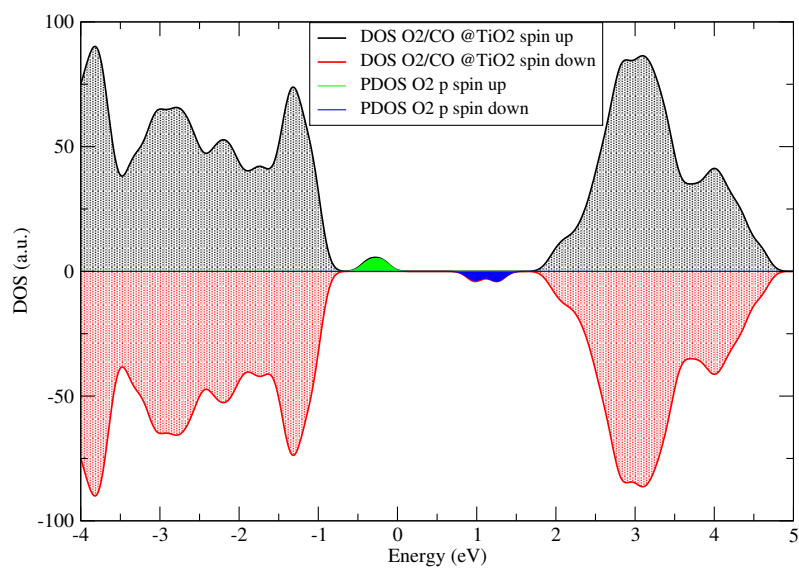


Figure D.2: DOS of the O₂/CO coadsorption over TiO₂ anatase 101 surface using DFTB approach

References

- [1] Dario Polli, Piero Altoè, Oliver Weingart, Katelyn M. Spillane, Cristian Manzoni, Daniele Brida, Gaia Tomasello, Giorgio Orlandi, Philipp Kukura, Richard A. Mathies, Marco Garavelli, and Giulio Cerullo. Conical intersection dynamics of the primary photoisomerization event in vision. , 467(7314):440–443, September 2010.
- [2] R. W. Schoenlein, L. A. Peteanu, R. A. Mathies, and C. V. Shank. The First Step in Vision: Femtosecond Isomerization of Rhodopsin. *Science*, 254(5030):412–415, October 1991.
- [3] Alicia Marcos Ramos, Minze T. Rispens, Jeroen K. J. van Duren, Jan C. Hummelen, and René A. J. Janssen. Photoinduced electron transfer and photovoltaic devices of a conjugated polymer with pendant fullerenes. *Journal of the American Chemical Society*, 123(27):6714–6715, 2001. PMID: 11439067.
- [4] M. H. B. Stowell, T. M. McPhillips, D. C. Rees, S. M. Soltis, E. Abresch, and G. Feher. Light-induced structural changes in photosynthetic reaction center: Implications for mechanism of electron-proton transfer. *Science*, 276(5313):812–816, 1997.
- [5] Michael Grätzel. Solar energy conversion by dye-sensitized photovoltaic cells. *Inorganic Chemistry*, 44(20):6841–6851, 2005. PMID: 16180840.
- [6] Basile F. E. Curchod and Todd J. Martínez. Ab initio nonadiabatic quantum molecular dynamics. *Chemical Reviews*, 118(7):3305–3336, 2018. PMID: 29465231.
- [7] Ahmed H Zewail. *Femtochemistry: Ultrafast Dynamics of the Chemical Bond*. World Scientific Publishing Company, 1994.
- [8] Ahmed H. Zewail. *Femtochemistry: Atomic-Scale Dynamics of the Chemical Bond Using Ultrafast Lasers (Nobel Lecture)*, chapter 1, pages 1–85. John Wiley Sons, Ltd, 2001.
- [9] Ulrike Diebold. The surface science of titanium dioxide. *Surface Science Reports*, 48(5):53–229, 2003.

- [10] Michael A. Henderson. A surface science perspective on TiO_2 photocatalysis. *Surface Science Reports*, 66(6):185–297, 2011.
- [11] Brian O'Regan and Michael Grätzel. A low-cost, high-efficiency solar cell based on dye-sensitized colloidal TiO_2 films. *Nature*, (353):737–740, 1991.
- [12] Akira Fujishima, Xintong Zhang, and Donald A. Tryk. TiO_2 photocatalysis and related surface phenomena. *Surface Science Reports*, 63(12):515–582, 2008.
- [13] Tracy L. Thompson and John T. Yates. Surface science studies of the photoactivation of TiO_2 new photochemical processes. *Chemical Reviews*, 106(10):4428–4453, 2006. PMID: 17031993.
- [14] Selim Alayoglu, Anand U. Nilekar, Manos Mavrikakis, and Bryan Eichhorn. Ru-Pt core-shell nanoparticles for preferential oxidation of carbon monoxide in hydrogen. *Nature Materials*, 7(4):333–338, April 2008.
- [15] Yan-Yan Yu and Xue qing Gong. Co oxidation at rutile $\text{TiO}_2(110)$: Role of oxygen vacancies and titanium interstitials. *ACS Catalysis*, 5:2042–2050, 2015.
- [16] Georgios A. Tritsarlis, Dmitry Vinichenko, Grigory Kolesov, Cynthia M. Friend, and Efthimios Kaxiras. Dynamics of the photogenerated hole at the rutile $\text{TiO}_2(110)$ /water interface: A nonadiabatic simulation study. *The Journal of Physical Chemistry C*, 118(47):27393–27401, 2014.
- [17] Shengli Zhuang, Lingwen Liao, Jinyun Yuan, Chengming Wang, Yan Zhao, Nan Xia, Zibao Gan, Wanmiao Gu, Jin Li, Haiteng Deng, Jinlong Yang, and Zhikun Wu. Kernel homology in gold nanoclusters. *Angewandte Chemie International Edition*, 57(47):15450–15454, 2018.
- [18] Zhikun Wu and Rongchao Jin. On the ligand's role in the fluorescence of gold nanoclusters. *Nano Lett*, 10:2568–2573, 2010.
- [19] Valérie Schwanen and Françoise Remacle. Photoinduced ultrafast charge transfer and charge migration in small gold clusters passivated by a chromophoric ligand. *Nano Lett*, 17:5672–5681, 2017.
- [20] Deng Hao-Hua, Huang Kai-Yuan, Zhu Chen-Ting, Shen Jian-Feng, Zhang Xiang-Ping, Peng Hua-Ping, Xia Xing-Hua, and Wei Chen. Bell-shaped electron transfer kinetics in gold nanoclusters. *J. Phys. Chem. Lett.*, 12:876–883, 2021.
- [21] Wolfram Koch and Max C. Holthausen. *A Chemist's Guide to Density Functional Theory, 2nd Edition*. Wiley & Sons, Inc., 2001.
- [22] Ira N. Levine. *Quantum Chemistry, 7th Edition*. Pearson, 2014.

- [23] P. Geerlings, F. De Proft, and W. Langenaeker. Conceptual density functional theory. *Chemical Reviews*, 103(5):1793–1874, 2003. PMID: 12744694.
- [24] Sérgio Filipe Sousa, Pedro Alexandrino Fernandes, and Maria João Ramos. General performance of density functionals. *The Journal of Physical Chemistry A*, 111(42):10439–10452, 2007. PMID: 17718548.
- [25] S. H. Vosko, L. Wilk, and M. Nusair. Accurate spin-dependent electron liquid correlation energies for local spin density calculations: a critical analysis. *Canadian Journal of Physics*, 59:1200, August 1980.
- [26] A. D. Becke. Density functional calculations of molecular bond energies. *The Journal of Chemical Physics*, 84(8):4524–4529, 1986.
- [27] Axel D. Becke. Density-functional thermochemistry. i. the effect of the exchange-only gradient correction. *The Journal of Chemical Physics*, 96(3):2155–2160, 1992.
- [28] Axel D. Becke. Density-functional thermochemistry. ii. the effect of the perdew–wang generalized-gradient correlation correction. *The Journal of Chemical Physics*, 97(12):9173–9177, 1992.
- [29] Axel D. Becke. Density-functional thermochemistry. iii. the role of exact exchange. *The Journal of Chemical Physics*, 98(7):5648–5652, 1993.
- [30] Axel D. Becke. Density-functional thermochemistry. iv. a new dynamical correlation functional and implications for exact-exchange mixing. *The Journal of Chemical Physics*, 104(3):1040–1046, 1996.
- [31] Axel D. Becke. Density-functional thermochemistry. v. systematic optimization of exchange-correlation functionals. *The Journal of Chemical Physics*, 107(20):8554–8560, 1997.
- [32] John P. Perdew, Stefan Kurth, Aleš Zupan, and Peter Blaha. Accurate density functional with correct formal properties: A step beyond the generalized gradient approximation. *Phys. Rev. Lett.*, 82:2544–2547, Mar 1999.
- [33] Chengteh Lee, Weitao Yang, and Robert G. Parr. Development of the colle-salvetti correlation-energy formula into a functional of the electron density. *Phys. Rev. B*, 37:785–789, Jan 1988.
- [34] John P. Perdew and Yue Wang. Accurate and simple analytic representation of the electron-gas correlation energy. *Phys. Rev. B*, 45:13244–13249, Jun 1992.
- [35] John P. Perdew, J. A. Chevary, S. H. Vosko, Koblar A. Jackson, Mark R. Pederson, D. J. Singh, and Carlos Fiolhais. Atoms, molecules, solids, and surfaces: Applications

- of the generalized gradient approximation for exchange and correlation. *Phys. Rev. B*, 46:6671–6687, Sep 1992.
- [36] John P. Perdew, Kieron Burke, and Matthias Ernzerhof. Generalized gradient approximation made simple. *Phys. Rev. Lett.*, 77:3865–3868, Oct 1996.
- [37] Jorge Kohanoff. *Electronic Structure Calculations for Solids and Molecules: Theory and Computational Methods*. Cambridge University Press, 2006.
- [38] Christoph Heinemann, Wolfram Koch, and Helmut Schwarz. An approximate method for treating spin-orbit effects in platinum. *Chemical Physics Letters*, 245(4):509–518, 1995.
- [39] John P. Perdew and Karla Schmidt. Jacob’s ladder of density functional approximations for the exchange-correlation energy. *AIP Conference Proceedings*, 577(1):1–20, 2001.
- [40] Erich Runge and E. K. U. Gross. Density-functional theory for time-dependent systems. *Phys. Rev. Lett.*, 52:997–1000, Mar 1984.
- [41] Carsten A. Ullrich. *Time-Dependent Density-Functional Theory: Concepts and Applications*. Oxford University Press, 2011.
- [42] Miguel A.L. Marques, Neepa T. Maitra, Fernando M.S. Nogueira, E.K.U. Gross, and Angel Rubio. *Fundamentals of Time-Dependent Density Functional Theory*. Springer Berlin, Heidelberg, 2012.
- [43] MARK E. CASIDA. *Time-Dependent Density Functional Response Theory for Molecules*, pages 155–192.
- [44] Marcus Elstner and Gotthard Seifert. Density functional tight binding. *Philosophical Transactions of the Royal Society A: Mathematical, Physical and Engineering Sciences*, 372(2011):20120483, 2014.
- [45] Martin Stöhr, Leonardo Medrano Sandonas, and Alexandre Tkatchenko. Accurate many-body repulsive potentials for density-functional tight binding from deep tensor neural networks. *The Journal of Physical Chemistry Letters*, 11(16):6835–6843, 2020. PMID: 32787209.
- [46] B. Hourahine, B. Aradi, V. Blum, F. Bonafé, A. Buccheri, C. Camacho, C. Cevallos, M. Y. Deshayé, T. Dumitrică, A. Dominguez, S. Ehlert, M. Elstner, T. van der Heide, J. Hermann, S. Irle, J. J. Kranz, C. Köhler, T. Kowalczyk, T. Kubař, I. S. Lee, V. Lutsker, R. J. Maurer, S. K. Min, I. Mitchell, C. Negre, T. A. Niehaus, A. M. N. Niklasson, A. J. Page, A. Pecchia, G. Penazzi, M. P. Persson, J. Řezáč, C. G. Sánchez,

- M. Sternberg, M. Stöhr, F. Stuckenberg, A. Tkatchenko, V. W.-z. Yu, and T. Frauenheim. Dftb+, a software package for efficient approximate density functional theory based atomistic simulations. *The Journal of Chemical Physics*, 152(12):124101, 2020.
- [47] C M Goringe, D R Bowler, and E Hernández. Tight-binding modelling of materials. *Reports on Progress in Physics*, 60(12):1447–1512, dec 1997.
- [48] D. Porezag, Th. Frauenheim, Th. Köhler, G. Seifert, and R. Kaschner. Construction of tight-binding-like potentials on the basis of density-functional theory: Application to carbon. *Phys. Rev. B*, 51:12947–12957, May 1995.
- [49] Augusto F. Oliveira, Gotthard Seifert, Thomas Heine, and Hélio A. Duarte. Density-functional based tight-binding: An approximate dft method. *Journal of the Brazilian Chemical Society*, 20(7):1193–1205, 2009.
- [50] M. Elstner, D. Porezag, G. Jungnickel, J. Elsner, M. Haugk, Th. Frauenheim, S. Suhai, and G. Seifert. Self-consistent-charge density-functional tight-binding method for simulations of complex materials properties. *Phys. Rev. B*, 58:7260–7268, Sep 1998.
- [51] R. S. Mulliken. Electronic population analysis on lcao–mo molecular wave functions. i. *The Journal of Chemical Physics*, 23(10):1833–1840, 1955.
- [52] Nikos L Doltsinis. Nonadiabatic dynamics: mean-field and surface hopping. *Quantum simulations of complex many-body systems: from theory to algorithms*, 10:377–397, 2002.
- [53] A.D. McLachlan. A variational solution of the time-dependent schrodinger equation. *Molecular Physics*, 8(1):39–44, 1964.
- [54] Joseph E. Subotnik. Augmented ehrenfest dynamics yields a rate for surface hopping. *The Journal of Chemical Physics*, 132(13):134112, 2010.
- [55] John C. Tully. Molecular dynamics with electronic transitions. *The Journal of Chemical Physics*, 93(2):1061–1071, 1990.
- [56] M. Born and R. Oppenheimer. Zur Quantentheorie der Molekeln. *Annalen der Physik*, 389(20):457–484, January 1927.
- [57] H. Köuppel, W. Domcke, and Lorenz Cederbaum. *Multimode Molecular Dynamics Beyond the Born-Oppenheimer Approximation*, volume 57, pages 59 – 246. 03 2007.
- [58] A. Jabłoński. Efficiency of Anti-Stokes Fluorescence in Dyes. *Nature*, 131(3319):839–840, June 1933.

- [59] B. Lasorne, M. A. Robb, and G. A. Worth. Direct quantum dynamics using variational multi-configuration gaussian wavepackets. implementation details and test case. *Phys. Chem. Chem. Phys.*, 9:3210–3227, 2007.
- [60] G.W. Richings, I. Polyak, K.E. Spinlove, G.A. Worth, I. Burghardt, and B. Lasorne. Quantum dynamics simulations using gaussian wavepackets: the vmcg method. *International Reviews in Physical Chemistry*, 34(2):269–308, 2015.
- [61] Yuxiu Liu and Chaoyuan Zhu. Trajectory surface hopping molecular dynamics simulations for retinal protonated schiff-base photoisomerization. *Phys. Chem. Chem. Phys.*, 23:23861–23874, 2021.
- [62] M. Ben-Nun and Todd J. Martínez. Nonadiabatic molecular dynamics: Validation of the multiple spawning method for a multidimensional problem. *The Journal of Chemical Physics*, 108(17):7244–7257, 1998.
- [63] Patricia Vindel-Zandbergen, Spiridoula Matsika, and Neepa T. Maitra. Exact-factorization-based surface hopping for multistate dynamics. *The Journal of Physical Chemistry Letters*, 13(7):1785–1790, 2022. PMID: 35170972.
- [64] Sheng Meng and Efthimios Kaxiras. Real-time, local basis-set implementation of time-dependent density functional theory for excited state dynamics simulations. *The Journal of Chemical Physics*, 129(5):054110, 2008.
- [65] Grigory Kolesov, Dmitry Vinichenko, Georgios A. Tritsaris, Cynthia M. Friend, and Efthimios Kaxiras. Anatomy of the photochemical reaction: Excited-state dynamics reveals the c–h acidity mechanism of methoxy photo-oxidation on titania. *The Journal of Physical Chemistry Letters*, 6(9):1624–1627, 2015. PMID: 26263325.
- [66] P. Ehrenfest. Bemerkung über die angenäherte Gültigkeit der klassischen Mechanik innerhalb der Quantenmechanik. *Zeitschrift für Physik*, 45(7-8):455–457, July 1927.
- [67] Alexey V. Akimov and Oleg V. Prezhdo. The pyxaid program for non-adiabatic molecular dynamics in condensed matter systems. *Journal of Chemical Theory and Computation*, 9(11):4959–4972, 2013. PMID: 26583414.
- [68] Walter Malone, Benjamin Nebgen, Alexander White, Yu Zhang, Huajing Song, Josiah A. Bjorgaard, Andrew E. Sifain, Beatriz Rodriguez-Hernandez, Victor M. Freixas, Sebastian Fernandez-Alberti, Adrian E. Roitberg, Tammie R. Nelson, and Sergei Tretiak. Nexmd software package for nonadiabatic excited state molecular dynamics simulations. *Journal of Chemical Theory and Computation*, 16(9):5771–5783, 2020. PMID: 32635739.

- [69] Qijing Zheng, Weibin Chu, Chuanyu Zhao, Lili Zhang, Hongli Guo, Yanan Wang, Xiang Jiang, and Jin Zhao. Ab initio nonadiabatic molecular dynamics investigations on the excited carriers in condensed matter systems. *Wiley Interdisciplinary Reviews: Computational Molecular Science*, 9:e1411, 03 2019.
- [70] Alexey Akimov. Libra: An open-source "methodology discovery" library for quantum and classical dynamics simulations. *Journal of computational chemistry*, 37, 03 2016.
- [71] Mario Barbatti, Matthias Ruckebauer, Felix Plasser, Jiri Pittner, Giovanni Granucci, Maurizio Persico, and Hans Lischka. Newton-x: A surface-hopping program for nonadiabatic molecular dynamics. *Wiley Interdisciplinary Reviews: Computational Molecular Science*, 4, 01 2014.
- [72] Adrian Domínguez-Castro, Carlos R. Lien-Medrano, Khaoula Maghrebi, Sabri Messaoudi, Thomas Frauenheim, and Arnaud Fihey. Photoinduced charge-transfer in chromophore-labeled gold nanoclusters: quantum evidence of the critical role of ligands and vibronic couplings. *Nanoscale*, 13:6786–6797, 2021.
- [73] Adrian Domínguez-Castro and Thomas Frauenheim. Impact of vibronic coupling effects on light-driven charge transfer in pyrene-functionalized middle and large-sized metalloid gold nanoclusters from ehrenfest dynamics. *Phys. Chem. Chem. Phys.*, 23:17129–17133, 2021.
- [74] Sebastian Kenzler and Andreas Schnepf. Metalloid gold clusters – past, current and future aspects. *Chem. Sci.*, 12:3116–3129, 2021.
- [75] Faraday M. X. the bakerian lecture. —experimental relations of gold (and other metals) to light. *Phil. Trans. R. Soc.*, 47:145–181, 1857.
- [76] Mary Sajini Devadas, Junhyung Kim, Ekkehard Sinn, Dongil Lee, Theodore Goodson, and Guda Ramakrishna. Unique ultrafast visible luminescence in monolayer-protected au₂₅ clusters. *The Journal of Physical Chemistry C*, 114(51):22417–22423, 2010.
- [77] Arnaud Fihey, Christian Hettich, Jérémy Touzeau, François Maurel, Aurélie Perrier, Christof Köhler, Bálint Aradi, and Thomas Frauenheim. Scc-dftb parameters for simulating hybrid gold-thiolates compounds. *J. Comput. Chem.*, 36(27):2075–2087, 2015.
- [78] Mary Sajini Devadas, Kyuju Kwak, Jung-Woo Park, Ji-Hwan Choi, Chul-Ho Jun, Ekkehard Sinn, Guda Ramakrishna, and Dongil Lee. Directional electron transfer in chromophore-labeled quantum-sized au₂₅ clusters: Au₂₅ as an electron donor. *J. Phys. Chem. Lett.*, 1(9):1497–1503, 2010.

- [79] A. Nitzan. *Chemical Dynamics in Condensed Phases: Relaxation, Transfer, and Reactions in Condensed Molecular Systems*. Oxford University Press, 2006.
- [80] Arnaud Fihey, François Maurel, and Aurélie Perrier. Modeling the absorbance properties of a pyrene chromophore grafted onto a au₂₅ nanocluster: A td-dft study. *J. Phys. Chem. C*, 118(8):4444–4453, 2014.
- [81] Van Quan Vuong, Jissy Akkarapattiakal Kuriappan, Maximilian Kubillus, Julian J. Kranz, Thilo Mast, Thomas A. Niehaus, Stephan Irle, and Marcus Elstner. Parametrization and benchmark of long-range corrected dftb2 for organic molecules. *J. Chem. Theory Comput.*, 14(1):115–125, 2018.
- [82] Franco P. Bonafé, Bálint Aradi, Ben Hourahine, Carlos R. Medrano, Federico J. Hernández, Thomas Frauenheim, and Cristián G. Sánchez. A Real-Time Time-Dependent Density Functional Tight-Binding Implementation for Semiclassical Excited State Electron–Nuclear Dynamics and Pump–Probe Spectroscopy Simulations. *Journal of Chemical Theory and Computation*, 16(7):4454–4469, jul 2020.
- [83] Carlo Andrea Rozzi, Sarah Maria Falke, Nicola Spallanzani, Angel Rubio, Elisa Molinari, Daniele Brida, Margherita Maiuri, Giulio Cerullo, Heiko Schramm, Jens Christoffers, and Christoph Lienau. Quantum coherence controls the charge separation in a prototypical artificial light-harvesting system. *Nature communications*, 4:1602, 2013.
- [84] Sarah Maria Falke, Carlo Andrea Rozzi, Daniele Brida, Margherita Maiuri, Michele Amato, Ephraim Sommer, Antonietta De Sio, Angel Rubio, Giulio Cerullo, Elisa Molinari, and Christoph Lienau. Coherent ultrafast charge transfer in an organic photovoltaic blend. *Science (New York, N.Y.)*, 344(6187):1001–1005, 2014.
- [85] N. Sheppard. The vibrational spectra of some organic sulphur compounds and the characteristic frequencies of c–s linkages. *Trans. Faraday Soc.*, 46:429–439, 1950.
- [86] Ernest J. Bastian and R. Bruce Martin. Disulfide vibrational spectra in the sulfur-sulfur and carbon-sulfur stretching region. *J. Phys. Chem.*, 77(9):1129–1133, 1973.
- [87] Birte Varnholt, Patric Oulevey, Sandra Lubber, Chanaka Kumara, Amala Dass, and Thomas Bürgi. Structural information on the au–s interface of thiolate-protected gold clusters: A raman spectroscopy study. *J. Phys. Chem. C*, 118(18):9604–9611, 2014.
- [88] Thomas Bürgi. Properties of the gold–sulphur interface: from self-assembled monolayers to clusters. *Nanoscale*, 7:15553–15567, 2015.

- [89] Yuanxin Du, Hongting Sheng, Didier Astruc, and Manzhou Zhu. Atomically precise noble metal nanoclusters as efficient catalysts: A bridge between structure and properties. *Chem. Rev.*, 120(2):526–622, 2020.
- [90] Manzhou Zhu, Christine M. Aikens, Frederick J. Hollander, George C. Schatz, and Rongchao Jin. Correlating the crystal structure of a thiol-protected Au_{25} cluster and optical properties. *J. Am. Chem. Soc.*, 130(18):5883–5885, 2008.
- [91] Birte Varnholt, Romain Letrun, Jesse J. Bergkamp, Yongchun Fu, Oleksandr Yushchenko, Silvio Decurtins, Eric Vauthey, Shi-Xia Liu, and Thomas Burgi. Excited state interactions between the chiral $\text{Au}_{38}\text{I}_{24}$ cluster and covalently attached porphyrin. *Phys. Chem. Chem. Phys.*, 17:14788–14795, 2015.
- [92] Sebastian Kenzler, Claudio Schrenk, and Andreas Schnepf. $\text{Au}_{108}\text{S}_{24}(\text{pph}_3)_{16}$: A highly symmetric nanoscale gold cluster confirms the general concept of metalloid clusters. *Angewandte Chemie International Edition*, 56(1):393–396, 2017.
- [93] Sebastian Kenzler, Claudio Schrenk, Andrew R. Frojd, Hannu Häkkinen, Andre Z. Clayborne, and Andreas Schnepf. $\text{Au}_{70}\text{S}_{20}(\text{pph}_3)_{12}$: an intermediate sized metalloid gold cluster stabilized by the Au_4S_4 ring motif and Au-pph_3 groups. *Chem. Commun.*, 54:248–251, 2018.
- [94] Van Quan Vuong, Jenica Marie L. Madrideojos, Bálint Aradi, Bobby G. Sumpter, Gregory F. Metha, and Stephan Irlé. Density-functional tight-binding for phosphine-stabilized nanoscale gold clusters. *Chem. Sci.*, 11:13113–13128, 2020.
- [95] Carlos R. Medrano and Cristián G. Sánchez. Trap-door-like irreversible photoinduced charge transfer in a donor–acceptor complex. *J. Phys. Chem. Lett.*, 9(12):3517–3524, 2018.
- [96] Adrian Domínguez-Castro, Fernando Guzmán, and Yasser Novo-Fernández. Adsorption on a nanoporous organic polymer for clean energy applications: A multiscale modeling study using density functional tight binding approach. *Computational and Theoretical Chemistry*, 1102:30–37, 2017.
- [97] Adrian Domínguez-Castro, Dariel Hernández, and Fernando Guzmán. Insights into the interactions of biomolecules with small gold clusters: a theoretical study from a dftb perspective. *Theoretical Chemistry Accounts*, 136:84, 2017.
- [98] Michael Wagstaffe, Lukas Wenthaus, Adrian Dominguez-Castro, Simon Chung, Guilherme Dalla Lana Semione, Steffen Palutke, Giuseppe Mercurio, Siarhei Dziarzhyski, Harald Redlin, Nicolai Klemke, Yudong Yang, Thomas Frauenheim, Adriel Dominguez, Franz Kärtner, Angel Rubio, Wilfried Wurth, Andreas Stierle, and Heshmat Noei. Ultrafast real-time dynamics of co oxidation over an oxide photocatalyst. *ACS Catalysis*, 10(22):13650–13658, 2020.

- [99] Chadwick A. Tolman. Steric effects of phosphorus ligands in organometallic chemistry and homogeneous catalysis. *Chemical Reviews*, 77(3):313–348, 1977.
- [100] Jong Hyun Kim, Evan Reeder, Sean Parkin, and Samuel G. Awuah. Gold(i/iii)-phosphine complexes as potent antiproliferative agents. *Scientific Reports*, 9:12335, 2019.
- [101] Emilie B. Guidez and Christine M. Aikens. Time-dependent density functional theory study of the luminescence properties of gold phosphine thiolate complexes. *The Journal of Physical Chemistry A*, 119(14):3337–3347, 2015.
- [102] Eduardo J. Fernández, M. Concepción Gimeno, Antonio Laguna, José M. López-de Luzuriaga, Miguel Monge, Pekka Pyykkö, and Dage Sundholm. Luminescent characterization of solution oligomerization process mediated gold-gold interactions. dft calculations on $[\text{auzag}_2\text{r}_4\text{l}_2]_n$ moieties. *Journal of the American Chemical Society*, 122(30):7287–7293, 2000.
- [103] Antonietta De Sio and Christoph Lienau. Vibronic coupling in organic semiconductors for photovoltaics. *Phys. Chem. Chem. Phys.*, 19:18813–18830, 2017.
- [104] Michael Gaus, Xiya Lu, Marcus Elstner, and Qiang Cui. Parameterization of dftb3/3ob for sulfur and phosphorus for chemical and biological applications. *Journal of Chemical Theory and Computation*, 10(4):1518–1537, 2014.
- [105] J.O. Jensen, D. Zeroka, and A. Banerjee. Theoretical studies of the infrared and raman spectra of p4s3 and p4s7. *Journal of Molecular Structure: THEOCHEM*, 505(1):31–43, 2000.
- [106] Chadwick A. Tolman. Phosphorus ligand exchange equilibria on zerovalent nickel. dominant role for steric effects. *Journal of the American Chemical Society*, 92(10):2956–2965, 1970.
- [107] Akira Fujishima. Electrochemical Photolysis of Water at a Semiconductor Electrode. , 238(5358):37–38, July 1972.
- [108] Andrew G. Thomas and Karen L. Syres. Adsorption of organic molecules on rutile tio2 and anatase tio2 single crystal surfaces. *Chem. Soc. Rev.*, 41:4207–4217, 2012.
- [109] Chi Lun Pang, Robert Lindsay, and Geoff Thornton. Chemical reactions on rutile tio2(110). *Chem. Soc. Rev.*, 37:2328–2353, 2008.
- [110] Mingchun Xu, Youkun Gao, Elias Martinez Moreno, Marinus Kunst, Martin Muhler, Yuemin Wang, Hicham Idriss, and Christof Wöll. Photocatalytic activity of bulk tio2 anatase and rutile single crystals using infrared absorption spectroscopy. *Phys. Rev. Lett.*, 106:138302, Mar 2011.

- [111] Jessica Scaranto and Santi Giorgianni. A quantum-mechanical study of co adsorbed on tio₂: A comparison of the lewis acidity of the rutile (110) and the anatase (101) surfaces. *Journal of Molecular Structure: THEOCHEM*, 858(1):72–76, 2008.
- [112] Raina Wanbayor, Peter Deák, Thomas Frauenheim, and Vithaya Ruangpornvisuti. First principles theoretical study of the hole-assisted conversion of co to co₂ on the anatase tio₂(101) surface. *The Journal of Chemical Physics*, 134(10):104701, 2011.
- [113] Martin Setvin, Maria Buchholz, Weiyi Hou, Cui Zhang, Bernhard Stöger, Jan Hulva, Thomas Simschitz, Xiao Shi, Jiri Pavelec, Gareth S. Parkinson, Mingchun Xu, Yuemin Wang, Michael Schmid, Christof Wöll, Annabella Selloni, and Ulrike Diebold. A multitechnique study of co adsorption on the tio₂ anatase (101) surface. *The Journal of Physical Chemistry C*, 119(36):21044–21052, 2015.
- [114] Martin Setvin, Jan Hulva, Gareth S. Parkinson, Michael Schmid, and Ulrike Diebold. Electron transfer between anatase tio₂ and an o₂ molecule directly observed by atomic force microscopy. *Proceedings of the National Academy of Sciences*, 114(13):E2556–E2562, 2017.
- [115] Michael Wagstaffe, Lukas Wenthaus, Adrian Dominguez-Castro, Simon Chung, Guilherme Dalla Lana Semione, Steffen Palutke, Giuseppe Mercurio, Sjarhei Dziarzhyski, Harald Redlin, Nicolai Klemke, Yudong Yang, Thomas Frauenheim, Adriel Dominguez, Franz Kärtner, Angel Rubio, Wilfried Wurth, Andreas Stierle, and Heshmat Noei. Ultrafast real-time dynamics of co oxidation over an oxide photocatalyst. *ACS Catalysis*, 10(22):13650–13658, 2020.
- [116] G. Kresse and J. Hafner. Ab initio molecular dynamics for liquid metals. *Phys. Rev. B*, 47:558–561, Jan 1993.
- [117] G. Kresse and J. Hafner. Ab initio molecular-dynamics simulation of the liquid-metal–amorphous-semiconductor transition in germanium. *Phys. Rev. B*, 49:14251–14269, May 1994.
- [118] G. Kresse and J. Furthmüller. Efficiency of ab-initio total energy calculations for metals and semiconductors using a plane-wave basis set. *Computational Materials Science*, 6(1):15–50, 1996.
- [119] G. Kresse and J. Furthmüller. Efficient iterative schemes for ab initio total-energy calculations using a plane-wave basis set. *Phys. Rev. B*, 54:11169–11186, Oct 1996.
- [120] John P. Perdew, Matthias Ernzerhof, and Kieron Burke. Rationale for mixing exact exchange with density functional approximations. *The Journal of Chemical Physics*, 105(22):9982–9985, 1996.

- [121] P. E. Blöchl. Projector augmented-wave method. *Phys. Rev. B*, 50:17953–17979, Dec 1994.
- [122] G. Kresse and D. Joubert. From ultrasoft pseudopotentials to the projector augmented-wave method. *Phys. Rev. B*, 59:1758–1775, Jan 1999.
- [123] Stefan Grimme, Jens Antony, Stephan Ehrlich, and Helge Krieg. A consistent and accurate ab initio parametrization of density functional dispersion correction (dft-d) for the 94 elements h-pu. *The Journal of Chemical Physics*, 132(15):154104, 2010.
- [124] Stefan Grimme, Stephan Ehrlich, and Lars Goerigk. Effect of the damping function in dispersion corrected density functional theory. *Journal of computational chemistry*, 32:1456–65, 05 2011.
- [125] Meisam Farzalipour Tabriz, Bálint Aradi, Thomas Frauenheim, and Peter Deák. Application of the lany–zunger polaron correction for calculating surface charge trapping. *Journal of Physics: Condensed Matter*, 29(39):394001, aug 2017.
- [126] Stephan Lany, Hannes Raebiger, and Alex Zunger. Magnetic interactions of Cr–Cr and Co–Co impurity pairs in ZnO within a band-gap corrected density functional approach. *Phys. Rev. B*, 77:241201, Jun 2008.
- [127] Stephan Lany. Semiconducting transition metal oxides. *Journal of Physics: Condensed Matter*, 27(28):283203, jun 2015.
- [128] Grygoriy Dolgonos, Bálint Aradi, Ney H. Moreira, and Thomas Frauenheim. An improved self-consistent-charge density-functional tight-binding (scc-dftb) set of parameters for simulation of bulk and molecular systems involving titanium. *Journal of Chemical Theory and Computation*, 6(1):266–278, 2010. PMID: 26614337.
- [129] Amy Linsebigler, Guangquan Lu, and John T. Yates. Co chemisorption on tio₂(110): Oxygen vacancy site influence on co adsorption. *The Journal of Chemical Physics*, 103(21):9438–9443, 1995.
- [130] Dan C. Sorescu and John T. Yates. Adsorption of co on the tio₂(110) surface: a theoretical study. *The Journal of Physical Chemistry B*, 102(23):4556–4565, 1998.
- [131] Zdenek Dohnálek, Joocho Kim, Oleksandr Bondarchuk, J. Mike White, and Bruce D. Kay. Physisorption of n₂, o₂, and co on fully oxidized tio₂(110). *The Journal of Physical Chemistry B*, 110(12):6229–6235, 2006. PMID: 16553438.
- [132] J. Freitag, A. Domínguez, T. A. Niehaus, A. Hülsewig, R. Dillert, T. Frauenheim, and D. W. Bahnemann. Nitrogen(ii) oxide charge transfer complexes on tio₂: A new source for visible-light activity. *The Journal of Physical Chemistry C*, 119(9):4488–4501, 2015.

- [133] A. Vittadini, A. Selloni, F. P. Rotzinger, and M. Grätzel. Structure and energetics of water adsorbed at TiO_2 anatase 101 and 001 surfaces. *Phys. Rev. Lett.*, 81:2954–2957, Oct 1998.
- [134] Regina Luschtinetz, Johannes Frenzel, Theodor Milek, and Gotthard Seifert. Adsorption of phosphonic acid at the TiO_2 anatase (101) and rutile (110) surfaces. *The Journal of Physical Chemistry C*, 113(14):5730–5740, 2009.
- [135] Franco P. Bonafé, Bálint Aradi, Mengxue Guan, Oscar A. Douglas-Gallardo, Chao Lian, Sheng Meng, Thomas Frauenheim, and Cristián G. Sánchez. Plasmon-driven sub-picosecond breathing of metal nanoparticles. *Nanoscale*, 9:12391–12397, 2017.
- [136] Franco P. Bonafé, Federico J. Hernández, Bálint Aradi, Thomas Frauenheim, and Cristián G. Sánchez. Fully atomistic real-time simulations of transient absorption spectroscopy. *The Journal of Physical Chemistry Letters*, 9(15):4355–4359, 2018. PMID: 30024765.
- [137] Daniele Selli, Gianluca Fazio, Gotthard Seifert, and Cristiana Di Valentin. Water multilayers on TiO_2 (101) anatase surface: Assessment of a dftb-based method. *Journal of Chemical Theory and Computation*, 13(8):3862–3873, 2017. PMID: 28679048.
- [138] Ruth Martinez-Casado, Giuseppe Mallia, Nicholas M. Harrison, and Rubén Pérez. First-principles study of the water adsorption on anatase(101) as a function of the coverage. *The Journal of Physical Chemistry C*, 122(36):20736–20744, 2018.
- [139] L. E. Walle, A. Borg, E. M. J. Johansson, S. Plogmaker, H. Rensmo, P. Uvdal, and A. Sandell. Mixed dissociative and molecular water adsorption on anatase TiO_2 (101). *The Journal of Physical Chemistry C*, 115(19):9545–9550, 2011.
- [140] Stephen Rhatigan and Michael Nolan. Activation of water on MnOx -nanocluster-modified rutile (110) and anatase (101) TiO_2 and the role of cation reduction. *Frontiers in Chemistry*, 7, 2019.
- [141] D. D. Beck, J. M. White, and C. T. Ratcliffe. Catalytic reduction of carbon monoxide with hydrogen sulfide. 2. adsorption of water and hydrogen sulfide on anatase and rutile. *The Journal of Physical Chemistry*, 90(14):3123–3131, 1986.
- [142] Sencer Selcuk and Annabella Selloni. Facet-dependent trapping and dynamics of excess electrons at anatase TiO_2 surfaces and aqueous interfaces. *Nature materials*, 15:1107–1112, 2016.
- [143] Annapaola Migani and Lluís Blancafort. What controls photocatalytic water oxidation on rutile TiO_2 (110) under ultra-high-vacuum conditions? *Journal of the American Chemical Society*, 139(34):11845–11856, 2017. PMID: 28768408.

- [144] Gylen Odling and Neil Robertson. Why is anatase a better photocatalyst than rutile? the importance of free hydroxyl radicals. *ChemSusChem*, 8(11):1838–1840, June 2015.
- [145] Kenji Shirai, Gianluca Fazio, Toshiki Sugimoto, Daniele Selli, Lorenzo Ferraro, Kazuya Watanabe, Mitsutaka Haruta, Bunsho Ohtani, Hiroki Kurata, Cristiana Di Valentin, and Yoshiyasu Matsumoto. Water-assisted hole trapping at the highly curved surface of nano-tio₂ photocatalyst. *Journal of the American Chemical Society*, 140(4):1415–1422, 2018. PMID: 29325412.
- [146] Cristiana Di Valentin. A mechanism for the hole-mediated water photooxidation on TiO₂/sub(101) surfaces. *Journal of Physics: Condensed Matter*, 28(7):074002, jan 2016.
- [147] Noèlia Pueyo Bellafont, Francesc Viñes, Wolfgang Hieringer, and Francesc Illas. Predicting core level binding energies shifts: Suitability of the projector augmented wave approach as implemented in vasp. *Journal of Computational Chemistry*, 38:518–522, 2017.
- [148] <https://www.vasp.at/wiki/index.php/icorelevel>. Accessed June 21, 2021.
- [149] <https://aradi.bitbucket.org/nanocut/index.html>. Accessed August 4, 2021.
- [150] Oriol Lamiel-Garcia, Kyoung Chul Ko, Jin Yong Lee, Stefan T. Bromley, and Francesc Illas. When anatase nanoparticles become bulklike: Properties of realistic tio₂ nanoparticles in the 1–6 nm size range from all electron relativistic density functional theory based calculations. *Journal of Chemical Theory and Computation*, 13(4):1785–1793, 2017. PMID: 28230983.
- [151] Rosendo Valero, Ángel Morales-García, and Francesc Illas. Theoretical modeling of electronic excitations of gas-phase and solvated tio₂ nanoclusters and nanoparticles of interest in photocatalysis. *Journal of Chemical Theory and Computation*, 14(8):4391–4404, 2018. PMID: 30011198.
- [152] Timothy B Luttrell, Sandamali Halpegamage, Junguang Tao, Alan Richard Kramer, Eli Sutter, and Matthias Batzill. Why is anatase a better photocatalyst than rutile? - model studies on epitaxial tio₂ films. *Scientific Reports*, 4:4043, 2014.
- [153] Stefan Grimme. Semiempirical gga-type density functional constructed with a long-range dispersion correction. *Journal of Computational Chemistry*, 27(15):1787–1799, 2006.
- [154] https://www.vasp.at/wiki/index.php/xanes_in_diamond. Accessed August 4, 2021.

- [155] Adam Kubas, Max Verkamp, Josh Vura-Weis, Frank Neese, and Dimitrios Maganas. Restricted open-shell configuration interaction singles study on m- and l-edge x-ray absorption spectroscopy of solid chemical systems. *Journal of Chemical Theory and Computation*, 14(8):4320–4334, 2018. PMID: 29949367.
- [156] Torin F. Stetina, Joseph M. Kasper, and Xiaosong Li. Modeling l_{2,3}-edge x-ray absorption spectroscopy with linear response exact two-component relativistic time-dependent density functional theory. *The Journal of Chemical Physics*, 150(23):234103, 2019.
- [157] Robert Huber, Lars Dworak, Jacques E. Moser, Michael Grätzel, and Josef Wachtveitl. Beyond vibrationally mediated electron transfer: Coherent phenomena induced by ultrafast charge separation. *The Journal of Physical Chemistry C*, 120(16):8534–8539, 2016.
- [158] T. Ohsaka, F. Izumi, and Y. Fujiki. Raman spectrum of anatase, tio₂. *J. Raman Spectrosc.*, 7:321–324, 1978.
- [159] M. Giarola, A. Sanson, F. Monti, G. Mariotto, M. Bettinelli, A. Speghini, and G. Salviulo. Vibrational dynamics of anatase tio₂: Polarized raman spectroscopy and ab initio calculations. *Phys. Rev. B*, 81:174305, May 2010.